

Ocena stosowalności metody różnic skończonych  
w dziedzinie częstotliwości do opisu propagacji światła  
w ciekłokrystalicznych światłowodach fotonicznych



**Assessment on the Applicability of Finite Difference  
Methods in Frequency Domain to Model  
Light Propagation in  
Photonic Liquid Crystal Fibers**

**Li-Wei Wei              (ID: 241220)**

**Supervisors      Prof. Małgorzata Kujawińska**  
(Institute of Micromechanics and Photonics)  
**Dr. Katarzyna Rutkowska**  
(Faculty of Physics)

**Master Thesis submitted to the  
Department of Mechatronics,  
Warsaw University of Technology**

**September, 2011**

## Streszczenie

Włókna światłowodowe, o coraz bardziej wyszukanych parametrach i geometriach, wciąż znajdują wiele nowych zastosowań praktycznych w nauce i technice, mając przy tym istotny wpływ do rozwoju współczesnej telekomunikacji. Przykładowo, najnowsze badania prowadzone na właściwościami kryształów fotonicznych pozwoliły na wprowadzenie nowatorskich idei i pomysłów do prac z zakresu optyki światłowodowej. Należy przy tym zwrócić uwagę na podjętą w ostatnich latach tematykę badań nad światłowodami fotonicznymi (*ang. photonic crystal fibers, PCF*), w tym w szczególności nad takimi, dla których możliwe jest uzyskanie dynamicznej zmiany ich właściwości optycznych. Na przykład, przestrajanie parametrów propagacyjnych może być stosunkowo łatwo uzyskane dzięki zastosowaniu ciekłego kryształu, jako materiału wypełniającego otwory światłowodu fotonicznego. Wytwarzane w ten sposób struktury światłowodowe, określane mianem fotonicznych światłowodów ciekłokrystalicznych (*ang. photonic liquid crystal fiber, PLCF*), spotykają się ze znacznym zainteresowaniem ze strony środowiska naukowego. Ich unikatowe właściwości wynikają przy tym nie tylko ze specyfiki zastosowanego elementu bazowego, jakim jest światłowód fotoniczny, ale również z zastosowania ciekłych kryształów, których właściwości optyczne mogą być zmieniane przez czynniki zewnętrzne takie jak temperatura, rozciąganie, ciśnienie, pole elektryczne i/lub magnetyczne. Niestety konieczność uwzględnienia orientacji molekuł ciekłego kryształu oraz jego niejednorodności wewnętrz objętości rozważanego światłowodu fotonicznego wprowadza dodatkowe wyzwanie w przypadku opisu teoretycznego jak i badań eksperymentalnych nad ciekłokrystalicznymi światłowodami fotonicznymi.

Najbardziej znanym i najbliższym modelem służącym do analizy i teoretycznej charakteryzacji światłowodów jest opis analityczny uzyskany dla przypadku pola skalarnego i przy założeniu polaryzacji liniowej. Model ten pozwala na dokładny opis propagacji modów światłowodowych dla większości typowych światłowodów telekomunikacyjnych, niestety zawodzi on w przypadku bardziej skomplikowanych i zaawansowanych struktur. W takich przypadkach konieczne okazuje się zastosowanie zapisu wektorowego pola elektromagnetycznego fali świetlnej. Dodatkowo, w ogólnym przypadku jest bardzo trudne lub wręcz niemożliwe uzyskanie rozwiązań analitycznych dla propagacji światła w kryształach fotonicznych. Na szczęście, dzięki stałemu rozwojowi w dziedzinie informatyki i fizyki komputerowej, zaproponowanych zostało wiele schematów numerycznych, które mogłyby zostać zastosowane do charakteryzacji światłowodów mikrostrukturalnych.

Niniejsza praca dotyczy w szczególności opracowania skutecznych metod numerycznych służących do opisu propagacji światła w ciekłokrystalicznych światłowodach fotonicznych przy wykorzystaniu dostępnych zasobów sprzętowych. W szczególności, sformułowane zostały opisy teoretyczne zarówno dla pola skalarnego jak i wektorowego, a następnie odpowiednie schematy opisu propagacji modów światłowodowych zostały zaimplementowane numerycznie przy zastosowaniu metod różnic skończonych. W porównaniu do wartości uzyskanych analitycznie dla światłowodu skokowego o dużym kontraście współczynników załamania, błąd względny wprowadzany przez zastosowanie pola skalarnego jest niemalże **100** razy większy niż ten uzyskany dla opisu wektorowego. Zastosowanie tego ostatniego pozwala na uzyskanie błędu względnego  $\sim 3 \cdot 10^{-6}$  dla efektywnego współczynnika załamania modu podstawowego w światłowodzie skokowym o dużym kontraście współczynników załamania oraz  $\sim 4 \cdot 10^{-4}$  w światłowodzie fotonicznym typu Holey-Fiber (w przypadku propagacji na zasadzie zmodyfikowanego całkowitego wewnętrznego odbicia). W przypadku symulacji numerycznych przeprowadzonych dla ciekłokrystalicznych światłowodów fotonicznych błąd ten został oszacowany na poziomie poniżej  $10^{-3}$  i co więcej przeprowadzone symulacje potwierdziły istnienie przerw fotonicznych w widmie transmisyjnym (co zostało zaobserwowane również eksperymentalnie).

Mając na uwadze uzyskane wyniki, przewiduje się dalszy rozwój tematyki poruszonej w niniejszej pracy, w tym badania eksperymentalne jak i przeprowadzenie dodatkowych symulacji numerycznych, w celu potwierdzenia właściwego działania i optymalizacji napisanych skryptów oraz dokładności przeprowadzanych obliczeń. W szczególności zaproponowany i opracowany pełno-wektorowy schemat do wyznaczania modów światłowodowych przy zastosowaniu metody różnic skończonych w dziedzinie częstotliwości może być z łatwością wykorzystany przy rozważaniu anizotropii ciekłego kryształu przy dowolnym obrocie molekuł w płaszczyźnie poprzecznej w stosunku do kierunku propagacji światła (osi światłowodu).

---

## Summary

Optical fibers have found vast applications in science and technology, and contributed largely to the infrastructure of telecommunications. Studies on properties of photonic crystals have infused new ideas and visions into the field of fiber optics. Recently, photonic crystal fibers (PCFs) with highly tunable optical properties achieved by their infiltration with liquid crystals (LCs) have gained significant amount of scientific attention.

These particular fiber structures are often referred to as photonic liquid crystal fibers (PLCFs). Their unique characteristics not only result from specific properties of the structure of host PCFs, but also from the highly tunable optical properties of LCs. Such tunability can be achieved by applying external factors like temperature, strain, pressure, electric or/and magnetic fields. However, owing to their quasi-crystalline, non-uniform nature, LCs introduce further challenges in theoretical, numerical and experimental characterization of PLCFs.

Conventionally, the most well-known and the simplest model for optical fiber characterization is the analytical scalar-field formulation with linearly polarized field approximation. It provides fairly straightforward and accurate characterization of practical telecommunication fibers, but fails for more complicated fiber geometries (e.g. with high contrast on refractive index). In such case the vector-field formulation is required. Moreover, when photonic crystal structures are incorporated, analytical solutions are difficult to obtain, if not impossible. Thanks to the advance of computer science and computational physics, various types of numerical schemes have been proposed to characterize optical fibers with micro-structures.

In this thesis, we focus on numerical methods for the characterization of PLCFs with accessible computational effort. More specifically, both the scalar-field scheme and the vector-field scheme are formulated theoretically and implemented numerically with finite difference methods (FDFD/FDM). Compared to analytical values, the relative error introduced in the scalar-field formulation is almost **100** times higher than the vector-field formulation for a high index-contrast step-index fiber (HC-SIF). When vector-field FDFD is applied, relative error of **3ppm** is observed for effective refractive index of the fundamental mode in HC-SIF and **413ppm** in a holey fiber (HoF) with index-guiding geometry. The **<0.1%** relative errors qualify for simulations on PLCFs. However, spurious results appear to be a concern when photonic bandgap (PBG) guiding fiber geometries are considered, as the eigenvalue range of the simulation is very limited under some conditions. Simulations show the wavelength selectivity in transmission spectrum, which is correspondingly observed in experiments. Future examinations on both the experiment and the numerical schemes are required to justify the simulations and to analyze the discrepancy. In particular, a vector-field FDFD scheme developed and implemented here can easily take into consideration the anisotropy of LC with arbitrary rotation in the transverse plane with respect to the propagation axis of the fiber.

---

## Acknowledgement

This thesis would not have been possible without the support from many parties. It is truly a honored pleasure of mine to express my gratitude to all the guidance and support that have accompanied me through the master program.

First, I would like to thank Dr. Katarzyna Rutkowska, as my supervisor, for being so kind in leading me through such an interesting field of optics. Second, I would still like to thank Dr. Katarzyna Rutkowska for being a patient reader and a hearty colleague who has made various corrections to my carelessness and provided delightful discussions on my doubts regarding the subject. If fair readability of the thesis is anyhow achieved, it shall be accredited to her careful revision. Thank you.

I would like to show my gratitude to Prof. Małgorzata Kujawińska and the colleagues at the Institute of Micromechanics and Photonics of Warsaw University of Technology for discussions and orientations of my work. My special thanks go to Marzena Tefelska and Miłosz Chychłowski, who supported me with experimental setups and measurements. It was truly an enjoyable experience working with you in the labs sharing odds and ends on the marvelous phenomena of light. I also want to thank the Faculty of Physics of Warsaw University of Technology for supporting me with experimental work and numerical computations.

I would like to thank my girlfriend Yu-Chen Cheng for her patience and understanding during my studies abroad, which have always shortened the distance between Europe and home together with the support from my family.

It is an honor for me to carry out my master study in the framework of the Erasmus Mundus program Optics in Science and Technology with financial support from the associated scholarship.

Last but not least, I would like to express my gratitude to Prof. Yin-Chieh Lai, who taught me valuable lessons in National Chiao Tung University in Taiwan and opened up my gate to overseas studies. In fact, the numerical methods developed in this thesis were started with a term project report regarding numerical methods in optical physics.

Li-Wei Wei

September 2<sup>nd</sup> 2011 Warsaw, Poland

---

## Table of Contents

Streszczenie.....	I
Summary.....	II
Acknowledgement.....	III
Table of Contents.....	IV
List of Figures .....	VII
List of Tables.....	X
1      Introduction .....	1
1.1    Photonic Liquid Crystal Fiber (PLCF).....	1
1.2    Motivation .....	2
1.3    Objectives .....	2
1.4    Organization of the Thesis.....	3
2      Optical Fibers and Liquid Crystals .....	4
2.1    Optical Fibers in Telecommunication and Beyond .....	4
2.2    Microstructures in Optical Fibers .....	5
2.3    Guiding Mechanisms in Optical Fibers .....	7
2.3.1    Index-Guiding .....	9
2.3.2    Photonic Bandgap Guiding.....	9
2.4    Photonic Liquid Crystal Fibers .....	10
3      Numerical Modeling Schemes .....	12
3.1    Theory for Optical Fiber Modeling .....	12
3.1.1    Maxwell Equations .....	12
3.1.2    Scalar-Field Formulation .....	13
3.1.3    Vector-Field Formulation .....	16
3.2    Overview of Characterization Methods for Microstructured Optical Fibers.....	18
3.2.1    Effective Index Approach .....	19
3.2.2    Basis-Function Expansion Approach .....	20
3.2.3    Numerical Approach .....	20

---

3.2.4	Choices for PLCF Characterization.....	21
4	Finite Difference Methods in Frequency Domain (FDM/ FDFD) .....	24
4.1	Scalar-Field FDFD .....	25
4.2	Material Anisotropy in FDFD .....	27
4.3	Vector-Field FDFD .....	28
4.4	Some Techniques Regarding Improvement of FDFD .....	37
4.5	Spurious Modes and Their Elimination .....	39
4.5.1	Post-Computation Correlation .....	39
4.5.2	Pre-Computation Edge-Cutting .....	39
4.5.3	In-Computation Eigen Solver Specifications .....	40
4.5.4	Divergence Maxwell Equations .....	41
4.6	Implementation of the Scalar-Field FDFD and the Vector-Field FDFD .....	41
4.7	Verification and Benchmarking of Proposed Schemes .....	41
4.7.1	Methods for Verification .....	41
4.7.2	Single-Mode Fiber (SMF).....	44
4.7.3	Multi-Mode Fiber (MMF).....	50
4.7.4	High Index-Contrast Step-Index Fiber (HC-SIF) .....	58
4.7.5	Holey Fiber (HoF) .....	60
4.7.6	Summary on Benchmarking of FDFD .....	63
4.8	Summary on Implemented FDFDs.....	63
5	Photonic Liquid Crystal Fiber of Interest.....	65
5.1	Photonic Liquid Crystal Fiber Geometry.....	65
5.2	Liquid Crystal for Infiltration.....	65
5.3	Molecular Arrangements of Liquid Crystals .....	66
5.4	PLCF Sample Preparation .....	67
5.5	Experimental Setup .....	69
5.6	Numerical Setup .....	70
5.6.1	Refractive Index of Silica .....	70
5.6.2	Refractive Index of 6CHBT .....	72
5.6.3	Numerical Auto-Verification and Comparison with Experimental Results .....	73

---

---

5.7	Experimental and Numerical Results for the Host PCF .....	74
5.7.1	Field Intensity Distribution.....	74
5.7.2	Transmission Spectrum .....	79
5.8	Experimental and Numerical Results for the PLCF Sample .....	80
5.8.1	Field Intensity Distribution.....	80
5.8.2	Transmission Spectrum .....	85
5.9	Discussions and Numerical Study of PLCF .....	88
5.9.1	Polarization and Birefringence .....	88
5.9.2	Rotation of Liquid Crystals in the Transverse Plane of the PLCF .....	88
6	Conclusions and Outlook .....	89
Appendix A	.....	92
Appendix B	.....	102
Appendix C	.....	103
Appendix D	.....	104
Appendix E	.....	105
Bibliography	.....	110

---

## List of Figures

Figure 2-1: Optical (OM) and scanning electron (SEM) micrographs of PCF structures .....	6
Figure 2-2: Some types of PCF geometries .....	7
Figure 2-3: Propagation diagrams for A) Single-Mode Fiber and B) Photonic Crystal Fiber .....	8
Figure 2-4: A PCF filled with short-pitch chiral nematic liquid crystals (N*LC) shows PBG location sensitivity of 1nm/°C (visible) and 3nm/°C (infrared) .....	11
Figure 3-1: Schematic of a triangular-lattice PCF.....	19
Figure 3-2: Estimation on 2D-FDFD computational effort for an exemplary PLCF geometry with two coupling field components.....	23
Figure 4-1: Finite-difference formulae for 2 <sup>nd</sup> -order differentiation .....	25
Figure 4-2: Discretized scalar-field eigenvalue problem with corresponding global matrix .....	27
Figure 4-3: The staggered Yee mesh configuration for the vector-field FDFD implemented .....	30
Figure 4-4: Schematic of Dirichlet and Neumann boundary conditions.....	34
Figure 4-5: Schematic of staircase approximation for curved interface and index-averaging.....	38
Figure 4-6: Permittivity profile of a three-ring PCF with edge-cutting .....	40
Figure 4-7: Dispersion relation curves of the SMF for $l = 0$ and $l = 1$ .....	46
Figure 4-8: Convergence curves of the SMF with respect to the size of calculation window calculated with scalar-field FDFD.....	47
Figure 4-9: Convergence curves of the SMF with respect to the number of grids .....	48
Figure 4-10: Convergence curves of the SMF with respect to the number of grids with index-averaging factor 10.....	49
Figure 4-11: Eigenfields (eigenvectors in matrix formulation) of the SMF with the largest 16 eigenvalues calculated with scalar-field FDFD .....	49
Figure 4-12: Fundamental eigenfields of the SMF calculated with vector-field FDFD .....	50
Figure 4-13: Dispersion relation curves of the MMF from $l = 0$ to $l = 6$ .....	51
Figure 4-14: Convergence curves of the MMF with respect to the size of calculation window calculated with scalar-field FDFD .....	52
Figure 4-15: More detailed convergence curves with respect to the size of calculation window for the first five modes of the MMF calculated with scalar-field FDFD .....	53
Figure 4-16: Convergence curves of the MMF calculated with scalar-field FDFD and without index-averaging .....	54
Figure 4-17: Convergence curves of the MMF calculated with scalar-field FDFD and index-averaging factor 10 .....	54
Figure 4-18: Convergence curves of the MMF calculated with vector-field FDFD and	

---

index-averaging factor 10.....	55
Figure 4-19: Degeneracy of some $LP_{lm}$ modes in a MMF.....	56
Figure 4-20: Eigenfields with the largest 20 eigenvalues of the MMF calculated with scalar-field FDFD .....	57
Figure 4-21: Eigenfields (Ex) with the largest 48 eigenvalues of the MMF calculated with vector-field FDFD.....	57
Figure 4-22: Dispersion relation curves of the HC-SIF from $l = 0$ to $l = 10$ .....	59
Figure 4-23: Convergence curves of the fundamental $n_{eff}$ of the HC-SIF with scalar-field FDFD (top) and vector-field FDFD (bottom) .....	60
Figure 4-24: Convergence curves of the fundamental $n_{eff}$ of the HoF with scalar-field FDFD (top) and vector-field FDFD (bottom) .....	61
Figure 4-25: The 1 <sup>st</sup> and 2 <sup>nd</sup> sets of eigenfields in E-formulation (Ex-Ey-Hz) of the HoF .....	62
Figure 4-26: The 1 <sup>st</sup> and 2 <sup>nd</sup> sets of eigenfields in H-formulation (Hx-Hy-Ez) of the HoF .....	62
Figure 5-1: PLCF of interest, showing the three-ring host PCF 070124, the nematic LC, 6CHBT, and the optical microscope image .....	65
Figure 5-2: Uniaxial nematic liquid crystal (N-LC) model.....	66
Figure 5-3: Molecular arrangements of LC inside the holes of PCF .....	66
Figure 5-4: Variants of molecular arrangements of LC inside the holes of PCF .....	67
Figure 5-5: PCF immersed in LC.....	68
Figure 5-6: Selected frames from the LC infiltration video clip .....	69
Figure 5-7: Experimental setup .....	70
Figure 5-8: Temperature dependent dispersion curves of silica .....	71
Figure 5-9: Temperature dependent dispersion curves of silica (zoom in).....	71
Figure 5-10: The mixture of nCHBT (nCPS) .....	72
Figure 5-11: Coefficients for nCHBT (nCPS) mixture with single band model .....	72
Figure 5-12: Ordinary and extraordinary dispersion curves of 6CHBT at T=28°C.....	73
Figure 5-13: Experimental results on far-field intensity distribution of an empty PCF 070124 .....	74
Figure 5-14: Convergence curves of the fundamental $n_{eff}$ of PCF 701024 with respect to the number of grids calculated with scalar-field FDFD (top) and vector-field FDFD (bottom).....	76
Figure 5-15: Eigenfields (Ex) of the core-guiding modes of PCF 070124 .....	76
Figure 5-16: Exemplary set of eigenfields of PCF 070124 at $\lambda = 555\text{nm}$ calculated with vector-field FDFD (top: Ex, bottom: Ey) .....	77
Figure 5-17: The 1 <sup>st</sup> and 2 <sup>nd</sup> sets of eigenfields in E-formulation (Ex-Ey-Hz) of PCF 070124 .....	78
Figure 5-18: The 1 <sup>st</sup> and 2 <sup>nd</sup> sets of eigenfields in H-formulation (Hx-Hy-Ez) of PCF 070124 .....	78
Figure 5-19: Experimental results on transmission spectrum of an empty PCF 070124 .....	79
Figure 5-20: Numerical results on fundamental $n_{eff}$ vs. wavelength of PCF 070124 .....	80
Figure 5-21: Experimental result on far-field intensity distribution of the PLCF sample.....	80
Figure 5-22: Experimental results on near-field intensity distribution of the PLCF sample at	

---

---

different light levels.....	81
Figure 5-23: Types of modes (Ex) of the PLCF sample calculated with vector-field FDFD.....	82
Figure 5-24: Exemplary set of eigenfields of the PLCF sample at $\lambda = 686\text{nm}$ with vector-field FDFD (top: Ex, bottom: Ey) .....	83
Figure 5-25: The 1 <sup>st</sup> and 2 <sup>nd</sup> sets of eigenfields in E-formulation (Ex-Ey-Hz) of the PLCF sample.....	84
Figure 5-26: The 1 <sup>st</sup> and 2 <sup>nd</sup> sets of eigenfields in H-formulation (Hx-Hy-Ez) of the PLCF sample ....	84
Figure 5-27: Experimental results on transmission spectrum of the PLCF sample.....	86
Figure 5-28: Numerical results on fundamental $n_{eff}$ vs. wavelength of the PLCF sample.....	86
Figure 5-29: Convergence curves of the PLCF sample with respect to the number of grids calculated with vector-field FDFD .....	87
Figure 5-30: Convergence curve of the PLCF sample with respect to the square of grid size calculated with vector-field FDFD .....	87

---

## List of Tables

Table 4-1: Material anisotropy and corresponding permittivity tensor form .....	31
Table 4-2: Complexity of FDFD eigenvalue problem and size of FDFD global matrix with respect to permittivity tensor form.....	32
Table 4-3: Sparsity of FDFD global matrix with respect to permittivity tensor form .....	32
Table 4-4: Exemplary 1 <sup>st</sup> -order finite-difference matrices for different boundary conditions .....	35
Table 4-5: Excerpted parameters of Corning <sup>®</sup> SMF-28 <sup>™</sup> Optical Fiber.....	44
Table 4-6: Sellmeier coefficients for fused silica .....	44
Table 4-7: The SMF for benchmarking .....	45
Table 4-8: Common FDFD simulation parameters for the SMF .....	46
Table 4-9: The MMF for benchmarking.....	50
Table 4-10: $n_{eff}$ of $LP_{lm}$ modes of the MMF .....	51
Table 4-11: Scalar-field FDFD simulation parameters for the MMF .....	52
Table 4-12: Scalar-field FDFD results on $n_{eff}$ and errors of the $LP_{lm}$ modes of the MMF .....	55
Table 4-13: Vector-field FDFD results on $n_{eff}$ and errors of the $LP_{lm}$ modes of the MMF .....	56
Table 4-14: The HC-SIF for benchmarking.....	58
Table 4-15: $n_{eff}$ of the $LP_{lm}$ modes of the HC-SIF .....	59
Table 4-16 Common FDFD simulation parameters for the HC-SIF.....	60
Table 4-17: The HoF for benchmarking and the FDFD simulation parameters.....	61
Table 4-18: Reference values on fundamental $n_{eff}$ of the HoF and our simulation results.....	61
Table 4-19: Benchmarking results of the scalar-field FDFD and the vector-field FDFD .....	63
Table 5-1: Temperature-dependent Sellmeier coefficients for silica .....	71
Table 5-2: Vector-field FDFD simulation parameters for PCF 070124 and the PLCF sample .....	75
Table 5-3: Vector-field FDFD results on $n_{eff}$ of the first six modes in PCF 070124 .....	75

## 1 Introduction

### 1.1 Photonic Liquid Crystal Fiber (PLCF)

Photonic crystals (PCs) are a new type of optical materials that has unusual optical properties and corresponding unprecedented applications. As an analogy to the atomic bandgap concept for electronic materials, the theory of photonic bandgap (PBG) has been developed for the optical materials.

Within a photonic bandgap, there is no available light modes (photons) for some frequency range and therefore the propagation of light is prohibited. A defect state within the photonic bandgap traps photons with certain combinations of optical frequency and wave vector. Confinement of light with such structure can therefore lead to the formation of optical cavities and waveguides, which correspond to three-dimensional (3D) and two-dimensional (2D) photonic crystal structures, respectively.

Photonic crystal fibers (PCFs) are the special class of 2D photonic crystal structures with cylindrical symmetry, extended homogeneously over the third dimension -- the axis of both propagation and symmetry. In addition to PBG guiding, PCFs can also guide light with the index-guiding mechanism, as conventional optical fibers do. General cross section (*fiber structure or geometry*) of PCF can be divided into two regions, the circular core and the annular cladding. The cladding generally consists of periodic air holes, forming photonic lattices, while the core region can either consist of solid materials as in conventional fibers, or remain hollow in some designs with PBG guiding. It is important to note that PCF geometries are highly flexible and give vast freedom in engineering and tailoring towards desired optical properties.

Recently, PCFs with highly tunable optical properties that can be relatively easily achieved by their infiltration with liquid crystals (LCs) have gained significant amount of the scientific attention. They are often referred to as photonic liquid crystal fibers (PLCFs) ([Wolinski et al., 2006](#)), liquid crystal-photonic crystal fibers (LC-PCFs) ([Du et al., 2004](#)), or liquid crystal-photonic bandgap fibers ([Larsen et al., 2003](#)). Their unique characteristics depend not only on the applied geometry of the PCF host, but also on the highly tunable optical properties of LC. The latter can be achieved by applying external factors like temperature, strain, pressure, electric or/and magnetic fields.

## 1.2 Motivation

Simple characterization of practical optical fibers (i.e., step-index geometries with small index-contrast) can be achieved by linearly polarized (LP) approximation under scalar-field formulation ([Gloge, 1971](#)). It enables analytical analysis of the fiber modes in which the vector fields are decoupled into individual scalar fields. Therefore, the resultant field distributions are called linearly polarized modes,  $LP_{lm}$ , where the subscripts  $l$  and  $m$  denote the order of the mode.

Although it is simple and accurate for typical telecommunication fibers, the use of the LP approximation under scalar-field formulation is however very limited. For more general fiber geometries, it is often not possible to find analytical solutions. Furthermore, even with a simple step-index geometry, when the index-contrast is large, scalar-field LP formulation fails to give accurate results because the coupling between vector field components are no longer negligible.

In order to characterize general fiber geometries, vector field formulation is required. Solving analytically the Maxwell equations with vector-field formulation is complicated, if not impossible, especially when complex refractive index profiles are also introduced. An alternative is to solve the Maxwell equations numerically. Numerical analysis nowadays has become more and more realistic thanks to powerful computers, whose limits are still being pushed further and further. They are an useful tool in modern science, and play an important role in modeling physical problems. As the Chinese saying goes, “to do the job well, one must first sharpen his tools”, the study of PLCFs can also be facilitated by introducing and refining numerical methods.

To sum up, the interesting characteristics of PLCFs are worth paying attention. However, it is difficult, if not impossible, to study PLCFs analytically. Not only the vector nature of light has to be taken into account for accurate analysis, but also the material anisotropy and the finite order of LC. Moreover, when LC molecules are infiltrated into a PCF host, resulting in a PLCF, the boundary interactions are also crucial for accurate analysis. It is therefore essential to progress the study of PLCFs with the advance of computer science.

---

## 1.3 Objectives

The main objective of the thesis is to construct computationally accessible and efficient numerical schemes that are capable of characterizing general optical fiber geometries, with an emphasize on photonic liquid crystal fibers.

In this work, finite-difference methods in frequency domain (FDM/FDFD) are proposed to

study the propagation of light in PLCFs after reviewing related literature, and FDFD is implemented and carried out all through the thesis. The implemented schemes are examined with various factors, including comparison with experimental results.

#### **1.4 Organization of the Thesis**

The presented thesis consists of six chapters. In **Chapter 1** an introduction of the thesis is given. In **Chapter 2** the historical development from optical fibers to PLCFs is shortly accounted. **Chapter 3** describes possible numerical modeling schemes for optical fiber characterization, among which FDFD methods are chosen in this work. Both scalar-field and vector-field FDFD schemes are implemented to characterize the PLCFs of interest, and are discussed in details in **Chapter 4**. **Chapter 5** shows both numerical and experimental results obtained for the PLCF of interest. In **Chapter 6**, conclusions are drawn with discussions, and outlook for future work is presented.

## 2 Optical Fibers and Liquid Crystals

In this chapter we introduce briefly the development of PLCFs, which originated from the concept of microstructured optical fibers (MOFs) and utilization of the specific properties of liquid crystals.

### 2.1 Optical Fibers in Telecommunication and Beyond

Electromagnetic waves provide the most reliable, economical and fastest means of information transfer in today's communication technologies, which expand from radio waves, microwaves to infrared and the visible spectra. Historically, Alexander Graham Bell was known to be the pioneer in using light waves for communication. In **1880** he invented the *photophone* which he claimed as "the greatest invention I have ever made, greater than the telephone." The schematic of the *photophone* can be found in Chapter 4 of the book *Fiber Optic Essentials* by [Thyagarajan and Ghatak, 2007](#). Nowadays, standard optical wavelengths for telecommunication are specified at **1310nm** and **1550nm**, which coincide with the two low-loss bands of silica. Indeed, the dramatic reduction in transmission loss made optical fiber communication a practical technology, as accredited by the [Nobel Prize in Physics, 2009](#) to the laureate Charles K. Kao, "for groundbreaking achievements concerning the transmission of light in fibers for optical communication." Along with the development of semiconductor lasers and detectors, optical fibers are an essential building block of modern communication infrastructure, and are still burgeoning along with the growth of Internet.

Other than in telecommunications, where they act as signal carriers, optical fibers also find their applications in the general fields of optics and photonics. By nature, optical fibers are suitable for:

- a) Long-haul signal transfer

Progress in purifying silica has led to less than **0.2dB/km** loss in modern telecom fibers. If we express this figure in real life, it means that after **10** kilometers of propagation, the optical power drops only by a factor of two. Such performance is unmatchable for other existing technologies. Together with fiber amplifiers which enable all-optical signal transfer over long distances, optical fibers have become the most significant backbone in telecommunications.

- b) Miniaturized optical systems

To compensate the diffraction and to define the propagation direction of light, i.e., to

guide light in bulk optics, it usually requires various optical components such as lenses and mirrors. For example, in **1964**, Goubau and Christian at Bell Labs proposed a beam waveguide that consists of a series of lenses ([Thyagarajan and Ghatak, 2007](#)). The focusing of lenses compensates the diffraction of light and therefore limits the spatial extension of the beam.

A modern optical fiber has diameter around **125** microns, and limits the spatial extent of light to few tens of microns. Together with the ultra-low loss, an optical fiber guides light efficiently in terms of the ratio between the longitudinal propagation distance and the transverse spatial extent.

With an optical fiber, one can easily bring light along almost arbitrary path to desired locations. Therefore, optical fibers are often advantageous in miniaturizing the size and the complexity of an optical setup, and moreover provide the setup with additional flexibility. Fiber optic endoscope (imaging fiber) and beam delivery systems illustrate such characteristic. In addition, fiber optic miniaturization also finds useful applications in many interferometric setups.

c) Nonlinear optics

The magnitude of nonlinear processes depends largely on the intensity of the light field. Optical fibers with typical core diameters, ranging from a few microns to a few tens of microns, possess high field intensity for efficient nonlinear processes. The book *Nonlinear Fiber Optics* by [Agrawal, 2007](#) best justifies the active role of optical fibers in the field of nonlinear optics.

d) Various sensing applications

Optical fibers are extremely sensitive to external factors such as stress, strain, and temperature. For telecom uses, optical fibers are protected with additional polymer and fabric layers. However, when raw fibers are used, many sensing applications arise. One application worth mentioning is the high-temperature (up to approx. 2000K) sensor obtained with the use of sapphire ( $\text{Al}_2\text{O}_3$ ) fibers ([Dils, 1983; Shen et al., 1999](#)).

## 2.2 Microstructures in Optical Fibers

Generally speaking, when optical fibers are addressed, step-index fibers (SIFs), owing to their vast uses in telecommunications, come naturally into mind. However, possible manipulation with the fiber geometry gives additional degree of freedom in tailoring the characteristics of the optical fibers. Microstructured optical fibers (MOFs) are the derived application of this concept.

It is useful here to make some notes on terminology. Photonic crystal fiber (PCF) is

another common name to refer to this type of optical fibers because MOFs often contain periodic PC structures in the cladding region. In literature, sometimes the term PCF is reserved for PCFs with PBG guiding. In the context of the thesis, we refer to PCFs for their PC structure. Guiding mechanisms will be specified separately, and that leads to index- and PBG-guiding PCFs.

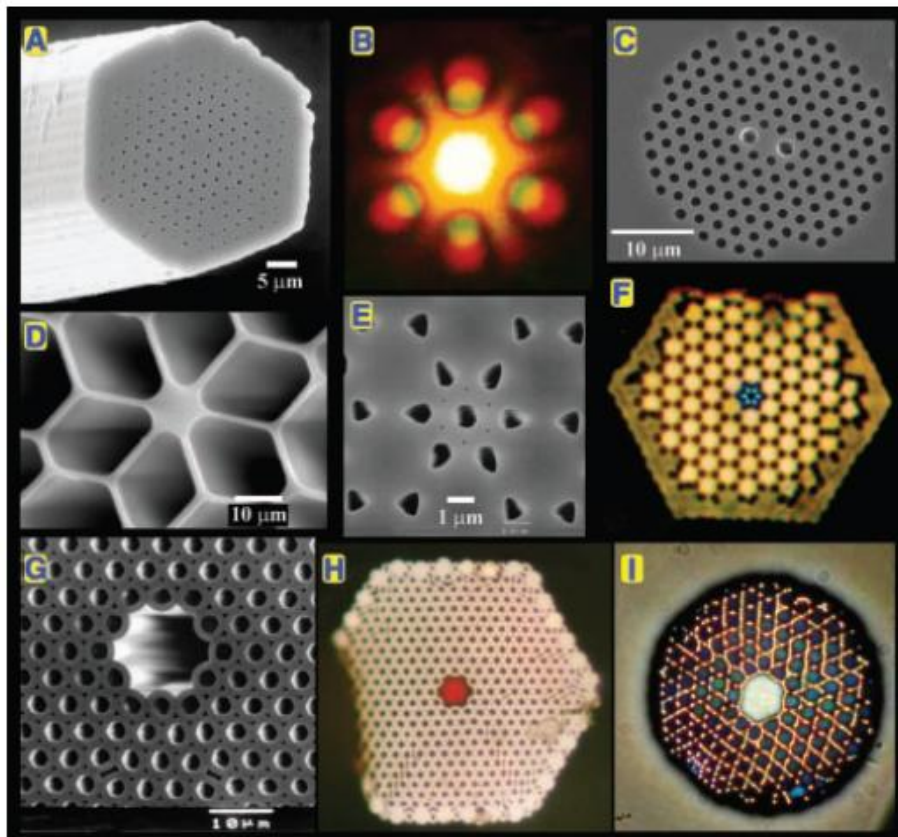


**Figure 2-1: Optical (OM) and scanning electron (SEM) micrographs of PCF structures**

- A) Endlessly single-mode solid-core PCF; B) Far-field optical pattern produced by [A] when excited by red and green light; C) Birefringent PCF; D) Small-core (800 nm) PCF with ultrahigh nonlinearity and zero chromatic dispersion at 560 nm; E) First photonic band gap fiber; F) Near-field OM of the six-leaved blue mode that appears when [E] is excited by white light; G) Hollow-core photonic band gap fiber; H) Near-field OM of a red mode; I) Hollow-core PCF with a Kagome cladding lattice, guiding white light. ([Russell, 2003](#))

The introduction of microstructures broadens largely the use of optical fibers in nonlinear optics. One well-known example is the generation of supercontinuum ([Dudley et al., 2006](#)). In addition, recent studies on PCF structures have shown that by confining light in a sub-micron core, it is possible to extend the zero-dispersion wavelength to the visible

range (Russell, 2003; Knight et al., 2000). A PCF with close-to-zero chromatic dispersion over hundreds of nm was also reported (Reeves et al., 2002). **Figure 2-1** shows some examples of PCF structures, excerpted from the review paper by Russell, 2003.

One interesting degree of freedom that comes along with PCF geometries is the air holes in the cladding region. Filling the air holes with gaseous and liquid media leads to even more extraordinary properties of PCFs. The concept then was extended to the infiltration with LCs (Larsen et al., 2003). This thesis sets its focus on the last, PCFs infiltrated with LCs, which will henceforth be addressed as photonic liquid crystal fibers (PLCFs) (Wolinski et al., 2006).

Partly borrowed from Knight, 2003, **Figure 2-2** shows some PCF designs among which we target this thesis on the characterization of the structure shown in **Figure 2-2c** for which the bandgap-guiding mechanism is possible (depending on the refractive index of LC used for infiltration).

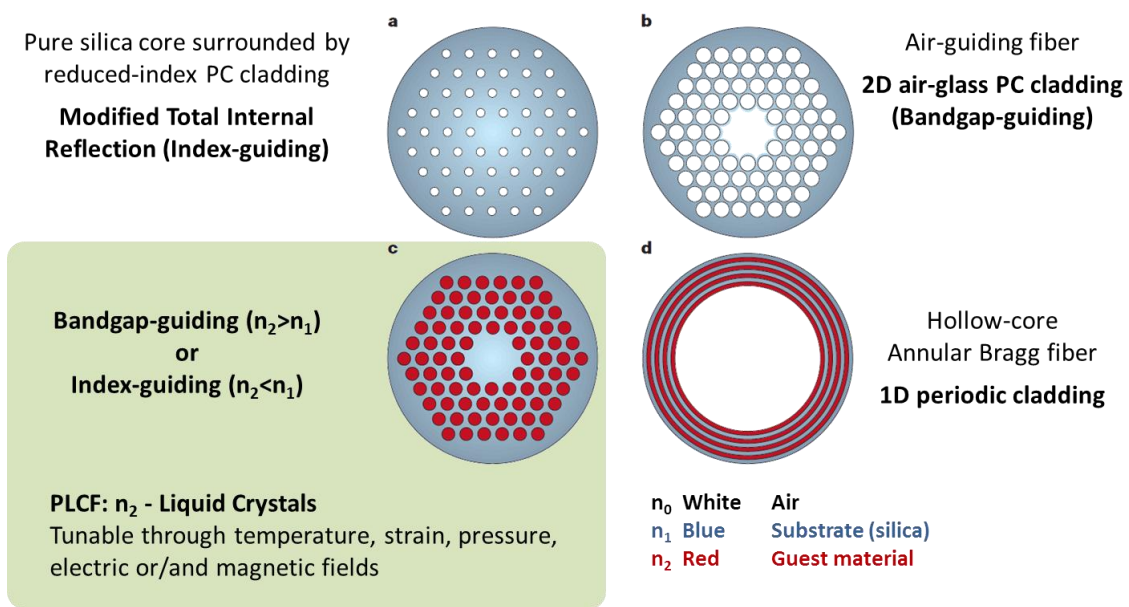


**Figure 2-2: Some types of PCF geometries**

### 2.3 Guiding Mechanisms in Optical Fibers

The guiding properties of an optical fiber depend on the cross-sectional refractive index profile. In the case of conventional fibers, which consist of a higher-index core and a lower-index cladding, the guidance of light is well explained by its confinement in the higher refractive index medium of the core.

On the other hand, studies on photonic crystals have ported new visions into the field of optical fibers. [Yablonovitch, 1993](#) described in his paper that by periodically arranging the structure in the scale of the wavelength, one can obtain photonic bandgaps that are analogous to atomic bandgaps in atomic crystals where the periodicity is in the order of the wavelength of electron waves. A defect state within such a photonic crystal enables the confinement of waves with certain frequency and wave vector, as they are forbidden to propagate in the surrounding photonic crystal ([John, 1987](#)).

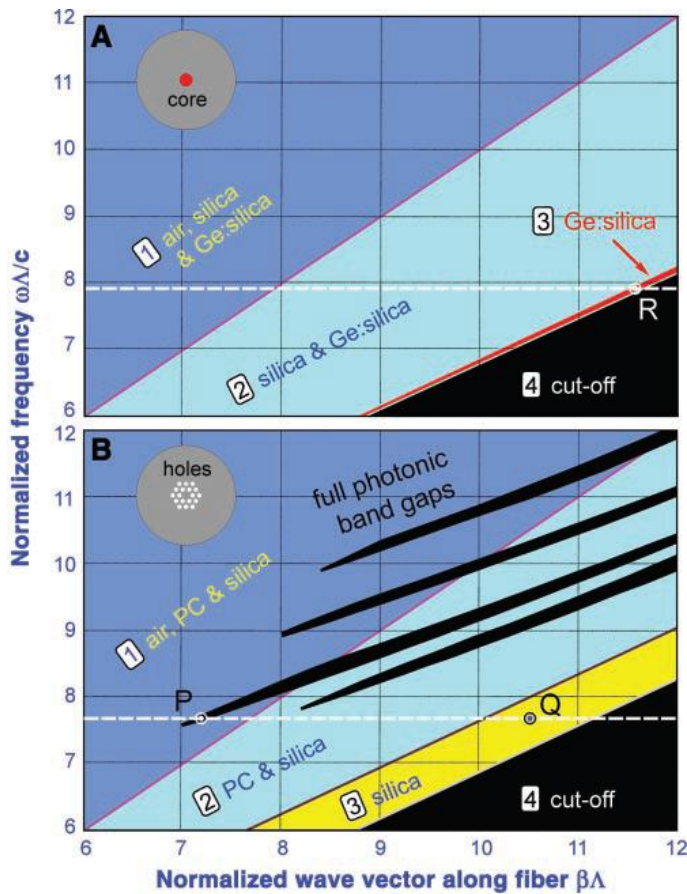


**Figure 2-3: Propagation diagrams for A) Single-Mode Fiber and B) Photonic Crystal Fiber**

Each shade indicates the number of regions where the light is free to propagate. Above: Light propagates freely in all three regions, the Ge:silica core, the silica cladding, and the surrounding air, in the blue-shaded area. In the cyan-shaded area, light is no longer free to propagate in air as the effective refractive index ( $n_{eff}$ ) of propagation exceeds that of the air.

As we approach to the bottom right,  $n_{eff}$  further increases such that light also becomes evanescent in the silica cladding (red-shade area), and eventually no region supports light propagation when  $n_{eff}$  reaches cut-off (black-shade area). Bottom: for a PCF, other than the continuous bands of areas, there also exist discrete 'fingers' which represent the location of photonic bandgaps of the PC cladding. ([Russell, 2003](#))

In the following two sections, we use the ‘propagation diagrams’ (**Figure 2-3**, after [Russell, 2003](#)) to illustrate the possible guiding mechanism(s), which are index- and/or PBG-guiding, in two fiber geometries, a conventional single-mode fiber with germanium-doped silica core (Ge:silica) and a PCF. The axes of the propagation diagram are the dimensionless quantities  $\beta\Lambda$  and  $\omega\Lambda/c$ , where  $\beta$  is the axial wave vector component,  $\Lambda$  the inter-hole spacing, and  $c$  the speed of light in vacuum. The maximum value of  $\beta$  is set by  $kn$ , where  $n$  is the refractive index of the medium in the region (air, silica, Ge:silica or PC) under consideration.

### 2.3.1 Index-Guiding

In the index-guiding mechanism, light is localized in areas with higher refractive indices. Conventional optical fibers belong to this group. Light is sometimes said to be guided by total internal reflection (TIR) with ray optics, and the discrete existence of modes explained by constructive interferences with wave optics. In addition, a holey micro-structured optical fiber with solid core also works under a similar mechanism known as modified total internal reflection (mTIR) ([Russell, 2003](#)).

In **Figure 2-3A** we see that the diagram is separated into four regions, with the slope of the boundaries specified by the refractive index of medium, i.e.,

$$\text{Slope} = \frac{\omega}{\beta c_0} = \frac{k c_0}{k n c_0} = \frac{1}{n}, \quad (2.1)$$

and effective refractive index ( $n_{eff}$ ) is defined for regions in between these boundaries as

$$n_{eff} = \frac{\beta}{k} = \frac{\beta c_0}{\omega}. \quad (2.2)$$

When frequency  $\omega$  is fixed,  $n_{eff}$  increases with  $\beta$ . For light to propagate, it requires that  $n_{eff} < n$ , where  $n$  is the refractive index of the medium. This infers that for  $\beta < kn$ , light is free to propagate, and for  $\beta > kn$ , it is evanescent. In a conventional single-mode fiber, the guiding of light works at points like **R**, where light is allowed to propagate in the Ge:silica core but not the silica cladding.

### 2.3.2 Photonic Bandgap Guiding

In the photonic bandgap guiding mechanism, the guiding of light is possible at points like **P** in **Figure 2-3b**, where light is allowed to propagate in the air- or silica- core but not in the PC cladding. Hollow-core PCFs (**Figure 2-2b**) are an example of this; light is confined by

the surrounding PC cladding to within the air-core. On the other hand, a PCF can also propagate light at points like **Q** in **Figure 2-3b** with index-guiding (mTIR), where light is allowed to propagate in silica but not in the PC cladding (**Figure 2-2a**). Finally, points located within the full photonic bandgaps in the cyan-shaded area, *2-PC&silica*, in **Figure 2-3b** enable solid-core PBG-guiding. In this case light is allowed to propagate in silica but not in the PC cladding due to the PBG effect (**Figure 2-2c**).

## 2.4 Photonic Liquid Crystal Fibers

Liquid crystal (LC), the fourth state of matter which has properties between those of liquid and those of solid crystal, was first discovered in 1888 by Austrian botanical physiologist Friedrich Reinitzer. LCs have found various application in modern technologies, in particular, liquid crystal displays (LCDs) and also the more general form, spatial light modulators.

By infiltrating the holes in PCF with liquid crystal, a new type of optical fibers, the photonic liquid crystal fiber (PLCF) is obtained. An initially index-guiding PCF (**Figure 2-2a**) can be converted to a PBG-guiding PLCF (**Figure 2-2c**). The liquid crystal placed in periodic holes gives high tunability to PLCFs that can be thermally, electrically, and optically controlled ([Wolinski et al., 2006](#); [Lee et al., 2010](#)), and brings various potential applications to the field of fiber optics. **Figure 2-4** shows an example of the tunability of the PLCF, after [Larsen et al., 2003](#).

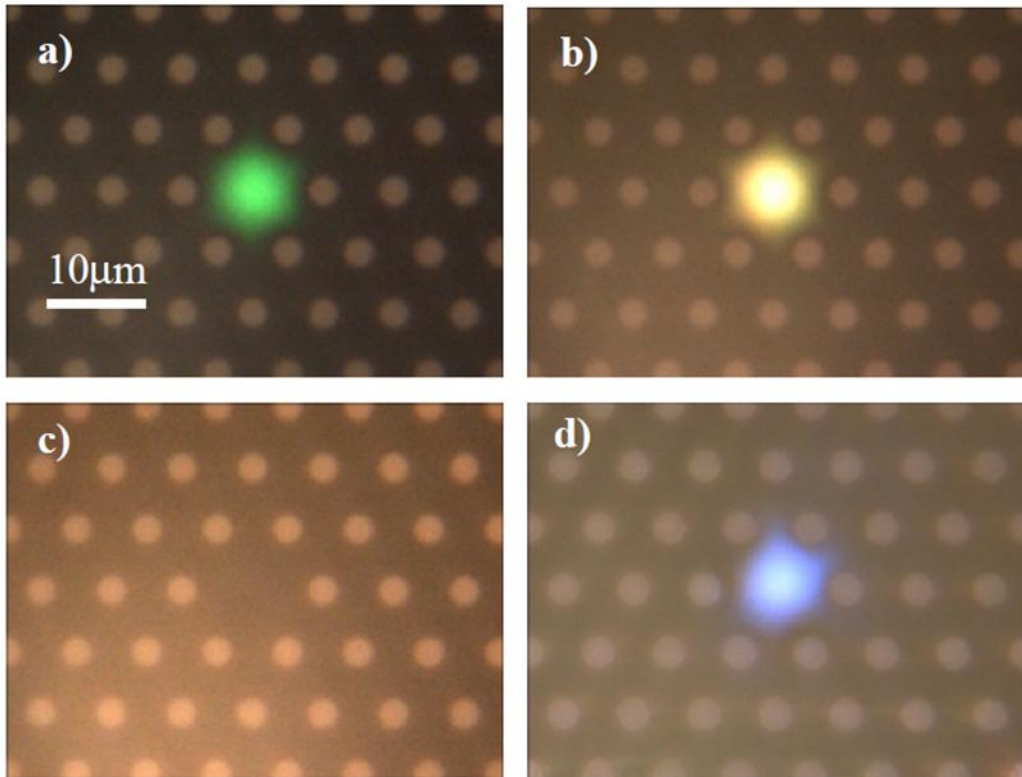


**Figure 2-4: A PCF filled with short-pitch chiral nematic liquid crystals ( $N^*LC$ ) shows PBG location sensitivity of  $1\text{nm}/^\circ\text{C}$  (visible) and  $3\text{nm}/^\circ\text{C}$  (infrared)**

The corresponding images are: a) Green,  $T=77^\circ\text{C}$ ; b) Yellow,  $T=89^\circ\text{C}$ ; c) Off state,  $T=91^\circ\text{C}$ ; d) Blue,  $T=94^\circ\text{C}$ . ([Larsen et al., 2003](#))

LCs are anisotropic, and, in most cases, have averaged refractive indices that are higher than that of silica. When we consider fibers geometries as shown in **Figure 2-2c**, PBG-guiding takes place in most cases. However, by changing the glass substrate to higher refractive index material or choosing LC with lower refractive index, it is also possible to achieve index-guiding. Furthermore, the refractive index of LC can also be engineered and/or tuned with temperature so that both index-guiding and PBG-guiding are possible with the same PLCF ([Wolinski et al., 2006](#)).

### 3 Numerical Modeling Schemes

In this chapter various numerical schemes for the characterization of optical fibers are discussed. Related work and publications are reviewed by [Chiang, 1994](#), [Scarmozzino et al., 2000](#) and [Saitoh and Koshiba, 2005](#). The classification shown in the last paper is adopted in [Section 3.2](#).

#### 3.1 Theory for Optical Fiber Modeling

##### 3.1.1 Maxwell Equations

The macroscopic Maxwell equations are:

$$\nabla \cdot D = \rho, \quad (3.1)$$

$$\nabla \cdot B = 0, \quad (3.2)$$

$$\nabla \times E = -\frac{\partial B}{\partial t}, \quad (3.3)$$

$$\nabla \times H = J + \frac{\partial D}{\partial t}, \quad (3.4)$$

where

$D$  = Electric induction,

$B$  = Magnetic induction,

$E$  = Electric field,

$H$  = Magnetic field,

$\rho$  = Charge density,

$J$  = Current density,

and the vector notations are neglected to point out mainly the form of equations. In the context of this thesis, we focus on non-magnetic ( $\mu_r = 1$ ,  $\mu = \mu_0$ ,  $B = \mu_0 H$ , where  $\mu$  is the permeability,  $\mu_0$  the permeability in vacuum, and  $\mu_r$  the relative permeability), source-free ( $\rho = 0$ ,  $J = 0$ ) media. The corresponding reduced equations are:

$$\nabla \cdot D = 0, \quad (3.5)$$

$$\nabla \cdot B = 0, \quad (3.6)$$

$$\nabla \times E = -\mu_0 \frac{\partial H}{\partial t}, \quad (3.7)$$

$$\nabla \times H = \frac{\partial D}{\partial t}. \quad (3.8)$$

### 3.1.2 Scalar-Field Formulation

When describing optical waveguides, very often Maxwell equations are introduced in the further reduced form where the vector nature of is dropped and results in the scalar wave formulation.

For an isotropic medium, within linear regime,

$$\underline{D} = \underline{\underline{\epsilon}} \underline{E} = \epsilon_0 \epsilon_r \underline{E}, \quad (3.9)$$

where  $\epsilon$  is the permittivity,  $\epsilon_0$  the permittivity of vacuum,  $\epsilon_r$  the relative permittivity, and the underlines indicate the tensor ranks. Assuming that the change in permittivity is negligible, i.e.,  $\epsilon$  is constant, we have the following relations

$$\nabla \cdot \underline{D} = \nabla \cdot (\epsilon_0 \epsilon_r \underline{E}) = \epsilon_0 \epsilon_r (\nabla \cdot \underline{E}) = 0, \quad \nabla \cdot \underline{E} = 0. \quad (3.10)$$

By performing curl operation on both sides of equation (3.7), we have

$$\nabla \times \nabla \times \underline{E} = -\mu_0 \frac{\partial(\nabla \times \underline{H})}{\partial t} = -\mu_0 \frac{\partial^2}{\partial t^2} \underline{D}. \quad (3.11)$$

With the vector algebra identity

$$\nabla \times \nabla \times F = \nabla(\nabla \cdot F) - \nabla \cdot (\nabla F), \quad (3.12)$$

and equations (3.8-9), we obtain the following equation that contains only the electric field,  $\underline{E}$ ,

$$\nabla(\nabla \cdot \underline{E}) - \nabla \cdot (\nabla \underline{E}) = -\mu_0 \epsilon_0 \epsilon_r \frac{\partial^2}{\partial t^2} \underline{E}. \quad (3.13)$$

Equation 3.10 shows that the divergence of  $\underline{E}$  is zero, and therefore

$$\nabla^2 \underline{E} = \mu_0 \epsilon_0 \epsilon_r \frac{\partial^2}{\partial t^2} \underline{E}. \quad (3.14)$$

We obtain the wave equation, which relates the spatial derivatives with the temporal derivatives. Similarly, starting from magnetic fields, we obtain the following differential equation:

$$\nabla^2 \underline{H} = \mu_0 \epsilon_0 \epsilon_r \frac{\partial^2}{\partial t^2} \underline{H}. \quad (3.15)$$

In equations (3.14) and (3.15), we see that the field  $\underline{f}(x, y, z, t)$  components,  $\underline{E}:Ex-Ey-Ez$  and  $\underline{H}:Hx-Hy-Hz$ , in each equation can be decoupled as there is no coupling among them. The scalar-field formulation is thus sufficient, and hence in the following we drop the first-rank tensor notation of the E- and H- fields. Additionally, we assume certain time and space dependence of the fields in the optical fibers, i.e.,

$$F(x, y, z, t) = F(x, y) \exp[i(\beta z - \omega_0 t)] = F_T \exp[i(\beta z - \omega_0 t)], \quad (3.16)$$

where  $\mathbf{F}$  can be either the electric field/induction ( $\mathbf{E}, \mathbf{D}$ ) or the magnetic field/induction ( $\mathbf{H}, \mathbf{B}$ ), and the  $T$  subscript denotes the transverse component of the field, known as the modes. The coefficients in the exponential terms are referred to as the propagation constant ( $\beta$ ) and angular frequency ( $\omega$ ). In this thesis we focus on frequency domain analysis, therefore the angular frequency is fixed and denoted as  $\omega_0$ . Accordingly, we reduce the  $z$ - and  $t$ - derivatives of the fields as follows:

$$\frac{\partial}{\partial t} = -i\omega_0, \quad \frac{\partial^2}{\partial t^2} = -\omega_0^2, \quad (3.17)$$

and

$$\frac{\partial}{\partial z} = i\beta, \quad \frac{\partial^2}{\partial z^2} = -\beta^2. \quad (3.18)$$

Equation (3.14) becomes

$$(\nabla_T^2 - \beta^2)E_T = -\mu_0\epsilon_0\epsilon_r\omega_0^2 E_T, \quad (3.19)$$

where the common exponential terms are omitted on both sides of the equation, and the Laplace operator is separated into the transverse and the longitudinal ( $z$ -) components,

$$\nabla^2 = \nabla_T^2 + \frac{\partial^2}{\partial z^2}. \quad (3.20)$$

By introducing

$$k = \frac{\omega_0}{c} = nk_0 = n \frac{\omega_0}{c_0} = \sqrt{\epsilon_r} \frac{\omega_0}{c_0}, \quad (3.21)$$

where  $\mathbf{k}$  is the wave vector,  $c$  the speed of light in the material considered,  $c_0$  the speed of light in vacuum,  $n$  the refractive index, and

$$c_0 = \frac{1}{\sqrt{\mu_0\epsilon_0}} \leftrightarrow \mu_0\epsilon_0 = \frac{1}{c_0^2}, \quad (3.22)$$

together with some rearrangement, we rewrite equation (3.19) in the following form:

$$(\nabla_T^2 + k_0^2\epsilon_r)E_T = \beta^2 E_T. \quad (3.23)$$

One can immediate identify equation (3.23) as an eigenvalue problem. Such problem can be solved by the scalar-field finite difference methods in frequency domain (FDFD) later discussed in **Section 4.1**. In our scalar-field FDFD formulation, the transverse Laplace operator is expanded in the Cartesian coordinate,

$$\nabla_T^2 = \frac{\partial^2}{\partial x^2} + \frac{\partial^2}{\partial y^2}, \quad E_T = E_T(x, y). \quad (3.24)$$

However, the differential equations can be solved analytically by expanding the transverse Laplace operator in cylindrical coordinates,

$$\nabla_T^2 = \frac{1}{r} \frac{\partial}{\partial r} \left( r \frac{\partial}{\partial r} \right) + \frac{1}{r^2} \frac{\partial^2}{\partial \theta^2}, \quad E_T = E_T(r, \theta), \quad (3.25)$$

which correspond to the cylindrical appearance of typical optical fibers. In this case, equation (3.23) results in the more familiar form in fiber optics textbooks,

$$\left[ \frac{\partial^2}{\partial r^2} + \frac{1}{r} \frac{\partial}{\partial r} + \frac{1}{r^2} \frac{\partial^2}{\partial \theta^2} + k_0^2 \epsilon_r \right] E_T(r, \theta) = \beta^2 E_T(r, \theta). \quad (3.26)$$

With the technique of separation of variables, we have

$$E_T(r, \theta) = R(r)\Theta(\theta) \quad (3.27)$$

and therefore

$$\begin{aligned} & \left[ \left( \frac{d^2}{dr^2} R(r) \right) \Theta(\theta) + \frac{1}{r} \left( \frac{\partial}{\partial r} R(r) \right) \Theta(\theta) + \frac{1}{r^2} R(r) \left( \frac{\partial^2}{\partial \theta^2} \Theta(\theta) \right) \right. \\ & \left. + k_0^2 \epsilon_r R(r) \Theta(\theta) \right] = \beta^2 R(r) \Theta(\theta). \end{aligned} \quad (3.28)$$

Scaling the above equation by  $\frac{r^2}{R\Theta}$ , we have

$$\begin{aligned} & \left[ \frac{r^2}{R(r)} \left( \frac{d^2}{dr^2} R(r) \right) + \frac{r}{R(r)} \left( \frac{d}{dr} R(r) \right) + \frac{1}{\Theta(\theta)} \left( \frac{d^2}{d\theta^2} \Theta(\theta) \right) + k_0^2 \epsilon_r r^2 \right] \\ & = \beta^2 r^2, \end{aligned} \quad (3.29)$$

and rearrange the formula so that only one variable is on one side of the equation:

$$\begin{aligned} & \left[ \frac{r^2}{R(r)} \left( \frac{d^2}{dr^2} R(r) \right) + \frac{r}{R(r)} \left( \frac{d}{dr} R(r) \right) + r^2 (k_0^2 \epsilon_r - \beta^2) \right] \\ & = -\frac{1}{\Theta(\theta)} \left( \frac{d^2}{d\theta^2} \Theta(\theta) \right). \end{aligned} \quad (3.30)$$

Physically, we know that  $\Theta(\theta)$  is  $2\pi$ -periodic:

$$-\frac{1}{\Theta(\theta)} \left( \frac{d^2}{d\theta^2} \Theta(\theta) \right) = l^2, \quad l \in N. \quad (3.31)$$

Therefore we can rewrite equation (3.29) into two equations with single variable coupled by  $l$ ,

$$\left[ \frac{r^2}{R(r)} \left( \frac{d^2}{dr^2} R(r) \right) + \frac{r}{R(r)} \left( \frac{d}{dr} R(r) \right) - \left( n^2(r) + \beta^2 \frac{\omega_0^2}{c_0^2} \right) r^2 \right] = l^2 \quad (3.32)$$

and

$$\left( \frac{d^2}{d\theta^2} \Theta(\theta) \right) + l^2 \Theta(\theta) = 0. \quad (3.33)$$

From these two equations we can derive the linearly polarized  $LP_{lm}$  modes ([Gloge, 1971](#)).

We demonstrate the linearly polarized approximation with scalar-field formulation in order to show the effectiveness and accuracy of finite-difference methods. This will be discussed in **Chapter 4** together with details of our scalar-field FDFD formulation.

### 3.1.3 Vector-Field Formulation

On the other hand, either the change in refractive index is significant or polarization properties are to be included, the vector-field formulation has to be introduced. Accordingly, two vector fields -- each with three scalar components -- are considered, the electric field  $\underline{E}$ : $E_x$ - $E_y$ - $E_z$ , and the magnetic field  $\underline{H}$ : $H_x$ - $H_y$ - $H_z$ , which are expressed in Cartesian coordinates. Maxwell equations govern the generation and evolution of all these fields, with every of them closely related, as well as the electromagnetic properties of matter, the permittivity  $\epsilon$  and the permeability  $\mu$ . Consequently, the vector-field formulation is more complicated than the scalar-field formulation as various cross coupling terms have to be accounted. However, depending on the permittivity and the permeability tensors of the material, with proper mathematical treatment, some fields can still be decoupled.

Again, starting from the curl Maxwell equations (3.7-8), and after dropping the t-derivative by assuming time dependence  $\exp(i\omega_0 t)$ , we have:

$$\nabla \times \underline{E} = -i\omega_0 \mu_0 \underline{H}, \quad (3.34)$$

$$\nabla \times \underline{H} = i\omega_0 \underline{D}. \quad (3.35)$$

Considering an anisotropic medium, within linear regime, we have

$$\underline{D} = \underline{\epsilon} \underline{E} = \epsilon_0 \underline{\epsilon}_r \underline{E}. \quad (3.36)$$

Performing curl operation on equation (3.33), we have:

$$\nabla \times \nabla \times \underline{E} = -i\omega_0 \mu_0 (\nabla \times \underline{H}) = \omega_0^2 \epsilon_0 \mu_0 \underline{\epsilon}_r \underline{E} = \underline{\epsilon}_r k_0^2 \underline{E}, \quad (3.37)$$

where some replacements are made according to equations (3.21-22). According to equation (3.5), with vector algebra identity, we have

$$\nabla \cdot \underline{D} = \nabla \cdot (\epsilon_0 \underline{\epsilon}_r \underline{E}) = \epsilon_0 (\nabla \cdot \underline{\epsilon}_r) \cdot \underline{E} + \epsilon_0 \underline{\epsilon}_r (\nabla \cdot \underline{E}) = 0, \quad (3.38)$$

which implies

$$\nabla \cdot \underline{\underline{E}} = - \frac{\nabla \underline{\underline{\epsilon}_r}}{\underline{\underline{\epsilon}_r}} \cdot \underline{\underline{E}}. \quad (3.39)$$

It should be noted the difference between equations (3.38) and (3.10) in view of vector algebra. Together with the vector algebra identity (3.12), we have

$$\nabla \times \nabla \times \underline{\underline{E}} = \nabla(\nabla \cdot \underline{\underline{E}}) - \nabla \cdot (\nabla \underline{\underline{E}}) = -\nabla \left( \frac{\nabla \underline{\underline{\epsilon}_r}}{\underline{\underline{\epsilon}_r}} \cdot \underline{\underline{E}} \right) - \nabla^2 \underline{\underline{E}}. \quad (3.40)$$

Combining equations (3.37) and (3.40), we have

$$\nabla^2 \underline{\underline{E}} + \nabla \left( \frac{\nabla \underline{\underline{\epsilon}_r}}{\underline{\underline{\epsilon}_r}} \cdot \underline{\underline{E}} \right) + k_0^2 \underline{\underline{\epsilon}_r} \underline{\underline{E}} = 0. \quad (3.41)$$

In order to compare equation (3.41) with equation (3.23), we also separate the Laplace operator into longitudinal and transverse components with the help of equations (3.18) and (3.20), and drop the common exponential term on both sides of the equation. This results in

$$\nabla_T^2 \underline{\underline{E}_T} + \nabla \left( \frac{\nabla \underline{\underline{\epsilon}_r}}{\underline{\underline{\epsilon}_r}} \cdot \underline{\underline{E}_T} \right) + k_0^2 \underline{\underline{\epsilon}_r} \underline{\underline{E}_T} = \beta^2 \underline{\underline{E}_T}. \quad (3.42)$$

We see that in the above equation, there exist two terms for which the coupling between fields is possible. One of them is related to the gradient of the permittivity tensor, and the other is related to material anisotropy. From equation (3.42) we see clearly that either when the change in refractive index is sharp or the material possesses non-diagonal anisotropy, the scalar-field LP approximation is no longer valid.

Similarly, performing again curl operation on the magnetic curl equation (3.34), we have

$$\nabla \times \nabla \times \underline{\underline{H}} = i\omega \epsilon_0 \nabla \times (\underline{\underline{\epsilon}_r} \underline{\underline{D}}) = i\omega \epsilon_0 \nabla \times (\underline{\underline{\epsilon}_r} \underline{\underline{E}}) = i\omega \epsilon_0 (\nabla \underline{\underline{\epsilon}_r} \times \underline{\underline{E}} + \underline{\underline{\epsilon}_r} \nabla \times \underline{\underline{E}}) \quad (3.43)$$

With the vector algebra identity (3.12), we have

$$\nabla \times \nabla \times \underline{\underline{H}} = \nabla(\nabla \cdot \underline{\underline{H}}) - \nabla \cdot (\nabla \underline{\underline{H}}) = -\nabla^2 \underline{\underline{H}}. \quad (3.44)$$

Combining equations (3.34-35) results in

$$\underline{\underline{E}} = \frac{1}{i\omega \epsilon_0 \underline{\underline{\epsilon}_r}} \nabla \times \underline{\underline{H}}. \quad (3.45)$$

Equations (3.43-45) show that

$$-\nabla^2 \underline{\underline{H}} = \nabla \underline{\underline{\epsilon}_r} \times \left( \frac{1}{\underline{\underline{\epsilon}_r}} \nabla \times \underline{\underline{H}} \right) + \omega^2 \epsilon_0 \mu_0 \underline{\underline{\epsilon}_r} \underline{\underline{H}}. \quad (3.46)$$

Rearranging the above equation we obtain the magnetic field counterpart of equation (3.41),

$$\nabla^2 \underline{H} + \frac{\nabla \epsilon_r}{\epsilon_r} \times (\nabla \times \underline{H}) + \epsilon_r k_0^2 \underline{H} = 0. \quad (3.47)$$

Either equation (3.41) or equation (3.47) can be applied as the starting point of the eigenvalue problem. However, in Chapter 2 of their book, [Joannopoulos et al., 2008](#) stated that for mathematical convenience, the equation with the magnetic field is preferred for numerical calculations. In our vector-field FDFD formulation, this is not a concern as neither is used. Instead, we followed the formulation based only on the two curl equations proposed by [Zhu and Brown, 2002](#). Details regarding our vector-field FDFD formulation are discussed in [Chapter 4](#).

In this section, we have theoretically shown the limits of the commonly-known scalar-field LP approximation for the characterization of optical fibers. The magnitude of differences between the vector-field formulation and the scalar-field LP approximation are given and discussed in [Section 4.7](#).

Now that we have reviewed the related theory, which is mostly Maxwell's electromagnetism, we proceed to the next part where various numerical schemes are briefed.

### 3.2 Overview of Characterization Methods for Microstructured Optical Fibers

We recall that in this section we follow the paper by [Saitoh and Koshiba, 2005](#), where modeling methods for PCFs are categorized into three types of approaches. They are:

- 1) Effective-Index Approach,
- 2) Basis-Function Expansion Approach, and
- 3) Numerical Approach.

In the following sections, the advantages and disadvantages of each modeling method is briefed and discussed with an emphasis set on the characterization of PLCFs. It is encouraged to consult the mentioned paper for further details regarding various characterization approaches for PCFs. To begin with, we draw a schematic representation of a triangular-lattice PCF, as shown in [Figure 3-1](#). The defect in the center of the periodic air holes is referred to as the core, while the PC functions as the cladding.

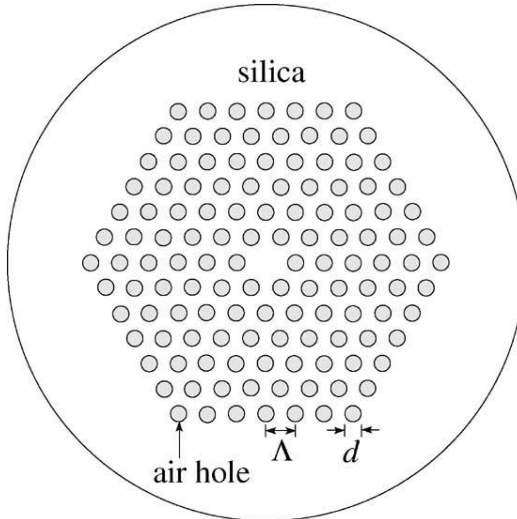


**Figure 3-1: Schematic of a triangular-lattice PCF**

The PCF is characterized by the hole diameter  $d$ , the pitch of holes  $\Lambda$ , and the number of the rings of holes (e.g., in this plot, there are six rings).

Depending on whether the air holes are infiltrated or not, and then on the refractive index of the infiltrating material, we can categorize PCF geometries into several different types, as already shown in [Figure 2-2](#).

### 3.2.1 Effective Index Approach

In [Section 3.1](#) we discussed briefly the scalar-field LP approximation. Although its use is limited, it nevertheless gives basic ideas on how light propagates in an optical fiber. In a standard step-index fiber with core radius  $\rho$  and core and cladding refractive indices  $n_{core}$  and  $n_{clad}$ , the number of guided modes is determined by the normalized frequency, also known as the  $V$  parameter ([Snyder and Love, 1983](#)):

$$V = \frac{2\pi}{\lambda} \rho \sqrt{n_{core}^2 - n_{clad}^2}. \quad (3.48)$$

To quantify the requirement for monomode operation in an index-guiding PCF, [Birks et al., 1997](#) and [Knight et al., 1998](#) extended the use of the  $V$  parameter by proposing a simple scalar model using an effective refractive index for the cladding,  $n_{clad,eff}$ , which is determined by the propagation constant of the fundamental space-filling mode ( $\beta_{FSM}$ ) of the PC cladding,

$$n_{clad,eff} = \frac{\beta_{FSM}}{k}, \quad k = \frac{2\pi}{\lambda}. \quad (3.49)$$

In this sense, one can extend the guiding requirement for the modal propagation constant  $\beta$  of a conventional step-index fiber to that of a PCF,

$$kn_{\text{silica}} > \beta > \beta_{\text{FSM}} = kn_{\text{clad,eff}}. \quad (3.50)$$

The propagation constants of the fundamental space-filling modes can be calculated by solving wave equations within a unit cell of the photonic crystal centered on one of the air holes with Neumann boundary condition along the axes of symmetry.

### 3.2.2 Basis-Function Expansion Approach

The effective index approach gives simple and qualitative descriptions of PCFs based on the extended  $V$  parameter. However, it does not give quantitative results for modal propagation constants nor the dispersion properties of PCFs. These properties strongly depend on the PCF geometries, which are not accounted in the effective index approach. Moreover, since a scalar model is used, it is insufficient to describe the properties related to the polarization of light and material anisotropy.

To extend the scope of characterizations, various vector models using different basis functions for PCFs have been proposed. One of the most widely used is the plane wave expansion (PWE) method. As the name suggests, the electromagnetic fields are expanded according to the plane wave basis. The fiber geometry, i.e. the permittivity profile is expressed by Fourier series. Other alternative methods are the localized function method (LFM) and the multipole method (MM).

### 3.2.3 Numerical Approach

The basis-function expansion approach takes advantage of the simplicity of periodic structures of a PCF with circular holes, and gives decent information about light propagation therein. However, for more complicated fiber structures consisting for example of non-circular hole, as in suspended core fibers, it is no longer applicable. Moreover, it also fails when applied to optical fibers with longitudinal permittivity variations, which is in general the case for PLCFs as LCs are not perfectly crystalline. Numerous direct numerical methods have been proposed to analyze general fiber structures and can be divided in the following categories:

- 1) Finite Element Methods (FEM)
- 2) Boundary Element Methods (BEM)

- 3) Beam Propagation Method (BPM)
- 4) Finite Difference Methods in Frequency Domain (FDM/FDFD)
- 5) Finite Difference Methods in Time Domain (FDTD)

The numerical approach is what we focus on later throughout the thesis. For the characterization of PLCFs, we will not go through all the categories in details but rather focus on and will discuss about FDFD and BPM in the next section.

### 3.2.4 Choices for PLCF Characterization

To find out what numerical methods are suitable for PLCF characterization, we first have to know the properties of a common PLCF while keeping in mind the advantages and disadvantages of the numerical methods. Two important aspects should be mentioned for the characterization of PLCFs. The first one is the material anisotropy that comes with liquid crystal. As discussed in **Section 3.1.3**, the more complicated the permittivity tensor, the more complex the numerical problem is, as fields are less likely to be decoupled from each other. The other aspect comes from the geometry of the PCF host. A PCF is larger in transverse extent compared to conventional single-mode fibers, but meanwhile has smaller radius of curvatures of changes in the refractive index profile. The former indicates that a bigger calculation window is necessary, and the latter suggests finer grids with smaller step size is required. Both aspects pose challenges in the characterization of PLCFs, and are discussed in the following.

#### Material Anisotropy

As previously discussed, both material anisotropy and high index-contrast require the use of vector-field formulation. Moreover, from the material side, when the crystal axes do not coincide with the axes of the fields ( $E_x, E_y, E_z, H_x, H_y, H_z$ ), the form of the permittivity tensor also has to be considered. This is further discussed in **Sections 4.2-3**. There have been various studies on vector-field FDFDs and BPMs for characterizations of optical elements ranging from conventional fibers to PCFs and anisotropic waveguides. When the optical fiber is homogeneous along the propagation (z-) axis, two-dimensional (2D) FDFD is sufficient, and that was the main focus in literature. When there exists inhomogeneity along the z-axis, three-dimensional (3D) BPM is often favored. 3D-BPM is also useful in characterizing fiber optics elements such as couplers. An alternative way to treat the z-inhomogeneity of a PLCF is to consider 3D-FDFD over a certain period. For example, recently [Ivinskaya et al., 2010](#) applied 3D-FDFD to characterize photonic nanocavities in contrast to the time domain methods. The formulation of 2D-FDFD, even if considering

material anisotropy, is relatively compact, while for 3D-BPM, it is more complicated. This explains partly why we choose FDFD to be our fundamental numerical tool for the characterization of PLCFs.

### Size of PLCF

Optical fibers are small in size from normal perception. For a typical PCF structure, the diameter is only of about **100µm**. However, when compared to the wavelength of light, this corresponds to about **60λ** in the telecommunication range and **200λ** in the visible range. This is extremely large for finite-difference numerical simulations, as the computational resolution and window are often specified with respect to wavelength. For example, **20λ-by-20λ** is regarded as ‘large domain size’ in FDTD. For 2D-FDFD, It has been reported that **λ/15** yields fairly accurate results ([Zhu and Brown, 2002](#)). Summing up all these factors, characterization of PLCF is demanding and therefore numerically expensive to be performed with time domain methods as extra memory storage for time steps are required in addition to the discretized spatial domain. Even with frequency domain methods, the simulation margin is also limited. Finite element methods and boundary element methods can reduce the number of points needed for the computations, but more effort is required to consider the vector fields and the material anisotropies. Fortunately, in most cases, even if only part of the periodic structure of a PCF/PLCF is considered in simulations, relevant results are obtained, as light is confined within a certain number of ‘rings’ in the periodic structure. Another advantage that comes with periodicity is the possibility to apply proper boundary condition that accounts for repeating cell structures.

To sum up, the reason for choosing FDFD is that the formulation is relatively simple, while BPM can be implemented to account for longitudinal variation (z-inhomogeneity) of a PLCF. It should also be noted that, in compliance with the objective of the thesis, FDFD and BPM are computationally less expensive and efficient, therefore extending their accessibility to commercial personal computers. The computed modal field distributions in FDFD can be used as the initial fields for BPM, which shall reduce the propagation distance and steps required for converged numerical results. In this thesis, more specifically, FDFD is implemented to study the characteristics of PLCFs. Both scalar-field and vector-field formulations are implemented for comparison. In the next chapter the FDFD schemes are described in detail. **Figure 3-2** gives an estimate on the computational effort for an exemplary PLCF geometry with vector-field FDFD. As one can see, the memory requirement is rather demanding.

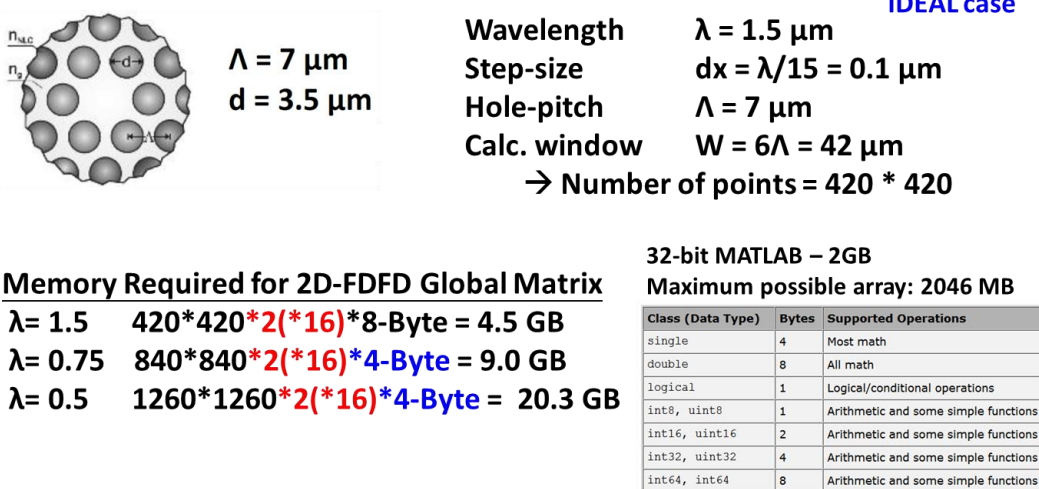


**Figure 3-2: Estimation on 2D-FDFD computational effort for an exemplary PLCF geometry with two coupling field components**

On the top we show an exemplary fiber geometry to be simulated. On the bottom-left we see that the required memory is large. The numbers in red parentheses specify the form of anisotropy, followed by the data type for storage. Requirement on memory can be reduced by using single-precision floating-point numbers than double-precision ones, however, for example, MATLAB 32-bit does not support single-precision sparse matrix. Simulations for fibers with photonic crystal structures are demanding. With MATLAB 32-bit, the maximum number of points allowed is approximately 350 by 350, when 48 eigenvalues are to be sought for an diagonally anisotropic PLCF.

## 4 Finite Difference Methods in Frequency Domain (FDM/ FDFD)

Maxwell equations (3.1-4) relate four vector fields ( $\mathbf{E}$ ,  $\mathbf{H}$ ,  $\mathbf{D}$ ,  $\mathbf{B}$ ) with four derivatives ( $\partial_x$ ,  $\partial_y$ ,  $\partial_z$ ,  $\partial_t$ ). The time derivative can be dropped by assuming time dependence  $\exp(-i\omega_0 t)$  of the fields, resulting in direct multiplication of  $-i\omega_0$ . This is the basis for frequency domain methods: only fields of a fixed optical frequency are considered. Assuming field dependence  $\exp(i\beta z)$  along the propagation axis  $z$ , the  $z$ -derivative is also reduced to direct multiplication of  $i\beta$ . Such field dependence in  $z$  forms the mode theory for electromagnetic fields propagating within an optical waveguide. A mode is said to have its field distribution unchanged along the propagation axis. Mathematically, modes are the possible solutions of wave equations.

The remaining  $x$ - and  $y$ - derivatives are approximated by finite-difference formulae. Having all four derivatives deduced, the Maxwell equations are solved numerically with specific geometry and property of the medium.

The above two paragraphs describe the idea behind FDFD, with also a touch on the mode theory of optical fibers. Conventionally, as derived in **Sections 3.1.2-3**, all four Maxwell equations are involved and result in wave equations where second-order derivatives appear. The corresponding related work includes [Bierwirth et al., 1986](#), [Stern, 1988](#), [Lüsse et al., 1994](#), and [Fallahkhair et al., 2008](#). On the other hand, [Zhu and Brown, 2002](#) first proposed a more compact FDFD scheme based on the two curl Maxwell equations and incorporated Yee's staggered mesh ([Yee, 1966](#)) to study the modal characteristics of MOFs. Numerous publications followed such FDFD scheme and extended its use to even more general fiber geometries ([Guo et al., 2004](#); [Yu and Chang, 2004](#); [Chen et al., 2009](#)). It is worth mentioning here that Yee's staggered mesh has been widely used in FDTD schemes owing to its effectiveness.

In this chapter, in order to gain some insight on FDFD, we first derive a scalar-field FDFD scheme based on the wave equations (3.14-15). The numerical results will then be compared, in particular, with its analytic counterpart given by the scalar-field LP approximation. Next, we discuss the material anisotropy involved in PLCFs and review corresponding work in literature. Finally, taking into consideration the computational accessibility and efficiency, we formulate our vector-field FDFD based on that of [Zhu and Brown, 2002](#) and extend its use to optical fibers with more general material anisotropy.

## 4.1 Scalar-Field FDFD

As derived in **Section 3.1.2**, combining equations (3.23-24), we obtain the following scalar-field eigenvalue problem,

$$\left( \frac{\partial^2}{\partial x^2} + \frac{\partial^2}{\partial y^2} + k_0^2 \epsilon_r \right) E_T = \beta^2 E_T. \quad (4.1)$$

One of the possibilities to approximate the second-order derivatives with respect to  $x$  and  $y$  are approximated is to use the three-point central finite differences (FDs) as shown in **Figure 4-1**. This gives us

$$\frac{\partial^2 U_{x,y}}{\partial x^2} = \frac{U_{x+1,y} - 2U_{x,y} + U_{x-1,y}}{\Delta x^2}, \quad \frac{\partial^2 U_{x,y}}{\partial y^2} = \frac{U_{x,y+1} - 2U_{x,y} + U_{x,y-1}}{\Delta y^2}. \quad (4.2)$$

Central and Non – Central Formula	Error Term
$f''(x_i) \approx \frac{-f(x_{i-3})+4f(x_{i-2})-5f(x_{i-1})+2f(x_i)}{h^2}$	$\frac{11}{12} h^2 f^{(4)}$
$f''(x_i) \approx \frac{f(x_{i-1})-2f(x_i)+f(x_{i+1})}{h^2}$	$\frac{1}{12} h^2 f^{(4)}$
$f''(x_i) \approx \frac{2f(x_i)-5f(x_{i+1})+4f(x_{i+2})-f(x_{i+3})}{h^2}$	$\frac{11}{12} h^2 f^{(4)}$
$f''(x_i) \approx \frac{-10f(x_{i-5})+61f(x_{i-4})-156f(x_{i-3})+214f(x_{i-2})-154f(x_{i-1})+45f(x_i)}{12h^2}$	$\frac{137}{180} h^4 f^{(6)}$
$f''(x_i) \approx \frac{f(x_{i-4})-6f(x_{i-3})+14f(x_{i-2})-4f(x_{i-1})-15f(x_i)+10f(x_{i+1})}{12h^2}$	$\frac{13}{180} h^4 f^{(6)}$
$f''(x_i) \approx \frac{-f(x_{i-2})+16f(x_{i-1})-30f(x_i)+16f(x_{i+1})-f(x_{i+2})}{12h^2}$	$\frac{1}{90} h^4 f^{(6)}$
$f''(x_i) \approx \frac{10f(x_{i-1})-15f(x_i)-4f(x_{i+1})+14f(x_{i+2})-6f(x_{i+3})+f(x_{i+4})}{12h^2}$	$\frac{13}{180} h^4 f^{(6)}$
$f''(x_i) \approx \frac{45f(x_i)-154f(x_{i+1})+214f(x_{i+2})-156f(x_{i+3})+61f(x_{i+4})-10f(x_{i+5})}{12h^2}$	$\frac{137}{180} h^4 f^{(6)}$
$f''(x_i) \approx \frac{-126f(x_{i-7})+1019f(x_{i-6})-3618f(x_{i-5})+7380f(x_{i-4})-9490f(x_{i-3})+7911f(x_{i-2})-4014f(x_{i-1})+938f(x_i)}{180h^2}$	$\frac{363}{560} h^6 f^{(8)}$
$f''(x_i) \approx \frac{11f(x_{i-6})-90f(x_{i-5})+324f(x_{i-4})-670f(x_{i-3})+855f(x_{i-2})-486f(x_{i-1})-70f(x_i)+126f(x_{i+1})}{180h^2}$	$\frac{29}{560} h^6 f^{(8)}$
$f''(x_i) \approx \frac{-2f(x_{i-5})+16f(x_{i-4})-54f(x_{i-3})+85f(x_{i-2})+130f(x_{i-1})-378f(x_i)+214f(x_{i+1})-11f(x_{i+2})}{180h^2}$	$\frac{47}{5040} h^6 f^{(8)}$
$f''(x_i) \approx \frac{2f(x_{i-3})-27f(x_{i-2})+270f(x_{i-1})-490f(x_i)+270f(x_{i+1})-27f(x_{i+2})+2f(x_{i+3})}{180h^2}$	$\frac{1}{560} h^6 f^{(8)}$
$f''(x_i) \approx \frac{-11f(x_{i-2})+214f(x_{i-1})-378f(x_i)+130f(x_{i+1})+85f(x_{i+2})-54f(x_{i+3})+16f(x_{i+4})-2f(x_{i+5})}{180h^2}$	$\frac{47}{5040} h^6 f^{(8)}$
$f''(x_i) \approx \frac{126f(x_{i-1})-70f(x_i)-486f(x_{i+1})+855f(x_{i+2})-670f(x_{i+3})+324f(x_{i+4})-90f(x_{i+5})+11f(x_{i+6})}{180h^2}$	$\frac{29}{560} h^6 f^{(8)}$
$f''(x_i) \approx \frac{938f(x_i)-4014f(x_{i+1})+7911f(x_{i+2})-9490f(x_{i+3})+7380f(x_{i+4})-3618f(x_{i+5})+1019f(x_{i+6})-126f(x_{i+7})}{180h^2}$	$\frac{363}{560} h^6 f^{(8)}$

**Figure 4-1: Finite-difference formulae for 2<sup>nd</sup>-order differentiation**

The three-term central difference for 2<sup>nd</sup>-order derivative (second formula from the top) is implemented in our scalar-field FDFD scheme, as derived in Equation (4.2).

The eigenvalue problem is then discretized as

$$\begin{aligned} & \left( \frac{-2}{\Delta x^2} + \frac{-2}{\Delta y^2} + k_0^2 \epsilon_r \right) E_{x,y} + \left( \frac{1}{\Delta x^2} \right) E_{x-1,y} + \left( \frac{1}{\Delta x^2} \right) E_{x+1,y} \\ & + \left( \frac{1}{\Delta y^2} \right) E_{x,y-1} + \left( \frac{1}{\Delta y^2} \right) E_{x,y+1} = \beta^2 E_{x,y}. \end{aligned} \quad (4.3)$$

We can see that at each point of the mesh grid,  $E(x,y)$  is associated with itself and another four neighboring points. This can be represented in the matrix form as shown in **Figure 4-2**. In FDFD, such matrix is referred to as the global matrix. The eigenvalues of the global matrix give access to the effective refractive indices ( $n_{eff} = \beta/k_0$ ) of the modes and the eigenvectors give the modal field patterns. We note that the full size of the global matrix is  $(M \times N)^2$ , where  $M$  and  $N$  grid points are used to represent the fiber geometry in the  $x$ - and  $y$ - dimensions, respectively. One can immediately see that in this case the use of memory is inefficient if full matrix is registered. Fortunately, with the development of sparse matrix packages, we can reduce significantly the requirement on memory. For example, in the three-point FD case, the memory required is reduced from  $(M \times N)^2$  to  $(M \times N) \times 5$ . Given  $M = N = 100$ , the reduction factor is already **2000**, and further increases dramatically with the number of grid points used.

More accurate finite-difference schemes for the approximation of second-order derivatives (**Figure 4-1**) can be utilized to reduce approximation errors at the cost of a more complex global matrix. We will validate the accuracy of the three-point scalar-field FDFD with comparison to the analytic scalar-field LP approximation in **Section 4.7**. The **MATLAB** code implemented for scalar-field FDFD is given in **Appendix A**. Despite its simplicity, it is worth mentioning that [Riishede et al., 2003](#) has also applied the scalar-field FDFD to the modeling of MOFs.

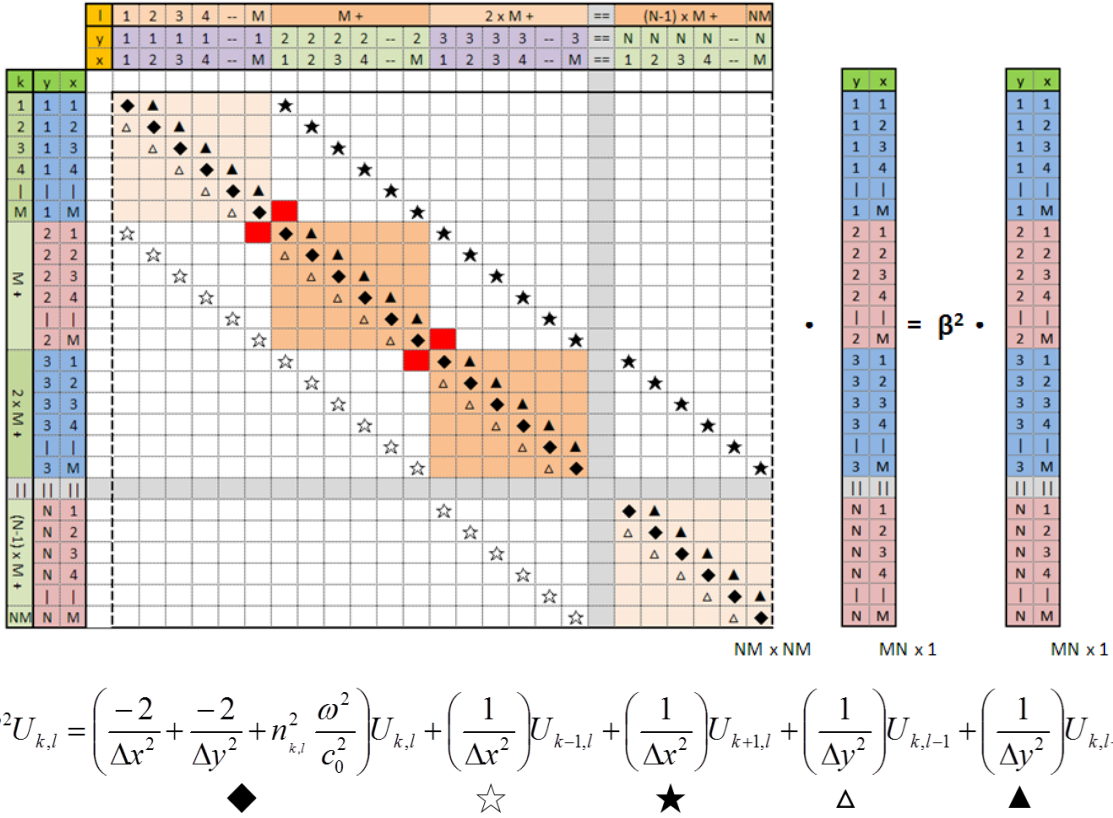


**Figure 4-2: Discretized scalar-field eigenvalue problem with corresponding global matrix**

In our matrix arrangement ( $[y, x]$ ;  $y$  is the major index and  $x$  is the minor index), the horizontal borders (dashed lines) of the global matrix corresponds to the boundaries in the  $y$  dimension, while the boundaries in the  $x$  dimension are colored in red.

## 4.2 Material Anisotropy in FDFD

In this work we set our focus in the characterization of more general optical fiber geometries, with an emphasis on PLCFs, therefore we have to consider the anisotropic properties of liquid crystals. So far some FDFD studies on light propagation in waveguides with material anisotropy have been reported. For example, [Zhu and Brown, 2002](#) proposed a FDFD scheme for optical fibers that is capable of taking into account the diagonal anisotropy. [Fallahkhair et al., 2008](#) reported a FDFD scheme that accounts for the transverse anisotropy in waveguides. [Chen et al., 2009](#) further considered the general anisotropy and tested their FDFD scheme with an anisotropic waveguide and an LC-core waveguide. The formulations of [Zhu and Brown, 2002](#) and [Chen et al., 2009](#), as mentioned in the beginning of this chapter, are based on the curl Maxwell equations, and only the first-order derivatives are required in the finite-difference scheme. [Fallahkhair et al., 2008](#),

on the other hand, introduces also the divergence Maxwell equations and require second-order derivatives in the finite difference scheme.

In the following, we start with the vector-field FDFD proposed by [Zhu and Brown, 2002](#) for its simplicity and use of Yee's staggered mesh, which reduces the number of grid points by a factor of two for a fixed fiber geometry. This is beneficial in the characterization of structures which are large in size. By introducing some correction terms, we have extended the FDFD to include transverse material anisotropies.

### 4.3 Vector-Field FDFD

Starting from equations (3.7-8), along with equations (3.16-17, 19-20), we replace the  $t$ - and  $z$ - derivatives of the two curl Maxwell equations and result in the following coupled equations of the vector-field components,

$$\begin{aligned} i\omega_0\mu_0H_x &= \frac{\partial E_z}{\partial y} - i\beta E_y \\ i\omega_0\mu_0H_y &= i\beta E_x - \frac{\partial E_z}{\partial x} \\ i\omega_0\mu_0H_z &= \frac{\partial E_y}{\partial x} - \frac{\partial E_x}{\partial y} \end{aligned} \tag{4.4}$$

and

$$\begin{aligned} -i\omega_0D_x &= \frac{\partial H_z}{\partial y} - i\beta H_y \\ -i\omega_0D_y &= i\beta H_x - \frac{\partial H_z}{\partial x} \\ -i\omega_0D_z &= \frac{\partial H_y}{\partial x} - \frac{\partial H_x}{\partial y}. \end{aligned} \tag{4.5}$$

To simplify the notations, we introduce the free space impedance  $Z_0$ ,

$$Z_0 = \sqrt{\frac{\mu_0}{\epsilon_0}}, \tag{4.6}$$

to replace both  $\mu_0$  and  $\epsilon_0$  by

$$\omega_0\mu_0 = k_0 Z_0, \quad \omega_0\epsilon_0 = \frac{k_0}{Z_0}, \tag{4.7}$$

and result in the following two sets of coupled equations,

$$\begin{aligned}
ik_0 Z_0 H_x &= \frac{\partial E_z}{\partial y} - i\beta E_y \\
ik_0 Z_0 H_y &= i\beta E_x - \frac{\partial E_z}{\partial x} \\
ik_0 Z_0 H_z &= \frac{\partial E_y}{\partial x} - \frac{\partial E_x}{\partial y},
\end{aligned} \tag{4.8}$$

and

$$\begin{aligned}
-ik_0 \frac{1}{\epsilon_0 Z_0} D_x &= \frac{\partial H_z}{\partial y} - i\beta H_y \\
-ik_0 \frac{1}{\epsilon_0 Z_0} D_y &= i\beta H_x - \frac{\partial H_z}{\partial x} \\
-ik_0 \frac{1}{\epsilon_0 Z_0} D_z &= \frac{\partial H_y}{\partial x} - \frac{\partial H_x}{\partial y}.
\end{aligned} \tag{4.9}$$

Since in an eigenvalue problem, the magnitude of the eigenfield (eigenvector) does not have physical meanings, we can further simplify the equations by scaling the electric field/induction  $\mathbf{E}, \mathbf{D}$  with respect to the magnetic field/induction  $\mathbf{H}, \mathbf{B}$ ,

$$E' = \frac{E}{Z_0}, \quad D' = \frac{D}{Z_0}. \tag{4.10}$$

This removes  $Z_0$  and its inverse terms from the coupled equations. Also, for simplicity, we drop the prime (') notations on  $\mathbf{D}$  and  $\mathbf{E}$  and arrive at the following equations,

$$\begin{aligned}
ik_0 H_x &= \frac{\partial E_z}{\partial y} - i\beta E_y \\
ik_0 H_y &= i\beta E_x - \frac{\partial E_z}{\partial x} \\
ik_0 H_z &= \frac{\partial E_y}{\partial x} - \frac{\partial E_x}{\partial y},
\end{aligned} \tag{4.11}$$

$$\begin{aligned}
-ik_0 \frac{1}{\epsilon_0} D_x &= \frac{\partial H_z}{\partial y} - i\beta H_y \\
-ik_0 \frac{1}{\epsilon_0} D_y &= i\beta H_x - \frac{\partial H_z}{\partial x} \\
-ik_0 \frac{1}{\epsilon_0} D_z &= \frac{\partial H_y}{\partial x} - \frac{\partial H_x}{\partial y}.
\end{aligned} \tag{4.12}$$

The finite differences are then incorporated to obtain the  $x$ - and  $y$ - derivatives. Various discretization schemes have been proposed among which the staggered mesh proposed by [Yee, 1966](#) has shown its effectiveness and accuracy. We adopt the Yee mesh configuration that is shown in [Figure 4-3](#). Discretizing equations (4.11-12) accordingly leads to

$$\begin{aligned} ik_0 H_x(k, l) &= \frac{E_z(k, l+1) - E_z(k, l)}{\Delta y} - i\beta E_y(k, l) \\ ik_0 H_y(k, l) &= i\beta E_x(k, l) - \frac{E_z(k+1, l) - E_z(k, l)}{\Delta x} \end{aligned} \quad (4.13)$$

$$\begin{aligned} ik_0 H_z(k, l) &= \frac{E_y(k+1, l) - E_y(k, l)}{\Delta x} - \frac{E_x(k, l+1) - E_x(k, l)}{\Delta y}, \\ -ik_0 \frac{1}{\epsilon_0} D_x(k, l) &= \frac{H_z(k, l) - H_z(k, l-1)}{\Delta y} - i\beta H_y(k, l) \\ -ik_0 \frac{1}{\epsilon_0} D_y(k, l) &= i\beta H_x(k, l) - \frac{H_z(k, l) - H_z(k-1, l)}{\Delta x} \\ -ik_0 \frac{1}{\epsilon_0} D_z(k, l) &= \frac{H_y(k+1, l) - H_y(k, l)}{\Delta x} - \frac{H_x(k, l+1) - H_x(k, l)}{\Delta y}. \end{aligned} \quad (4.14)$$

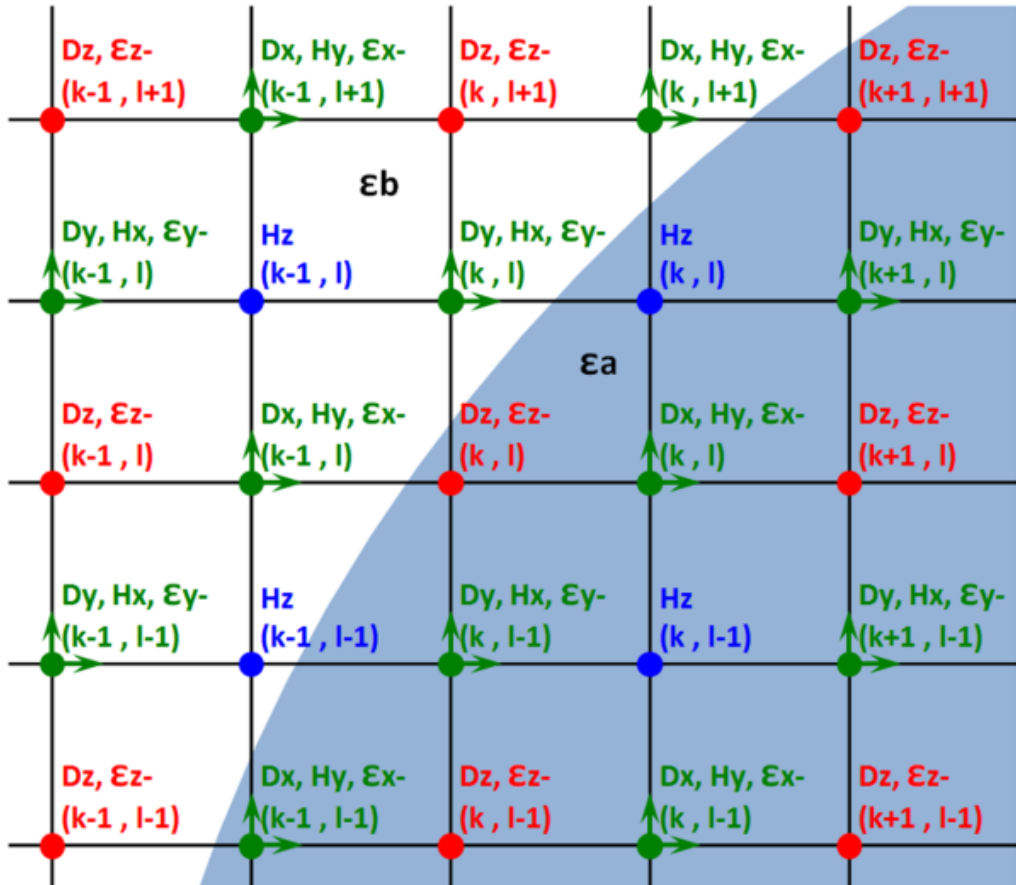


Figure 4-3: The staggered Yee mesh configuration for the vector-field FDFD implemented

An exemplary boundary for regions with permittivities  $\epsilon_a$  and  $\epsilon_b$  is drawn and the region with  $\epsilon_a$  is shaded in blue.

Since we consider non-magnetic materials, the relation between  $\mathbf{B}$  and  $\mathbf{H}$ , described by the permeability  $\mu$ , is readily accounted in the formulation. Next, in order to couple the sets of equations, (4.4-5) or (4.11-12), we consider the relation between  $\mathbf{D}$  and  $\mathbf{E}$ , described by the permittivity  $\epsilon$ . We limit ourselves to linear regime where the permittivity  $\epsilon$  is in the form of a second-rank tensor (i.e., a 3-by-3 matrix). In this sense the material anisotropy falls into four possible forms of permittivity tensors, as shown in **Table 4-1**.

**Table 4-1: Material anisotropy and corresponding permittivity tensor form**

<b>a</b>	<b>b</b>	<b>c</b>	<b>d</b>
$\begin{bmatrix} \epsilon_r & 0 & 0 \\ 0 & \epsilon_r & 0 \\ 0 & 0 & \epsilon_r \end{bmatrix}$	$\begin{bmatrix} \epsilon_{r,xx} & 0 & 0 \\ 0 & \epsilon_{r,yy} & 0 \\ 0 & 0 & \epsilon_{r,zz} \end{bmatrix}$	$\begin{bmatrix} \epsilon_{r,xx} & \epsilon_{r,xy} & 0 \\ \epsilon_{r,yx} & \epsilon_{r,yy} & 0 \\ 0 & 0 & \epsilon_{r,zz} \end{bmatrix}$	$\begin{bmatrix} \epsilon_{r,xx} & \epsilon_{r,xy} & \epsilon_{r,xz} \\ \epsilon_{r,yx} & \epsilon_{r,yy} & \epsilon_{r,yz} \\ \epsilon_{r,zx} & \epsilon_{r,zy} & \epsilon_{r,zz} \end{bmatrix}$
Isotropic	Diagonally Anisotropic	Transversely Anisotropic	Arbitrarily Anisotropic

Each tensor form has different complexity in the numerical problem to be computed, and apparently, the complexity rises as we proceed from tensor form **a** to tensor form **d**. Tensor forms **a-c** have global matrices of the same size but different numbers of non-zero values. Tensor form **d**, on the other hand, results in a global matrix that is four times as large. We recall that for tensor form **a** with small variations in permittivity, scalar-field formulation is valid and reduces the global matrix to one-quarter the size. **Table 4-2** gives the sizes of the eigenvalue problem and the global matrix for each tensor form. **Table 4-3** gives the sparsity of the global matrix and its size for tensor forms **a-c**, after [Fallahkhair et al., 2008](#).

The FDFD scheme by [Zhu and Brown, 2002](#) allows the introduction of diagonal anisotropies (tensor form **b**). Relative error less than  $10^{-5}$  on fundamental  $n_{eff}$  was reported when tested with a step-index fiber with high index contrast. The analytic value was used as the reference. Although the work of [Fallahkhair et al., 2008](#) extends to transverse anisotropies (tensor form **c**), the formulation is somehow complicated. It also uses normal grids and thus supposedly more computationally expensive. [Chen et al., 2009](#) extended the work to arbitrary anisotropies, with a similar formulation from that of [Zhu and Brown, 2002](#), where Yee mesh is also introduced to reduce computational effort. However, the size of the corresponding eigenvalue problem is quadrupled and thus computationally demanding.

**Table 4-2: Complexity of FDFD eigenvalue problem and size of FDFD global matrix with respect to permittivity tensor form**

Tensor Form	Eigenvalue Problem	Size of Global Matrix (Full Matrix)
<b>a</b> ( $\Delta\epsilon$ small)	$S\{E   H\} = \beta^2\{E   H\}$	$S = (M * N)^2$
<b>a</b> <b>b</b> <b>c</b>	$P \begin{bmatrix} E_x \\ E_y \end{bmatrix} = \begin{bmatrix} P_{xx} & P_{xy} \\ P_{yx} & P_{yy} \end{bmatrix} \begin{bmatrix} E_x \\ E_y \end{bmatrix} = \beta^2 \begin{bmatrix} E_x \\ E_y \end{bmatrix}$ $Q \begin{bmatrix} H_x \\ H_y \end{bmatrix} = \begin{bmatrix} Q_{xx} & Q_{xy} \\ Q_{yx} & Q_{yy} \end{bmatrix} \begin{bmatrix} H_x \\ H_y \end{bmatrix} = \beta^2 \begin{bmatrix} H_x \\ H_y \end{bmatrix}$	$P, Q = (M * N * 2)^2$
<b>d</b>	$R \begin{bmatrix} E_x \\ E_y \\ H_x \\ H_y \end{bmatrix} = \begin{bmatrix} A_{11} & A_{12} & A_{13} & A_{14} \\ A_{21} & A_{22} & A_{23} & A_{24} \\ A_{31} & A_{32} & A_{33} & A_{34} \\ A_{41} & A_{42} & A_{43} & A_{44} \end{bmatrix} \begin{bmatrix} E_x \\ E_y \\ H_x \\ H_y \end{bmatrix} = \beta \begin{bmatrix} E_x \\ E_y \\ H_x \\ H_y \end{bmatrix}$	$R = (M * N * 4)^2$

**Table 4-3: Sparsity of FDFD global matrix with respect to permittivity tensor form**

<b>a</b>	<b>b</b>	<b>c</b>
Isotropic	Diagonally Anisotropic	Transversely Anisotropic
$M * N * 2 * 5$	$M * N * 2 * 9$	$M * N * 2 * 16$

The black squares represent non-zero values, and therefore have to be stored in the sparse matrix. The fewer the black squares, the higher the matrix sparsity is and hence the less demanding the memory requirement is. After [Fallahkhair et al., 2008](#).

Since the thesis targets in analyzing general fiber geometries, one might think it is straightforward to consider tensor form  $\mathbf{d}$  with arbitrary permittivity tensor. However, although optical fibers are of the size of a few tens of microns to few hundreds of microns and therefore are small from the common perception, they are in fact large in size for numerical simulations. The full anisotropy scheme, tensor form  $\mathbf{d}$ , having a global matrix four times bigger than the other tensor forms  $\mathbf{a}$ - $\mathbf{c}$ , limits its usefulness when the computational environment is limited.

The FDFD formulation by [Zhu and Brown, 2002](#) is simple and its computation less demanding. We therefore follow such scheme and will show that by adding cross terms, it can be extended to include transverse anisotropies.

We come back to the formulation of our vector-field FDFD. We consider media with transverse material anisotropy and the corresponding permittivity tensor form  $\mathbf{c}$ ,

$$\mathbf{D} = \begin{bmatrix} D_x \\ D_y \\ D_z \end{bmatrix} = \epsilon_0 \epsilon_r \mathbf{E} = \epsilon_0 \begin{bmatrix} \epsilon_{r,xx} & \epsilon_{r,xy} & 0 \\ \epsilon_{r,yx} & \epsilon_{r,yy} & 0 \\ 0 & 0 & \epsilon_{r,zz} \end{bmatrix} \begin{bmatrix} E_x \\ E_y \\ E_z \end{bmatrix}. \quad (4.15)$$

Equations (4.11-12), together with equation (4.15), can then be written in matrix forms as

$$ik_0 \begin{bmatrix} H_x \\ H_y \\ H_z \end{bmatrix} = \begin{bmatrix} 0 & -i\beta I & U_y \\ i\beta I & 0 & -U_x \\ -U_y & U_x & 0 \end{bmatrix} \begin{bmatrix} E_x \\ E_y \\ E_z \end{bmatrix} \quad (4.16)$$

and

$$-ik_0 \begin{bmatrix} \epsilon_{r,xx} & \epsilon_{r,xy} & 0 \\ \epsilon_{r,yx} & \epsilon_{r,yy} & 0 \\ 0 & 0 & \epsilon_{r,zz} \end{bmatrix} \begin{bmatrix} E_x \\ E_y \\ E_z \end{bmatrix} = \begin{bmatrix} 0 & -i\beta I & V_y \\ i\beta I & 0 & -V_x \\ -V_y & V_x & 0 \end{bmatrix} \begin{bmatrix} H_x \\ H_y \\ H_z \end{bmatrix}, \quad (4.17)$$

where

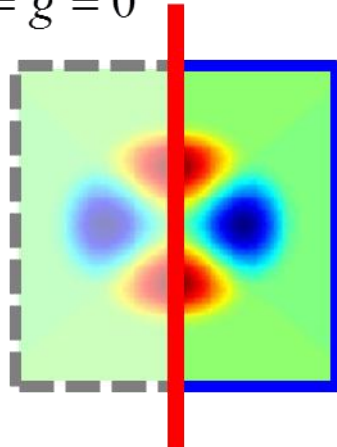
$$U_x = \frac{1}{\Delta x} \begin{bmatrix} -1 & 1 & & & \\ & -1 & 1 & & \\ & & \ddots & \ddots & \\ & & \ddots & \ddots & \\ & & & -1 & 1 \\ & & & & -1 \end{bmatrix}, \quad U_y = \frac{1}{\Delta y} \begin{bmatrix} -1 & & 1 & & \\ & -1 & & & \bullet \\ & & \ddots & \ddots & \\ & & \ddots & \ddots & 1 \\ & & & -1 & \\ & & & & -1 \end{bmatrix} \quad (4.18)$$

$$V_x = \frac{1}{\Delta x} \begin{bmatrix} 1 & & & & \\ -1 & 1 & & & \\ & -1 & \bullet & & \\ & & \bullet & \bullet & \\ & & & 1 & \\ & & & & -1 & 1 \end{bmatrix}, \quad V_y = \frac{1}{\Delta y} \begin{bmatrix} 1 & & & & \\ & 1 & & & \\ & & \bullet & & \\ & & & \bullet & \\ & & & & 1 \\ & & & & -1 & 1 \end{bmatrix} \quad (4.19)$$

are the finite-difference (FD) matrices subjected to how the two-dimensional fields are arranged into one-dimensional vectors for matrix computation. In our formulation the field-to-vector assignment is the same as shown in **Figure 4-2**. The FD matrices also depend on the boundary conditions specified. **Figure 4-4** illustrates two common types of boundary conditions, which are the Dirichlet and the Neumann boundary conditions. Values are designated on the Dirichlet boundaries, while derivatives are designated on the Neumann boundaries. We note that for FD matrices  $U_x$  and  $V_x$  in equations (4.18-19), there exist zeros in the off-diagonal values which represent the boundaries in x-direction, similar to the red shades in **Figure 4-2**. Exemplary FD matrices subjected to different boundary conditions are given in **Table 4-4**.

## Zero-Derivative (Neuman)

$$\left. \frac{\partial u}{\partial n} \right|_{\Gamma_2} = g = 0$$



## Zero-Value (Dirichlet)

$$u \Big|_{\Gamma_1} = u_0 = 0$$

**Figure 4-4: Schematic of Dirichlet and Neumann boundary conditions**

For both types we use only zero values in our formulations, i.e. the zero-value (the blue boundaries) and the zero-derivative (the red boundary) boundary conditions. For the exemplary symmetric field pattern (mode) shown here, it is possible to use only half of the domain to simulate the whole structure, where the zero-derivative boundary acts as the axis of symmetry.

**Table 4-4: Exemplary 1<sup>st</sup>-order finite-difference matrices for different boundary conditions**

FD	Zero-Value Dirichlet Boundary Conditions		Zero-Derivative Neumann Boundary Condition																																																											
	M+	2xM+	M+	(N-1)xM+																																																										
$U_x$	<table border="1"> <tr><td>1</td><td>2</td><td>3</td><td>4</td><td>-M</td><td>M+</td><td>2xM+</td><td>=</td><td>(N-1)xM+</td><td>NM</td></tr> <tr><td>Y</td><td>1</td><td>1</td><td>1</td><td>-1</td><td>1</td><td>2</td><td>2</td><td>2</td><td>-2</td></tr> <tr><td>X</td><td>1</td><td>2</td><td>3</td><td>4</td><td>-M</td><td>1</td><td>2</td><td>3</td><td>-M</td></tr> </table>	1	2	3	4	-M	M+	2xM+	=	(N-1)xM+	NM	Y	1	1	1	-1	1	2	2	2	-2	X	1	2	3	4	-M	1	2	3	-M	<table border="1"> <tr><td>1</td><td>2</td><td>3</td><td>4</td><td>-M</td><td>M+</td><td>2xM+</td><td>=</td><td>(N-1)xM+</td><td>NM</td></tr> <tr><td>Y</td><td>1</td><td>1</td><td>1</td><td>1</td><td>-1</td><td>1</td><td>2</td><td>2</td><td>2</td></tr> <tr><td>X</td><td>1</td><td>2</td><td>3</td><td>4</td><td>-M</td><td>1</td><td>2</td><td>3</td><td>-M</td></tr> </table>	1	2	3	4	-M	M+	2xM+	=	(N-1)xM+	NM	Y	1	1	1	1	-1	1	2	2	2	X	1	2	3	4	-M	1	2	3	-M
1	2	3	4	-M	M+	2xM+	=	(N-1)xM+	NM																																																					
Y	1	1	1	-1	1	2	2	2	-2																																																					
X	1	2	3	4	-M	1	2	3	-M																																																					
1	2	3	4	-M	M+	2xM+	=	(N-1)xM+	NM																																																					
Y	1	1	1	1	-1	1	2	2	2																																																					
X	1	2	3	4	-M	1	2	3	-M																																																					
$V_y$	<table border="1"> <tr><td>1</td><td>2</td><td>3</td><td>4</td><td>-M</td><td>M+</td><td>2xM+</td><td>=</td><td>(N-1)xM+</td><td>NM</td></tr> <tr><td>Y</td><td>1</td><td>1</td><td>1</td><td>1</td><td>-1</td><td>2</td><td>2</td><td>2</td><td>-2</td></tr> <tr><td>X</td><td>1</td><td>2</td><td>3</td><td>4</td><td>-M</td><td>1</td><td>2</td><td>3</td><td>-M</td></tr> </table>	1	2	3	4	-M	M+	2xM+	=	(N-1)xM+	NM	Y	1	1	1	1	-1	2	2	2	-2	X	1	2	3	4	-M	1	2	3	-M	<table border="1"> <tr><td>1</td><td>2</td><td>3</td><td>4</td><td>-M</td><td>M+</td><td>2xM+</td><td>=</td><td>(N-1)xM+</td><td>NM</td></tr> <tr><td>Y</td><td>1</td><td>1</td><td>1</td><td>1</td><td>-1</td><td>2</td><td>3</td><td>3</td><td>-3</td></tr> <tr><td>X</td><td>1</td><td>2</td><td>3</td><td>4</td><td>-M</td><td>1</td><td>2</td><td>3</td><td>-M</td></tr> </table>	1	2	3	4	-M	M+	2xM+	=	(N-1)xM+	NM	Y	1	1	1	1	-1	2	3	3	-3	X	1	2	3	4	-M	1	2	3	-M
1	2	3	4	-M	M+	2xM+	=	(N-1)xM+	NM																																																					
Y	1	1	1	1	-1	2	2	2	-2																																																					
X	1	2	3	4	-M	1	2	3	-M																																																					
1	2	3	4	-M	M+	2xM+	=	(N-1)xM+	NM																																																					
Y	1	1	1	1	-1	2	3	3	-3																																																					
X	1	2	3	4	-M	1	2	3	-M																																																					

Equations (4.16-17) can be expanded into:

$$\begin{aligned} ik_0 H_x &= U_y E_z - i\beta E_y \\ ik_0 H_y &= i\beta E_x - U_x E_z \\ ik_0 H_z &= U_x E_y - U_y E_x \end{aligned} \tag{4.20}$$

and

$$\begin{aligned} -ik_0 \epsilon_{r,xx} E_x - ik_0 \epsilon_{r,xy} E_y &= V_y H_z - i\beta H_y \\ -ik_0 \epsilon_{r,yx} E_y - ik_0 \epsilon_{r,yy} E_y &= i\beta H_x - V_x H_z \\ -ik_0 \epsilon_{r,zz} E_z &= V_x H_y - V_y H_x. \end{aligned} \tag{4.21}$$

After some algebra replacing  $E_z$  and  $H_z$ , we obtain two eigenvalue equations with respect to the electric field and the magnetic field, respectively. For electric fields:

$$\mathbf{P} \begin{bmatrix} E_x \\ E_y \end{bmatrix} = \begin{bmatrix} P_{xx} & P_{xy} \\ P_{yx} & P_{yy} \end{bmatrix} \begin{bmatrix} E_x \\ E_y \end{bmatrix} = \beta^2 \begin{bmatrix} E_x \\ E_y \end{bmatrix}, \quad (4.22)$$

where  $\mathbf{P}$  is the global matrix, with the sub-matrices:

$$\begin{aligned} P_{xx} = & -\frac{1}{k_0^2} U_x \left( \frac{I}{\epsilon_{r,zz}} \right) V_y V_x U_y + \left[ k_0^2 I + U_x \left( \frac{I}{\epsilon_{r,zz}} \right) V_x \right] \left[ \epsilon_{r,xx} + \frac{1}{k_0^2} V_y U_y \right] \\ & + U_x \left( \frac{I}{\epsilon_{r,zz}} \right) V_y \epsilon_{r,yx} \end{aligned} \quad (4.23)$$

$$\begin{aligned} P_{yy} = & -\frac{1}{k_0^2} U_y \left( \frac{I}{\epsilon_{r,zz}} \right) V_x V_y U_x + \left[ k_0^2 I + U_x \left( \frac{I}{\epsilon_{r,zz}} \right) V_y \right] \left[ \epsilon_{r,yy} + \frac{1}{k_0^2} V_x U_x \right] \\ & + U_y \left( \frac{I}{\epsilon_{r,zz}} \right) V_x \epsilon_{r,xy} \end{aligned} \quad (4.24)$$

$$\begin{aligned} P_{xy} = & U_x \left( \frac{I}{\epsilon_{r,zz}} \right) V_y \left[ \epsilon_{r,yy} + \frac{1}{k_0^2} V_x U_x \right] - \frac{1}{k_0^2} \left[ k_0^2 I + U_x \left( \frac{I}{\epsilon_{r,zz}} \right) V_x \right] V_y U_x \\ & + k_0^2 \epsilon_{r,xy} + U_x \left( \frac{I}{\epsilon_{r,zz}} \right) V_x \epsilon_{r,xy} \end{aligned} \quad (4.25)$$

$$\begin{aligned} P_{yx} = & U_y \left( \frac{I}{\epsilon_{r,zz}} \right) V_x \left[ \epsilon_{r,xx} + \frac{1}{k_0^2} V_y U_y \right] - \frac{1}{k_0^2} \left[ k_0^2 I + U_y \left( \frac{I}{\epsilon_{r,zz}} \right) V_y \right] V_x U_y \\ & - \frac{1}{k_0^2} \epsilon_{r,yx} + U_y \left( \frac{I}{\epsilon_{r,zz}} \right) V_y \epsilon_{r,yx}. \end{aligned} \quad (4.26)$$

When  $\epsilon_{r,xy} = \epsilon_{r,yx} = \mathbf{0}$ , the sub-matrices reduce to those in [Zhu and Brown, 2002](#). Similarly, for magnetic fields:

$$\mathbf{Q} \begin{bmatrix} H_x \\ H_y \end{bmatrix} = \begin{bmatrix} Q_{xx} & Q_{xy} \\ Q_{yx} & Q_{yy} \end{bmatrix} \begin{bmatrix} H_x \\ H_y \end{bmatrix} = \beta^2 \begin{bmatrix} H_x \\ H_y \end{bmatrix} \quad (4.27)$$

where  $\mathbf{Q}$  is the global matrix, with the sub-matrices:

$$\begin{aligned} Q_{xx} = & -\frac{1}{k_0^2} U_x \left( \frac{I}{\epsilon_{r,zz}} \right) V_y V_x U_y + \left[ k_0^2 I + U_x \left( \frac{I}{\epsilon_{r,zz}} \right) V_x \right] \left[ \epsilon_{r,xx} + \frac{1}{k_0^2} V_y U_y \right] \\ & + U_x \left( \frac{I}{\epsilon_{r,zz}} \right) V_y \epsilon_{r,yx} \end{aligned} \quad (4.28)$$

$$\begin{aligned} Q_{xy} = & -\frac{1}{k_0^2} U_x \left( \frac{I}{\epsilon_{r,zz}} \right) V_y V_x U_y + \left[ k_0^2 I + U_x \left( \frac{I}{\epsilon_{r,zz}} \right) V_x \right] \left[ \epsilon_{r,xx} + \frac{1}{k_0^2} V_y U_y \right] \\ & + U_x \left( \frac{I}{\epsilon_{r,zz}} \right) V_y \epsilon_{r,yx} \end{aligned} \quad (4.29)$$

$$\begin{aligned} Q_{yx} = & -\frac{1}{k_0^2} U_x \left( \frac{I}{\epsilon_{r,zz}} \right) V_y V_x U_y + \left[ k_0^2 I + U_x \left( \frac{I}{\epsilon_{r,zz}} \right) V_x \right] \left[ \epsilon_{r,xx} + \frac{1}{k_0^2} V_y U_y \right] \\ & + U_x \left( \frac{I}{\epsilon_{r,zz}} \right) V_y \epsilon_{r,yx} \end{aligned} \quad (4.30)$$

$$\begin{aligned} Q_{yy} = & -\frac{1}{k_0^2} U_x \left( \frac{I}{\epsilon_{r,zz}} \right) V_y V_x U_y + \left[ k_0^2 I + U_x \left( \frac{I}{\epsilon_{r,zz}} \right) V_x \right] \left[ \epsilon_{r,xx} + \frac{1}{k_0^2} V_y U_y \right] \\ & + U_x \left( \frac{I}{\epsilon_{r,zz}} \right) V_y \epsilon_{r,yx} \end{aligned} \quad (4.31)$$

Now that we have obtained the eigenvalue problems in our vector-field FDFD, we solve the eigen problem by using an available eigensolver and obtain the fields ***Ex***, ***Ey*** and ***Hx***, ***Hy***. The corresponding fields ***Hz*** and ***Ez*** can then be calculated with equations (4.20-21). As previously discussed, sparse matrices are introduced to decrease the amount of memory required. We use **MATLAB** as our simulation environment. **MATLAB** readily includes the Arnoldi Package (**ARPACK**) as the function **eigs**. More details on the algebra in arriving at the global equations (4.22-31) can be found in **Appendix E**.

#### 4.4 Some Techniques Regarding Improvement of FDFD

To further improve the performance of FDFD, some techniques have been proposed. For example, Yee's staggered mesh has been already incorporated in our FDFD to reduce the amount of grid points needed while maintaining the accuracy. If we use a normal mesh, we only have to change the FD matrices ***Ux***, ***Uy***, ***Vx*** and ***Vy*** in equations (4.18-19).

Index-averaging ([Zhu and Brown, 2002](#)) is another simple but useful technique, especially when the resolution for spatial discretization is low. It is particularly important when the computational power limits the number of grid points of the simulation. Correspondingly, the larger the fiber geometry, the more sparse the grid points. The idea of index-averaging is to make use of more values (i.e., grayscale over binary) near the boundaries with changes in refractive index. It has been shown that index-averaging increases greatly the convergence of numerical calculations. In our simulation, index-averaging is implemented

through interpolation. As an example, on the bottom-left of **Figure 4-5**, the refractive index of the point in red is given by  $\epsilon_{\text{average}} = \eta * \epsilon_a + (1 - \eta) * \epsilon_b$ , where  $\eta$  is the ratio of the region with refractive index  $\epsilon_a$  to the area enclosed with dashed red square. In our simulations, this is approximated by the interpolation of sub-grid points to the Yee mesh, the assignment of their values according to the original fiber geometry, and the calculation of their average. The accuracy of such approximation depends on the interpolation factor  $\Gamma$ , which is a positive even integer that specifies how many additional sub-grid points are used. For example, when  $\Gamma = 10 (N), 9 (N-1)$  additional points are assigned in between the original grid points, the refractive index profile of the area with **11-by-11 (2N+1)-by-(2N+1)** points centered around the original grid point is averaged and assigned to the grid point.

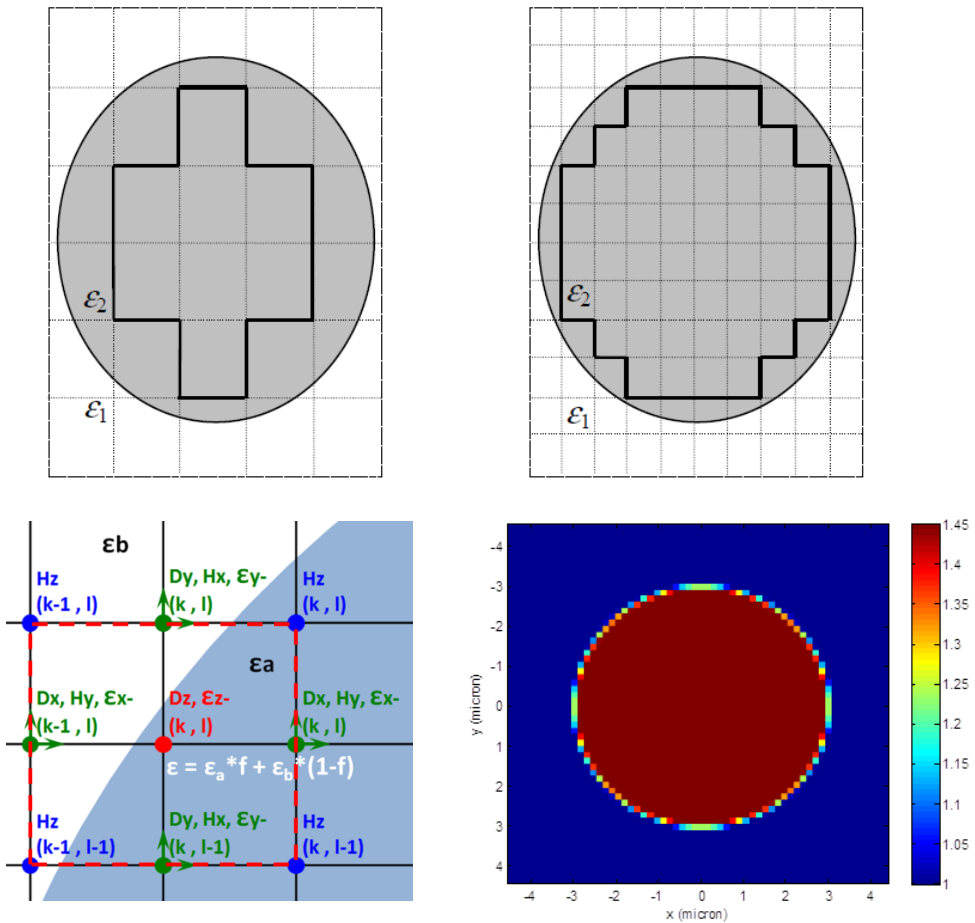


**Figure 4-5: Schematic of staircase approximation for curved interface and index-averaging**

*Top: staircase approximation of curved interface: only two levels of values are used and the approximation depends on the resolution of grids. Bottom-left: The area enclosed by the dashed red line is considered for index-averaging. With index-averaging, thanks to the use of more levels of values, even with low resolution, the curved surface is well represented in simulations, as shown on the bottom-right.*

Other advanced techniques deal with the boundary conditions. Other than conventional Dirichlet, Neumann and mixed boundary conditions, for example, the perfectly matched layer (PML) has been proposed ([Berenger, 1994](#)) and widely used.

Without additional treatment at the boundaries, our FDFD formulation falls in the Dirichlet boundary condition with zero-values. Additionally, by setting zero-derivatives at the boundaries, we can use the Neumann boundary condition to reduce the calculation window according to geometrical symmetry. This is particularly advantageous when calculating the fundamental space-filling mode (FSM) of PC claddings.

## 4.5 Spurious Modes and Their Elimination

During our preliminary tests on the vector field formulation, we found that for PBG-guiding geometries, very often spurious results ruin the whole simulations as only limited sets of eigenvalues and eigenvectors are calculated. This is mainly due to the various combinations of hole-guiding modes that result in various eigenvalues, and the space close to the edges of the calculation window. In order to remove these spurious modes, we propose the following two first techniques and also discuss other two possibilities.

### 4.5.1 Post-Computation Correlation

One straightforward method in removing the spurious results is to do it manually after obtaining the results. This can also be facilitated automatically by performing correlation between the obtained eigenfields and the presumed modal fields. However, no matter how this post-computation selection is performed, it requires more eigenvalues to be calculated in order to contain desired results other than the excessive spurious results. Moreover, it requires additional time for either computational or manual selection. We therefore do not consider this a good solution for the problem of spurious modes.

### 4.5.2 Pre-Computation Edge-Cutting

As previously stated, one main type of spurious fields localizes near the boundaries. By replacing these spaces with unity refractive index, we can remove this type of spurious

results. The advantage of this method is that it requires only little pre-treatment in setting up the refractive index geometry. The problem with this method is that the simulation might not seem physical, especially when only part of the fiber geometry is included in the simulation. The schematic for edge-cutting is shown in **Figure 4-6**.

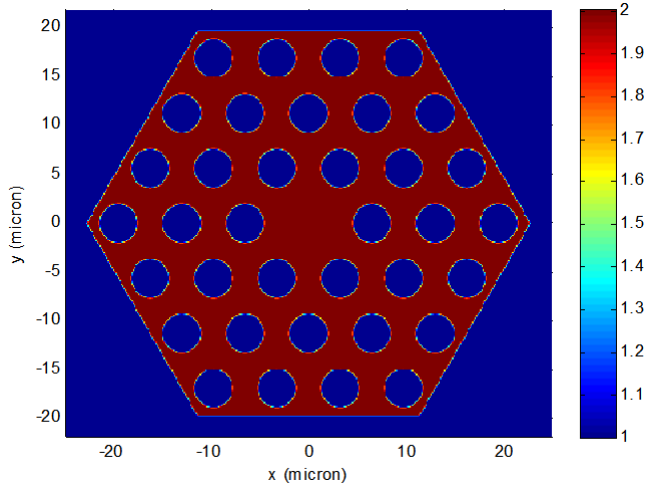


**Figure 4-6: Permittivity profile of a three-ring PCF with edge-cutting**

*In this case, the silica outside the photonic crystal cladding is replaced by air. Since the field of the fundamental guiding mode does not extend outside the photonic crystal cladding, the geometry with edge-cutting can be still be regarded physical.*

#### 4.5.3 In-Computation Eigen Solver Specifications

One additional method is to specify the eigenvalues to be located during the eigen solving process. The [MATLAB](#) sparse matrix eigen solver, [eigs](#), seeks eigenvalues with the largest/smallest/closest magnitudes/algebraic values/real parts/imaginary parts. For index-guiding fiber geometries, looking for eigenvalues with the largest algebraic values/magnitude/real parts gives good results. However, for PBG- guiding fiber geometries, the largest eigenvalues are often those of the hole-guiding modes because of the higher refractive index of the infiltrating material. Therefore, we have to seek eigenvalues that are close to and smaller than the refractive index of the PCF host material, which is silica in most cases. Unfortunately, [eigs](#) does not allow the specification to look for only smaller values and therefore introduce spurious results with larger eigenvalues.

#### 4.5.4 Divergence Maxwell Equations

By taking into account the divergence Maxwell equations, it may be possible to avoid some spurious results, as more physical constraints are imposed. From this point of view, the vector-field FDFD scheme proposed by Fallahkhair et al., 2008 may be a better choice. However, careful studies and comparisons shall be made to come to a solid conclusion.

### 4.6 Implementation of the Scalar-Field FDFD and the Vector-Field FDFD

Both the scalar-field FDFD and the vector-field FDFD are integrated into a single code library written in MATLAB and can be found in **Appendix A**. A simulation console m-file is written to incorporate the various function m-files to perform the simulations. A general computational flow is as follows:

- 1) Input parameters for the fiber and the simulation are assigned in the console m-file.
- 2) The *geometry\_* m-files generate the fiber geometry according to specification and the factor of index-averaging.
- 3) If index-averaging is desired, the *index\_avg* m-file processes the geometry according to mesh configuration.
- 4) The next step is to formulate the eigenvalue problem. The *sFDFD* m-file is for scalar-field FDFD, the *vFDFDd* m-files are for vector-field FDFD with diagonal anisotropies, and the *vFDFDt* m-files are for vector-field FDFD with transverse anisotropies.
- 5) The computation proceeds to the eigen solving process. The *eigsolve* m-file uses the *eigs* function in MATLAB, which seeks a defined number of eigenvalues and eigenvectors of a specific matrix using ARPACK (Arnoldi Package), and recasts the eigenvectors into eigenfields according to the dimension of the eigenvalue problem.
- 6) With some additional m-files, the results are arranged, displayed, and saved at the end of the console m-file.

### 4.7 Verification and Benchmarking of Proposed Schemes

#### 4.7.1 Methods for Verification

“Are the results correct, or at least relevant?” After the implementation of the numerical

schemes, the next problem comes into mind is whether they give good results. We use the following three methods to verify our FDFD schemes:

- 1) Theoretical verification,
- 2) Numerical verification, and
- 3) Experimental verification.

### **1) Theoretical Verification**

The first method is to compare the numerical results with good references, which are often analytic results. The idea is to use simple fiber geometries with known analytic results to verify the numerical schemes, and then extend the use of the validated numerical schemes to more complicated structures where analytic analysis becomes extremely difficult -- if not impossible -- because of the problem complexity.

Modal analysis of step-index fiber geometries, particularly those with small index-contrast, can be performed analytically. For more complicated photonic crystal fibers, although the analytic expressions are unsolvable, through basis-function expansion approach, one can obtain accurate results provided that the photonic crystal structure is not too complicated. Sometimes the basis-function expansion approach is regarded semi-analytic and it is useful for fiber geometries with periodic structures. Nevertheless, when there exist non-circular air holes, for example, the basis-function expansion approach is not applicable. Accordingly, it cannot accurately characterize real fiber geometries that are manufactured with defects.

### **2) Numerical Verification**

The next method is numerical verification. As the name suggests, this method lies entirely in the simulations themselves. The idea is to perform auto-verification of the numerical methods themselves. With this method, not only the numerical schemes (theory, formulation) themselves are accounted, but also the simulation conditions. The most important results of this verification method are the convergence curves. They may be as functions of either the step size or the size of the calculation window. Fast and steady convergence is expected for a good simulation scheme, as it represents smaller uncertainty of the simulation. On the other hand, although the uncertainty may be minimized, we still have no information regarding the error. Similarly, good convergence against the size of the calculation window may suggest that our simulation results are intrinsic, but does not give any information on whether the intrinsic results are correct.

### **3) Experimental Verification**

The third method is experimental verification. Intuitively, it appears to be the most convincing verification method as the ultimate goal of simulations is to predict what is

going to happen in experiments. Therefore, it is worthwhile to take into account the experimental verification. However, since the field of PLCFs is still new and awaits further studies, it is not easy to control the experimental conditions accurately. This has lots to do with the not-so-organized nature of LCs; they are not perfectly crystalline. The molecular arrangement of LC inside the host PCF greatly affects the characteristics of the PLCF, but with our current experimental means, it is not possible to observe the real configuration of LC inside the fiber. As the first approximation, a quasi-planar configuration is often assumed for nematic liquid crystals in a PCF without any pre-treatment. This will be further discussed in **Section 5.3**. Consequently, we may use experimental results for qualitative verification rather than strict quantitative comparison.

In order to raise the confidence level of our simulations, we test our FDFD schemes with various fiber geometries according to the first two verification methods described above. A brief introduction on the test fiber geometries is as follows, and will be discussed in details respectively in the following sections.

We test the performances of our numerical tools with the following geometries:

- 1) Single-Mode Fiber (SMF)

We first consider a standard single-mode telecommunication fiber (SMF). The diameter of a SMF is smaller, and its minimum radius of curvature in structure larger, than a typical PCF. As a result, the simulation condition is expected to be less stringent. The long wavelength also reduces computational effort. Furthermore, as discussed in **Chapter 3**, when the index-contrast is low, the LP approximation gives good results and therefore can be used for comparison.

- 2) Multi-Mode Fiber (MMF)

In a multi-mode fiber, the field patterns of higher-order modes have more rapid changes (higher spatial frequency) and are therefore fast-varying with respect to the dimension of the fiber structure. The higher-order modes also have larger spatial extent and therefore require larger calculation windows. The MMF is expected to pose more stringent conditions on the simulations, and is useful in examining the performance of the FDFD schemes.

- 3) Step-Index Fiber With High Index-Contrast (HC-SIF)

When the index-contrast is high, the scalar approximation is no longer valid. With an HC-SIF, we show the discrepancy between the scalar field and the vector field formulations. This fiber geometry, along with the next one, which is the holey fiber, are discussed in [Zhu and Brown, 2002](#). Since our vector-field FDFD is based on their work, by replicating the results, we can also know whether we are on the right track with the numerical schemes.

#### 4) Photonic Crystal Fiber (Holey Fiber, HoF)

Last, a photonic crystal fiber is considered. The HoF has the same type of geometry as the host PCF of our PLCF of interest.

#### 4.7.2 Single-Mode Fiber (SMF)

Some excerpt from the specification of Corning<sup>®</sup> SMF-28™ telecommunication fiber (**Appendix B**) is shown in **Table 4-5**.

**Table 4-5: Excerpted parameters of Corning<sup>®</sup> SMF-28™ Optical Fiber**

Core Diameter	8.2μm
Refractive Index Difference	0.36 %

By defining the refractive index difference as

$$\Delta n = \frac{n_{core} - n_{cladding}}{n_{cladding}} \times 100\% \quad (4.32)$$

and assuming the cladding to be made of fused silica, with refractive index specified by the common Sellmeier equation (**Appendix C**)

$$n^2 = 1 + \frac{B_1 \lambda^2}{\lambda^2 - C_1} + \frac{B_2 \lambda^2}{\lambda^2 - C_2} + \frac{B_3 \lambda^2}{\lambda^2 - C_3} \quad (4.33)$$

where the Sellmeier coefficients are shown in **Table 4-6**, we arrive at the SMF for benchmarking (**Table 4-7**).

**Table 4-6: Sellmeier coefficients for fused silica**

B <sub>1</sub>	B <sub>2</sub>	B <sub>3</sub>
6.96166300E-1	4.07942600E-1	8.97479400E-1
C <sub>1</sub> (μm <sup>2</sup> )	C <sub>2</sub> (μm <sup>2</sup> )	C <sub>3</sub> (μm <sup>2</sup> )
4.67914826E-3	1.35120631E-2	9.79340025E+1

**Table 4-7: The SMF for benchmarking**

Wavelength	1.55μm
Core Diameter	8.2μm
Core Refractive Index	1.449504
Cladding Refractive Index	1.444304
Δn	0.360035%
Normalized Frequency, V	2.038674

We first analyze the SMF analytically with the LP approximation. The solutions of equations (3.32-33) are obtained by solving the dispersion relation

$$u \frac{J_{l\pm 1}(u)}{J_l(u)} = \pm v \frac{K_{l\pm 1}(v)}{K_l(v)}, \quad (4.34)$$

where  $u$ ,  $v$  are the transverse propagation constants within the core ( $\alpha$ ) and the cladding ( $\kappa$ ), respectively, multiplied by the radius of the core ( $\rho$ ), i.e.,

$$u = \alpha \cdot \rho, \quad v = \kappa \cdot \rho, \quad (4.35)$$

where

$$\alpha^2 = k_0^2 n_{core}^2 - \beta_m^2, \quad \kappa^2 = \beta_m^2 - k_0^2 n_{cladding}^2. \quad (4.36)$$

$J$  and  $K$  are Bessel's functions of the first and the second kinds, respectively. Furthermore,  $u$  and  $v$  are related by the normalized frequency,  $V$ , as in equation (3.48):

$$u^2 + v^2 = V^2, \quad (4.37)$$

By introducing the  $b$ , the normalized propagation constant, to replace  $u$  and  $v$ ,

$$b = \frac{\beta^2 - k_0^2 n_{cladding}^2}{k_0^2 n_{core}^2 - k_0^2 n_{cladding}^2} = \left( \frac{v}{V} \right)^2, \quad 0 < b < 1 \quad (4.38)$$

the dispersion relation is recast as

$$D \equiv \sqrt{1-b} \frac{J_{l\pm 1}(V\sqrt{1-b})}{J_l(V\sqrt{1-b})} + \sqrt{b} \frac{K_{l\pm 1}(V\sqrt{b})}{K_l(V\sqrt{b})} = 0. \quad (4.39)$$

With sufficiently small step-size, we can obtain the values of  $b$  at which the dispersion relation (4.39) is satisfied, and that in turn gives us the effective refractive index ( $n_{eff}$ ) of the mode concerned. The dispersion curves with  $I = 0$  and  $I = 1$  are shown in **Figure 4-7**.

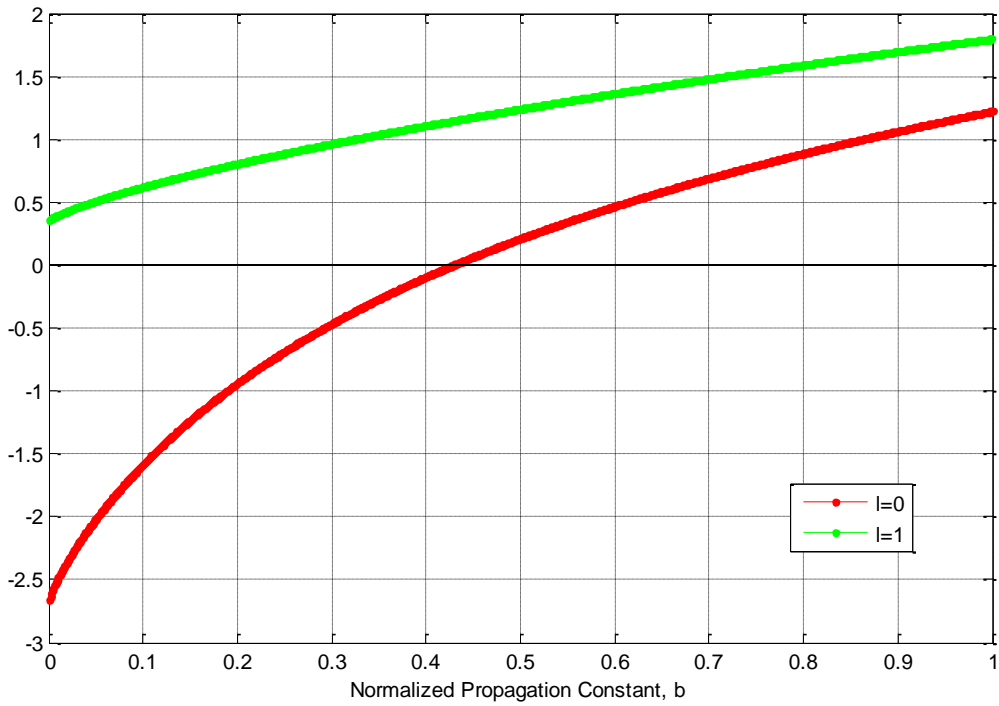


Figure 4-7: Dispersion relation curves of the SMF for  $I = 0$  and  $I = 1$

We can see that when  $I = 0$  there is one solution for  $D = 0$ , but when  $I = 1$  (or  $I > 1$ ),  $D$  is always greater than zero. This corresponds to single-mode operation of the optical fiber. The corresponding mode is  $LP_{01}$ , with  $n_{eff} = 1.446535$ . This value is calculated with **1E-8** step size in  $b$  and will be taken as the reference for our numerical simulations. We note that Marcuse's approximation formula (4.40) also gives a similar value, **1.446532**.

$$b(V) \approx \left( 1.1428 - \frac{0.996}{V} \right)^2 \quad (4.40)$$

We do not discuss the valid digits in Marcuse's approximation, but rather assume that the fourth digit is accountable.

Table 4-8: Common FDFD simulation parameters for the SMF

Calculation Window (Convergence against Step Size)	32μm
Step Size (Convergence against Window Size)	0.05μm
Index-Averaging Factor (If Applied)	10

The results of our FDFD simulations on the SMF are shown in **Figure 4-8**, **Figure 4-9** & **Figure 4-10**, and the common parameters of the simulations are given in **Table 4-8**. We perform convergence analysis with respect to the size of the calculation window and the grid step size.

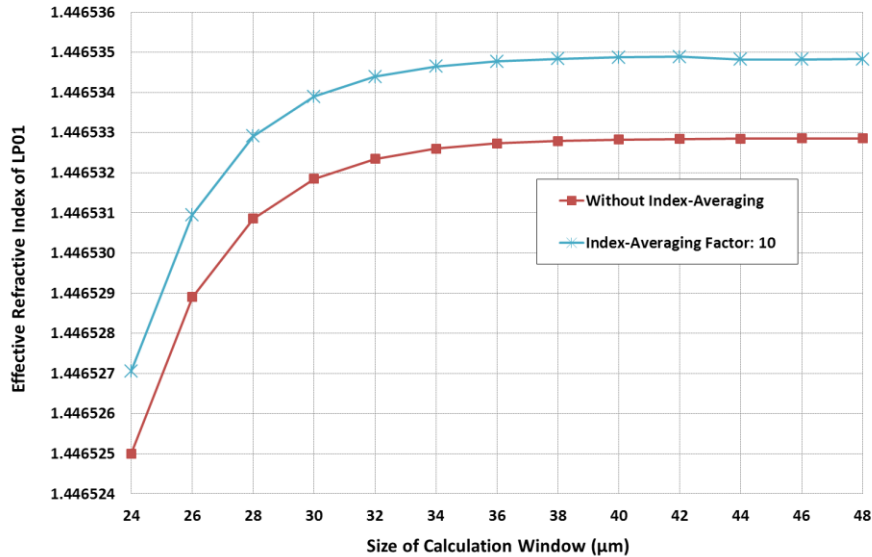


**Figure 4-8: Convergence curves of the SMF with respect to the size of calculation window calculated with scalar-field FDFD**

**Figure 4-8** shows that the convergence reaches **1E-6 (0.7ppm)** with calculation window larger than **32 $\mu\text{m}$** . We take this value to perform the convergence analysis with respect to the size of steps, without index-averaging (**Figure 4-9**) and with index-averaging (**Figure 4-10**), for both scalar-field and vector-field FDFDs.

With index-averaging, the convergence reaches the order of **1E-6 (Figure 4-10)** with number of grids more than **250**, while the value without index-averaging is almost **2E-5 (Figure 4-9)**. The index-averaging technique improves largely the convergence, especially when the resolution is low. At **250** grids, the resolution is **0.128 $\mu\text{m}$** , roughly **1/12** the wavelength ( $\lambda=1.55\mu\text{m}$ ). This criterion, together with the **1E-6 (3.5ppm)** convergence, will later be considered in our simulations. It should be noted that in most cases, owing to limited computational power, such criterions are not quite accessible.

By comparing the results with the analytic value (**LP01,  $n_{\text{eff}} = 1.446535$** ), we obtain the errors of our simulations, which is **1E-6 (0.7ppm)** for the scalar-field FDFD (**1.446534**), and **5E-6 (3.5ppm)** for the vector-field FDFD (**1.446530**). In brief, for the SMF, the analytical and numerical values match well to the fifth digit after the decimal point, which

corresponds to relative error smaller than **7ppm**.

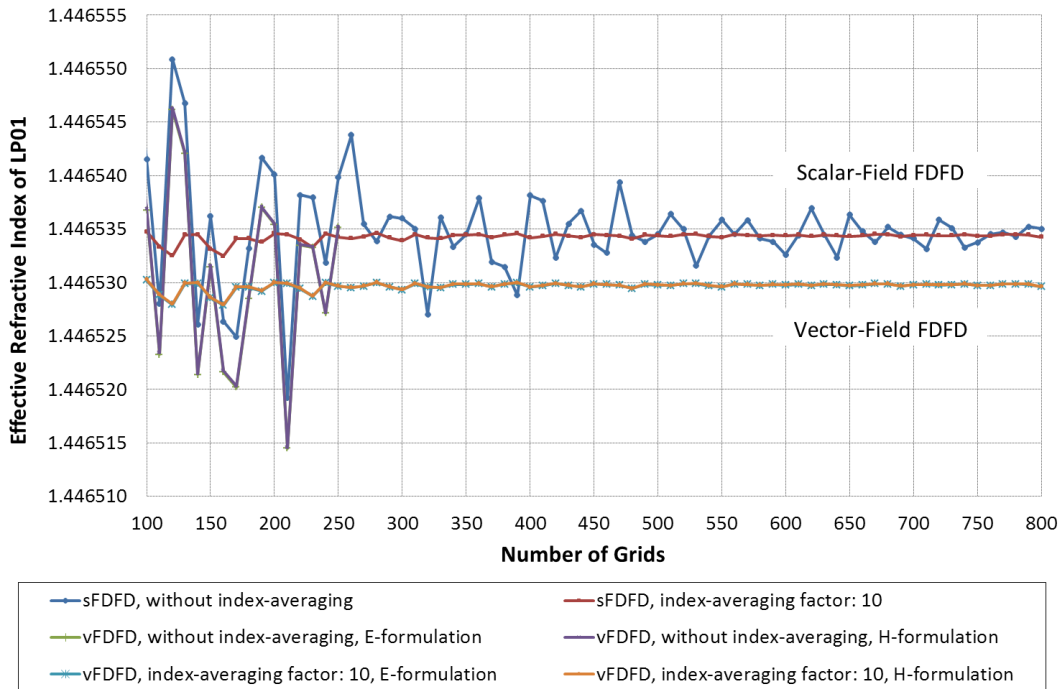


**Figure 4-9: Convergence curves of the SMF with respect to the number of grids**

We note that in our simulations the E-formulation and the H-formulation do not make a difference. In **Figure 4-10** the two curves almost overlap with each other. **Figure 4-11** shows the first sixteen eigenfields in our scalar-field simulation, and **Figure 4-12** shows the two sets of fields of the fundamental modes in our vector-field simulation.

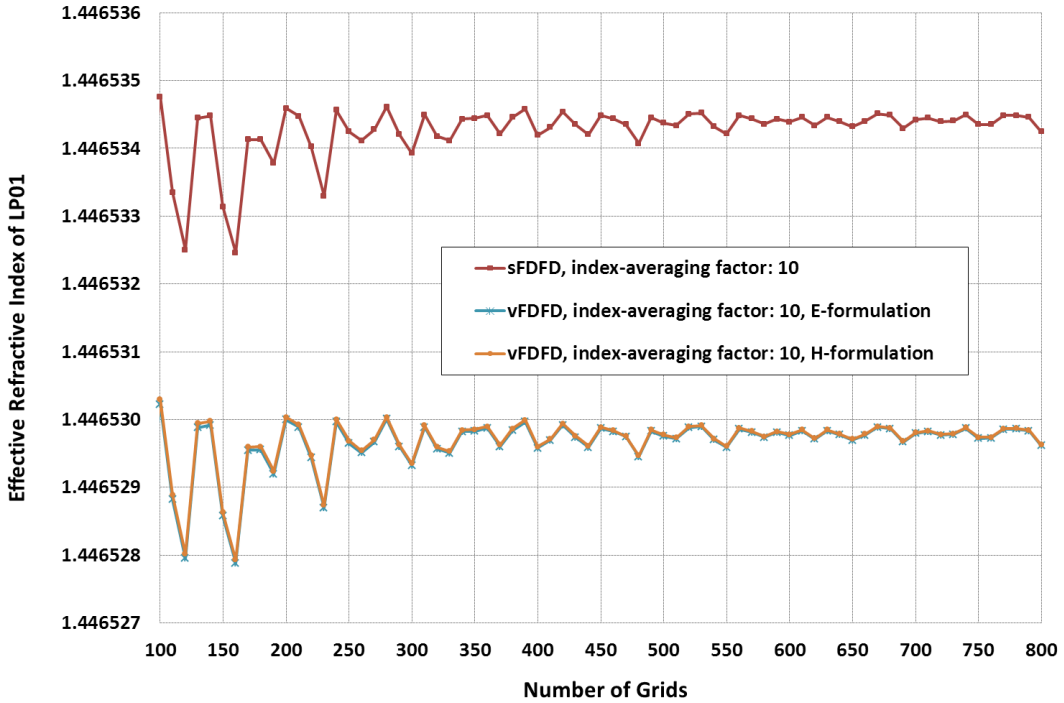


**Figure 4-10: Convergence curves of the SMF with respect to the number of grids with index-averaging factor 10**

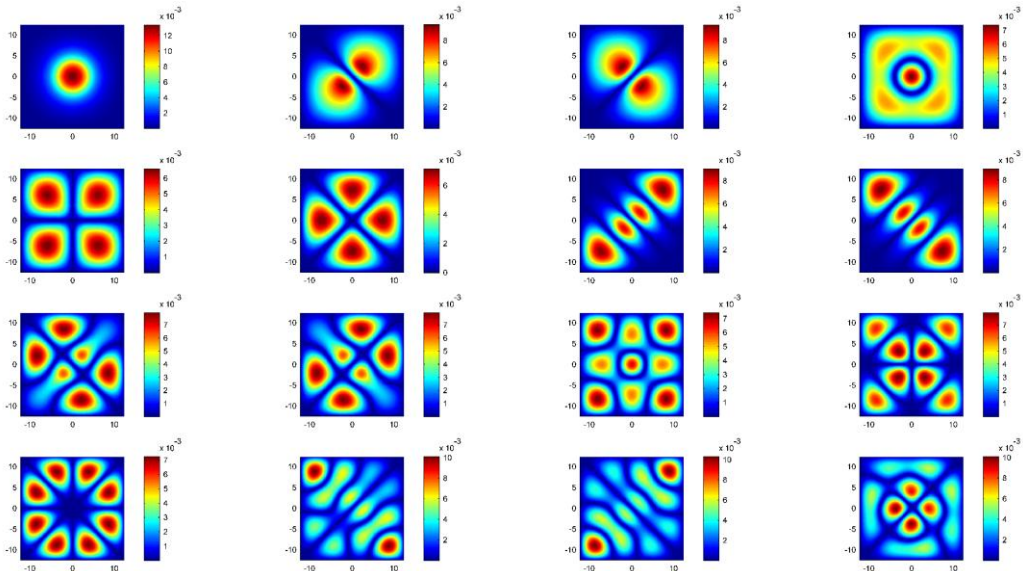


**Figure 4-11: Eigenfields (eigenvectors in matrix formulation) of the SMF with the largest 16 eigenvalues calculated with scalar-field FDFD**

We see that only one physical mode exists, which corresponds to the single-mode operation of the fiber. The spurious eigenfields possess mirror symmetry with respect to  $y=x$ . This is due to the discretization of the grids: each axis is discretized from  $-N/2$  to  $N/2-1$  with unity step size, where  $N$  is the number of grids.

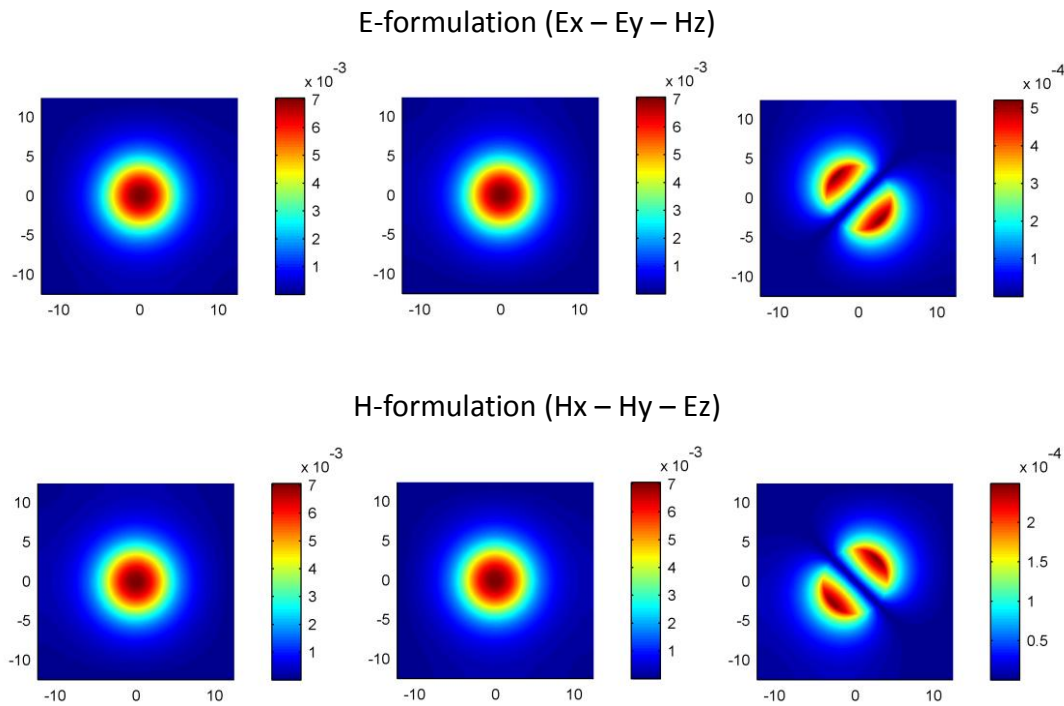


**Figure 4-12: Fundamental eigenfields of the SMF calculated with vector-field FDFD**

With vector-field FDFD, it is possible to obtain information regarding all six fields in two sets.

#### 4.7.3 Multi-Mode Fiber (MMF)

Unlike the small core size of a telecommunication SMF, a typical commercial MMF has core size around **50** to **62.5 $\mu\text{m}$**  and is thus larger in size than a SMF for numerical simulations. Excessive modes also make them impractical for comparison between analytical and numerical analyses. Consequently, a MMF with a smaller V-parameter is preferred for numerical tests and benchmarking. By increasing four times the core diameter of the SMF described in the previous section, we obtain the MMF for benchmarking with **V = 8.15** (**Table 4-9**).

**Table 4-9: The MMF for benchmarking**

Wavelength	1.55 $\mu\text{m}$
Core Diameter	32.8 $\mu\text{m}$
Core Refractive Index	1.449504
Cladding Refractive Index	1.444304
$\Delta n$	0.360035%
Normalized Frequency, V	8.154694

Similar to the benchmarking with the SMF, we first perform LP analysis of the MMF considered. The results are given in **Figure 4-13** and **Table 4-10**.

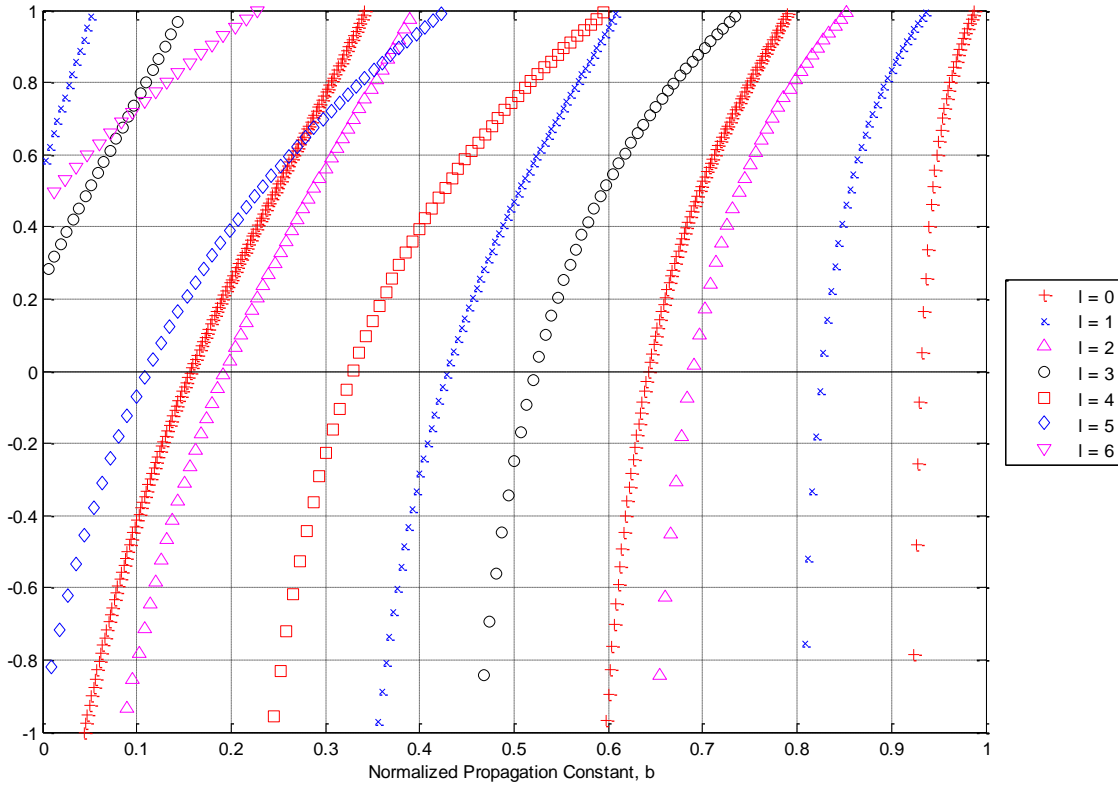


**Figure 4-13: Dispersion relation curves of the MMF from  $l = 0$  to  $l = 6$**

**Table 4-10:  $n_{eff}$  of  $LP_{lm}$  modes of the MMF**

$m \backslash l$	1	2	3
0	1.449147	1.447645	1.445121
1	1.448600	1.446538	-
2	1.447888	1.445312	-
3	1.447022	-	-
4	1.446016	-	-
5	1.444883	-	-
6	-	-	-

**Table 4-11: Scalar-field FDFD simulation parameters for the MMF**

Calculation Window (Convergence against Step Size)	50μm
Step Size (Convergence against Window Size)	0.1μm
Index-Averaging Factor (If Applied)	10

Next, we also use the scalar-field FDFD to study the convergence with respect to the calculation window. The result is shown **Figure 4-14**. As expected, for higher order modes, larger calculation windows are required because the extents of the fields are wider. More detailed convergence curves for the first five modes are shown in **Figure 4-15**. We take a moderate calculation window size of **50μm** for the convergence analysis with respect to the step size. In fact, other than the quantitative convergence curves, we can also estimate whether the results are intrinsic by observing the orientation of the  $I > 0$  modes. If the modal patterns rotate randomly in simulations, then we can say that the results are not affected by the rectangular calculation window. Otherwise the orientation always matches the symmetry condition of the simulation, which depends on the calculation window and the discretization scheme.

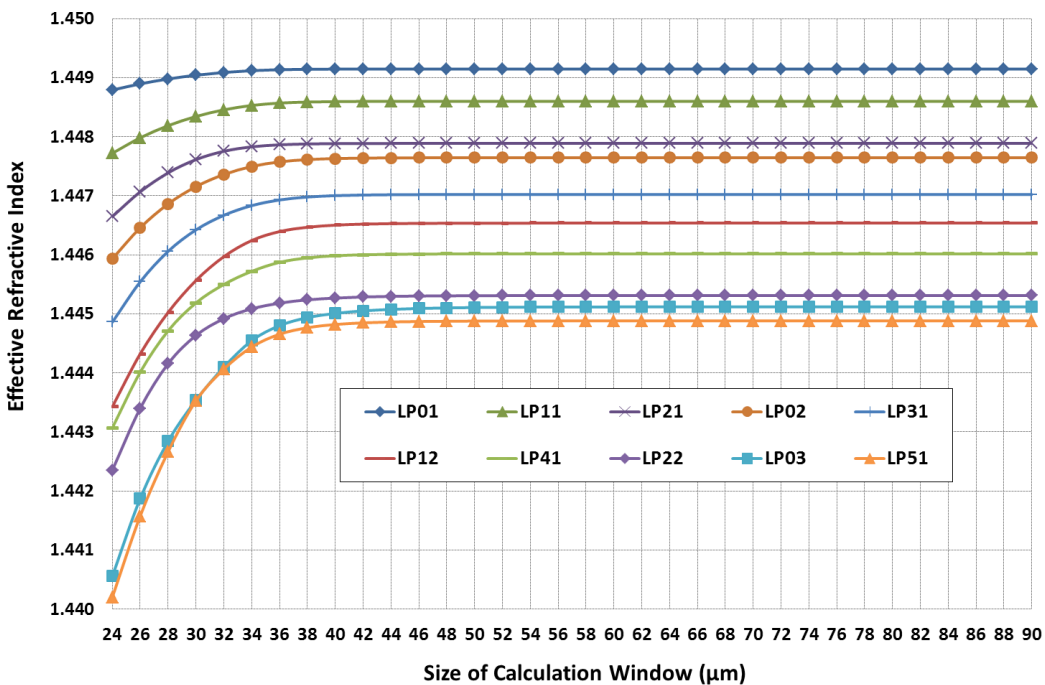


**Figure 4-14: Convergence curves of the MMF with respect to the size of calculation window calculated with scalar-field FDFD**

**Figure 4-16 & Figure 4-17** show the normalized convergence curves of the scalar-field FDFD, without and with index-averaging, respectively. Contrary to expected, the calculations for MMF converge faster than for SMF and reach **<1ppm** with a lower resolution at **200** grids for lower order modes (**Figure 4-17**). This infers that the requirements on simulations not only depend on the wavelength and the complexity of modal fields, but also the radius of curvature upon interfaces. We also note that the effectiveness of index-averaging is once again verified. In the following simulations, we will take index-averaging as a standard process.

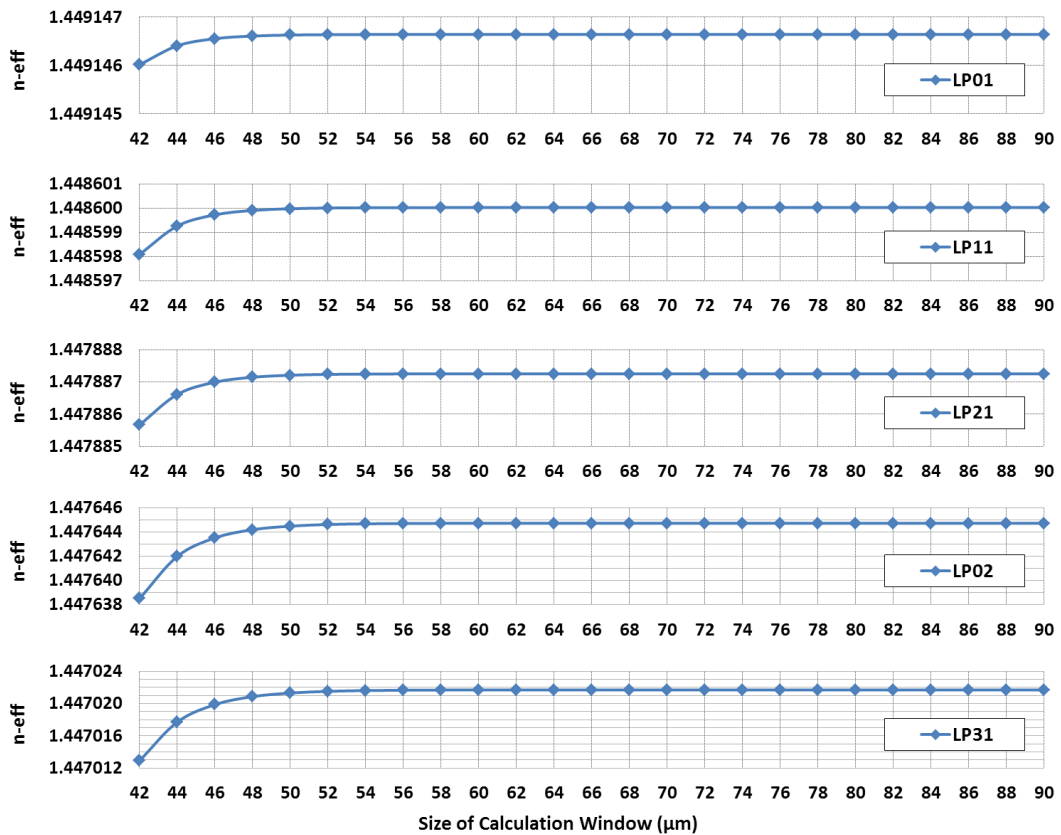


**Figure 4-15:** More detailed convergence curves with respect to the size of calculation window for the first five modes of the MMF calculated with scalar-field FDFD

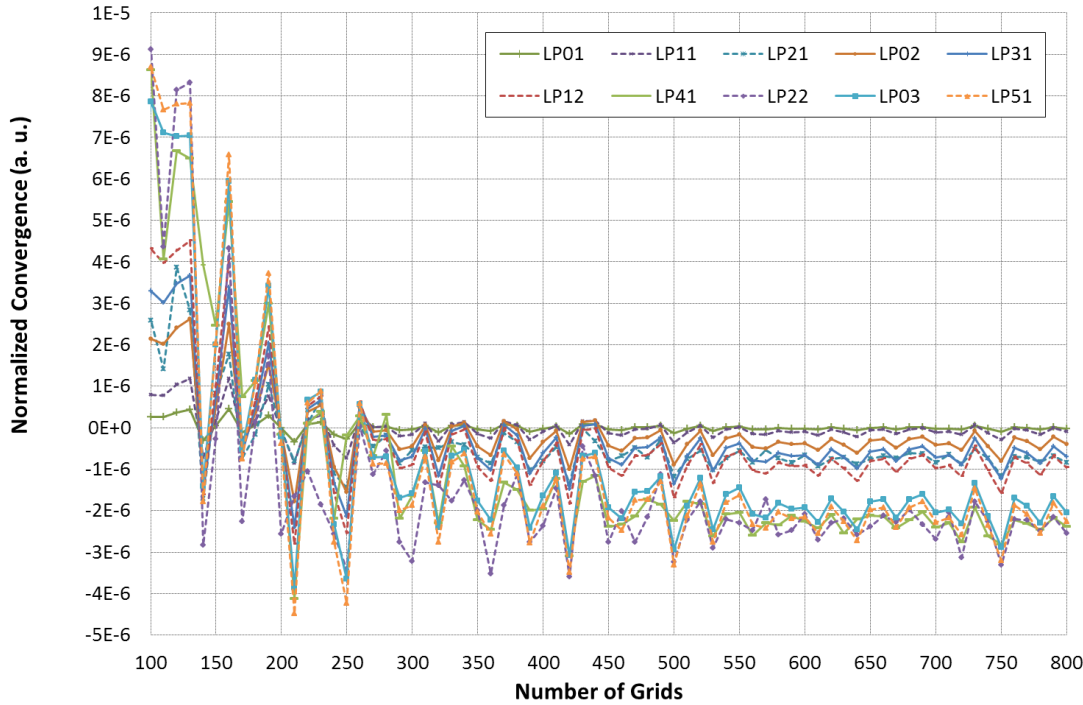


**Figure 4-16: Convergence curves of the MMF calculated with scalar-field FDFD and without index-averaging**

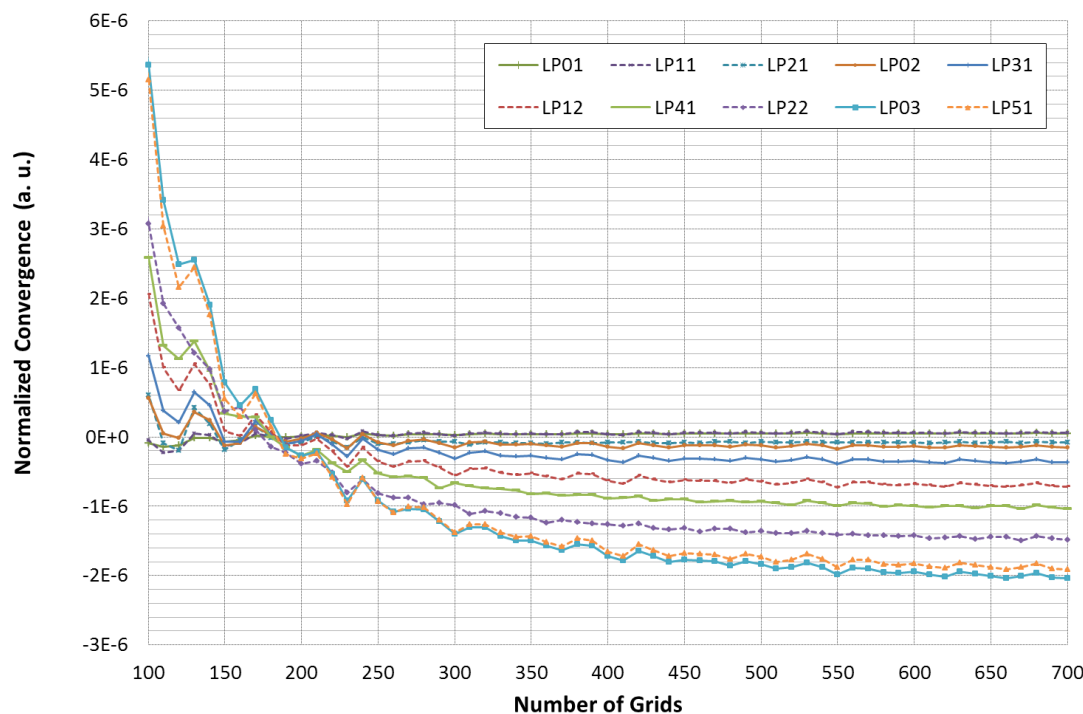


**Figure 4-17: Convergence curves of the MMF calculated with scalar-field FDFD and index-averaging factor 10**

We used the same calculation window size (**50 $\mu\text{m}$** ) for the vector-field simulations but found that some modes swap their orders and therefore made the results difficult to arrange. Consequently we increase the size of the calculation window to **100 $\mu\text{m}$** . **Figure 4-18** shows the corresponding convergence curves of the vector-field simulations. By comparing the results to the analytic values, we obtain the errors. The results are arranged in **Table 4-12** (scalar-field FDFD) and **Table 4-13** (vector-field FDFD).

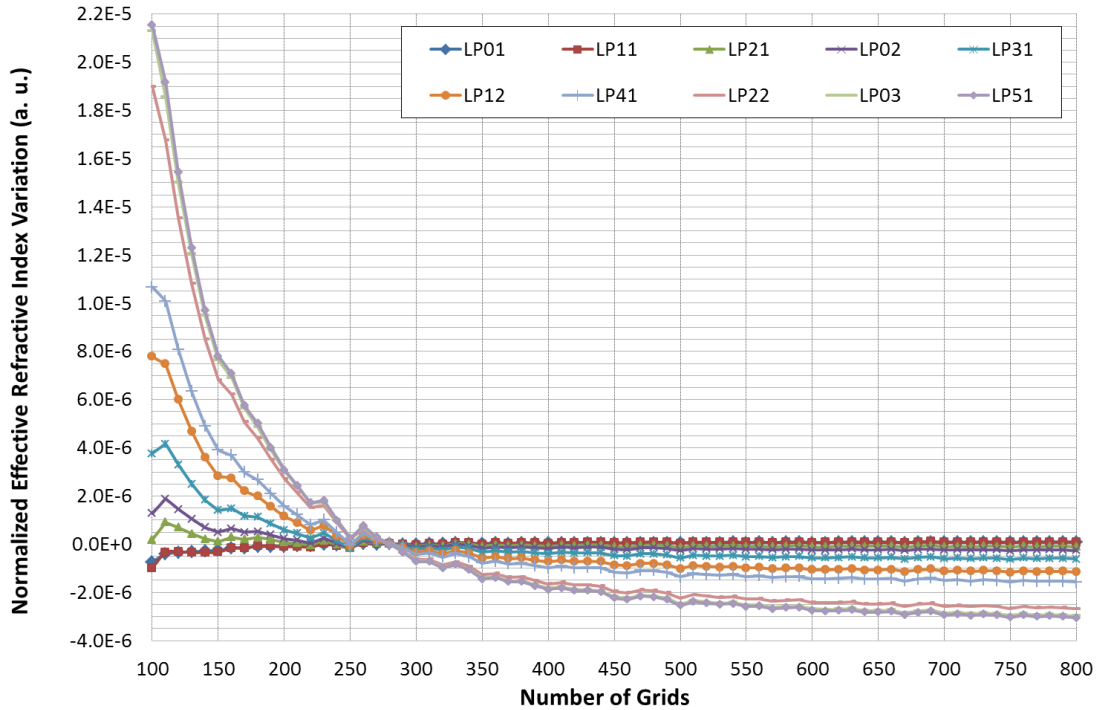


**Figure 4-18: Convergence curves of the MMF calculated with vector-field FDFD and index-averaging factor 10**

**Table 4-12: Scalar-field FDFD results on  $n_{\text{eff}}$  and errors of the  $LP_{lm}$  modes of the MMF**

$m \backslash l$	1	2	3
0	1.449147 (0ppm)	1.447645 (0ppm)	1.445109 (-8ppm)
1	1.448600 (0ppm)	1.446537 (-1ppm)	-
2	1.447888 (0ppm)	1.445309 (-2ppm)	-
3	1.447022 (0ppm)	-	-
4	1.446015 (-1ppm)	-	-
5	1.444880 (-2ppm)	-	-
6	-	-	-

For lower order modes, the simulation errors are in general of the order of few ppm. Other than  $n_{eff}$  and the number of modes that can be calculated analytically, through theory we also know that for  $LP_{lm}$  modes with  $l = 0$ , there exist two degeneracies (polarization) while for  $l > 0$ , there are four degeneracies (polarization and geometry) (Figure 4-19).

**Table 4-13: Vector-field FDFD results on  $n_{eff}$  and errors of the  $LP_{lm}$  modes of the MMF**

$m \backslash l$	1	2	3
0	1.449146 (-1ppm)	1.447644 (-1ppm)	1.445120 (-1ppm)
1	1.448600 (0ppm)	1.446537 (-1ppm)	-
2	1.447887 (-1ppm)	1.445311 (-1ppm)	-
3	1.447021 (-1ppm)	-	-
4	1.446015 (-1ppm)	-	-
5	1.444881 (-1ppm)	-	-
6	-	-	-

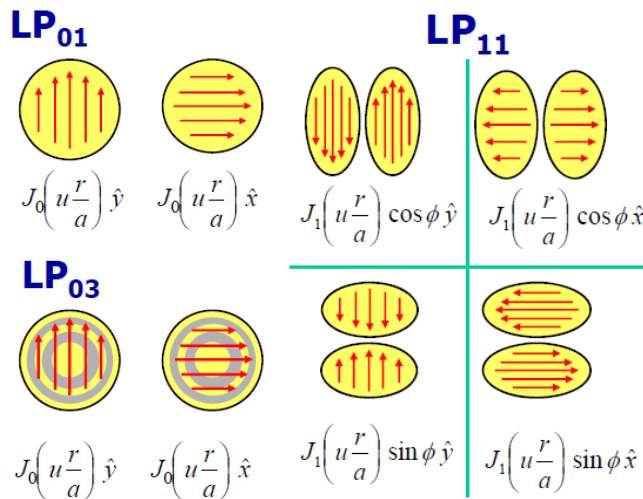


**Figure 4-19: Degeneracy of some  $LP_{lm}$  modes in a MMF**

Such degeneracy is observed in our simulations. With the scalar-field FDFD, because the polarization of fields is dropped, the degeneracy decreases by a factor of two (Figure 4-20). With the vector-field FDFD, the results match the theoretical degeneracy (Figure 4-21). Three two-fold degenerate modes and seven four-fold degenerate modes are

observed, which corresponds to results shown in **Figure 4-13** and **Table 4-10**.

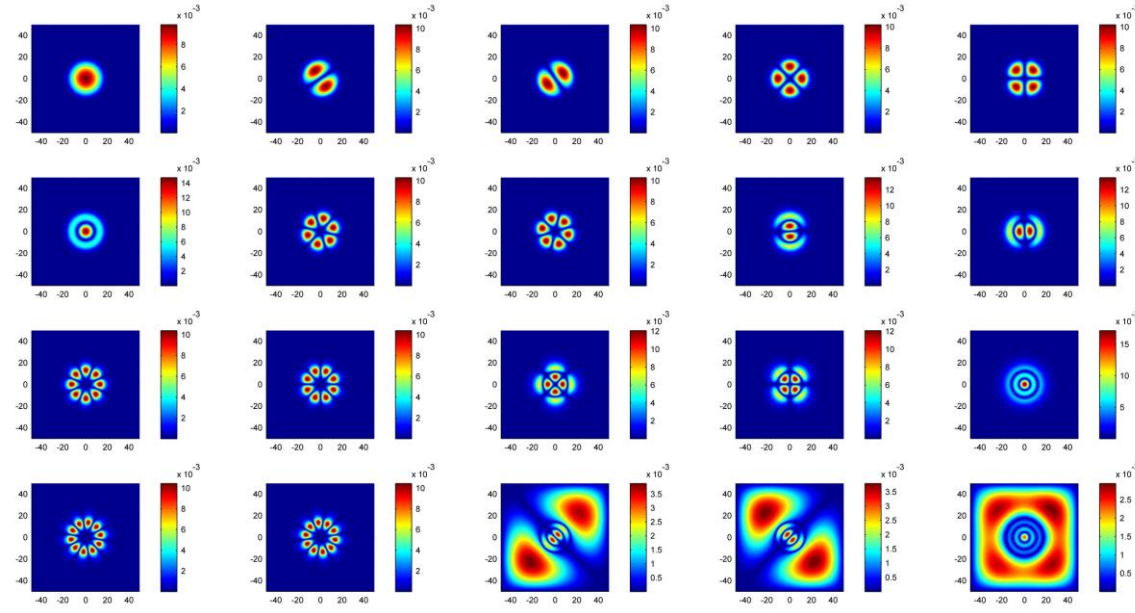


**Figure 4-20:** Eigenfields with the largest 20 eigenvalues of the MMF calculated with scalar-field FDFD

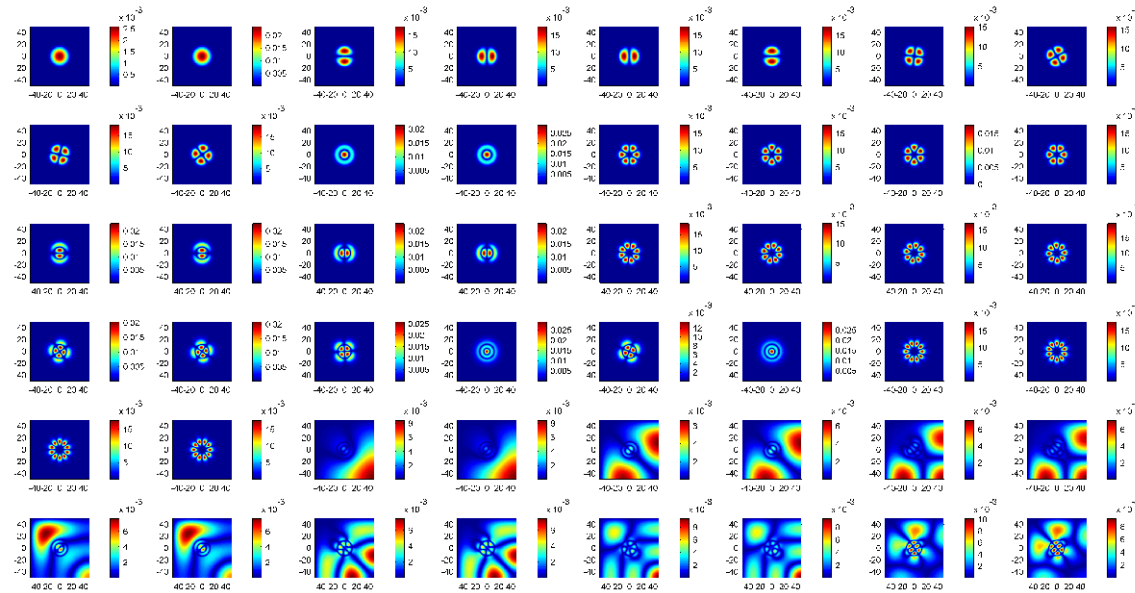


**Figure 4-21:** Eigenfields (Ex) with the largest 48 eigenvalues of the MMF calculated with vector-field FDFD

#### 4.7.4 High Index-Contrast Step-Index Fiber (HC-SIF)

We next consider a step-index fiber (SIF) with high index-contrast. We use the same geometry as introduced in [Zhu and Brown, 2002](#). Since we follow a similar formulation in our vector-field FDFD scheme, the results obtained verify whether our numerical implementation is valid. The fiber geometry is given in **Table 4-14**. The analytical value of the effective refractive index of the fundamental mode is **1.438604** ([Zhu and Brown, 2002](#)).

**Table 4-14: The HC-SIF for benchmarking**

Wavelength	1.5μm
Core Diameter	6μm
Core Refractive Index	1.45
Cladding Refractive Index	1.0
Δn	45%
Normalized Frequency, V	8.796459

Although as previously discussed, the scalar-field formulation with LP approximation is no longer valid when the index-contrast is high, we still like to show the results as a comparison. Similar to the previous two sections, we perform LP analysis on the HC-SIF and obtained the fundamental  $n_{eff}$ , **1.439051**. The error is **-0.000453 (>300ppm)** when compared with the analytical value (**1.438604**). This shows quantitatively the limit of the scalar-field LP approximation.

**Figure 4-22** gives the dispersion curves for  $I = 0$  to  $I = 10$ , and **Table 4-15** gives  $n_{eff}$  of the modes under the scalar-field LP approximation. We next perform simulations with both scalar-field and vector-field FDFDs. The common simulation parameters are shown in **Table 4-16**.

The resultant fundamental  $n_{eff}$  is **1.439054** for scalar-field FDFD and **1.438608** for vector-field FDFD, each of them more or less corresponds to its analytic counterpart (**1.439051** and **1.438604**, as derived earlier in this section). Calculation window of **12μm**, as in [Zhu and Brown, 2002](#), is used to ensure that the results are comparable.

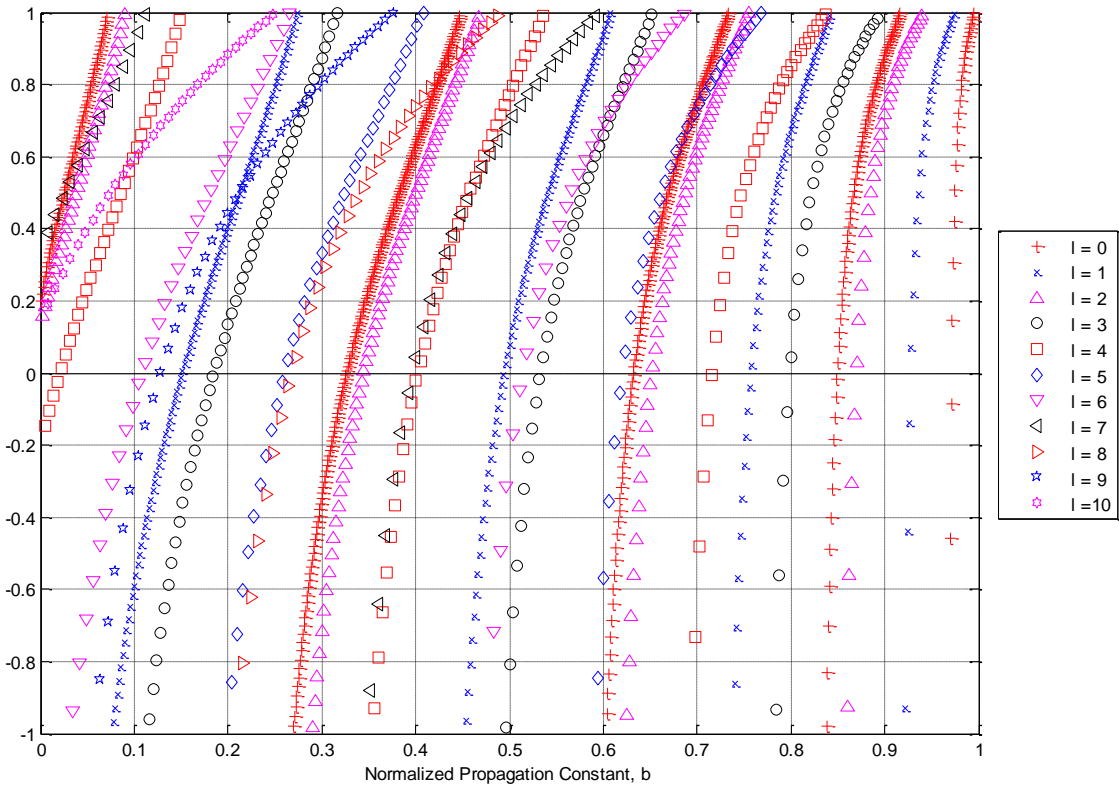


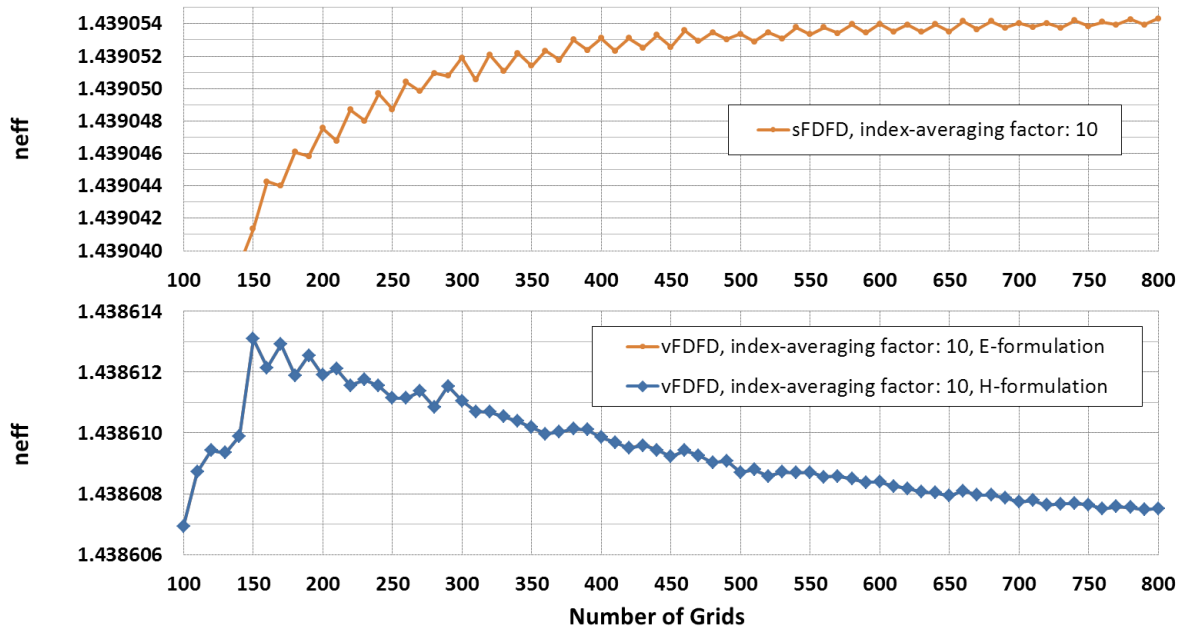
Figure 4-22: Dispersion relation curves of the HC-SIF from  $l = 0$  to  $l = 10$

Table 4-15:  $n_{eff}$  of the  $LP_{lm}$  modes of the HC-SIF

$m \backslash l$	1	2	3	4
0	1.439055	1.391548	1.302696	1.166173
1	1.422075	1.354578	1.242963	1.080239
2	1.399494	1.310865	1.174690	-
3	1.371369	1.260020	1.097285	-
4	1.337574	1.201483	1.011449	-
5	1.297841	1.134487	-	-
6	1.251754	1.058066	-	-
7	1.198724	-	-	-
8	1.137926	-	-	-
9	1.068203	-	-	-
10	-	-	-	-

**Table 4-16 Common FDFD simulation parameters for the HC-SIF**

Calculation Window (Convergence against Step Size)	12μm
Step Size (Convergence against Window Size)	0.05μm
Index-Averaging Factor (If Applied)	10

**Figure 4-23: Convergence curves of the fundamental  $n_{eff}$  of the HC-SIF with scalar-field FDFD (top) and vector-field FDFD (bottom)**

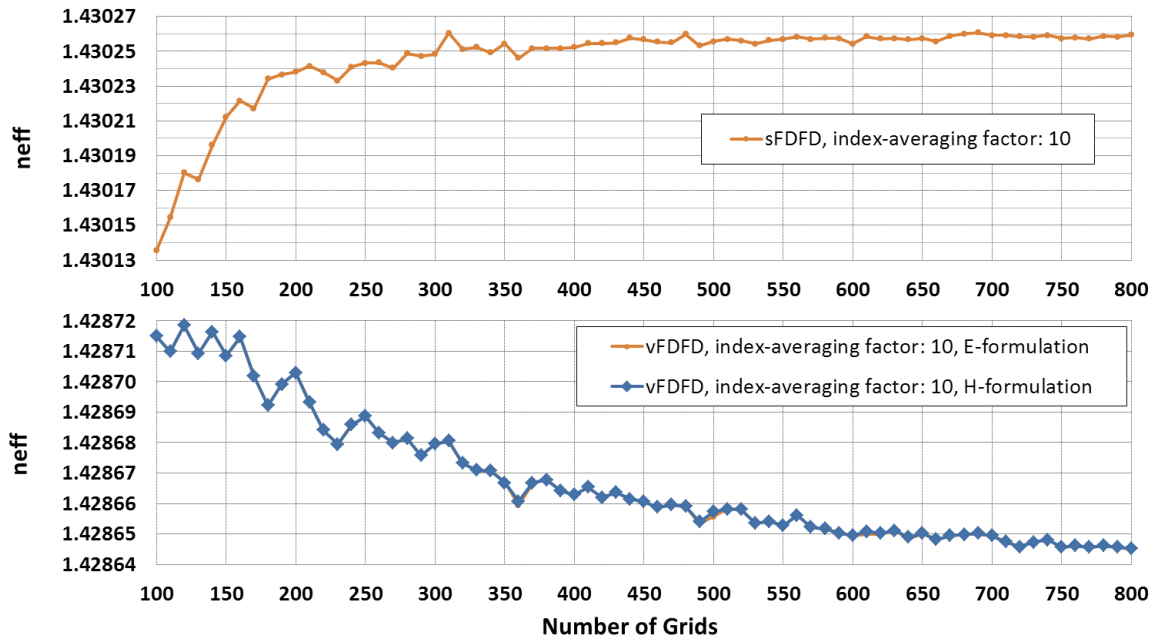
#### 4.7.5 Holey Fiber (HoF)

The next fiber geometry, a holey PCF, is also after [Zhu and Brown, 2002](#). The geometry is as shown in [Figure 3-1](#), with parameters specified in [Table 4-17](#). The results are shown and compared with reference values in [Figure 4-24](#) and [Table 4-18](#).

One concern of the triangular-lattice PCFs is the degeneracy of the fundamental modes. It has been shown both theoretically ([Steel et al., 2001](#)) and numerically ([Koshiba and Saitoh, 2001](#)) that, although there exists structural difference along the x- and the y- directions, the fundamental modes in two orthogonal polarization states are degenerate. Our simulation also confirms such degeneracy; the fundamental modes shown in [Figure 4-25](#) and [Figure 4-26](#) all have  $n_{eff} = 1.42864$  when calculated with 800 grids.

**Table 4-17: The HoF for benchmarking and the FDFD simulation parameters**

Wavelength	1.5 $\mu\text{m}$
Pitch, $\Lambda$	2.3 $\mu\text{m}$
Diameter, $d$	0.5 $\mu\text{m}$
$n_{\text{silica}}$	1.45
Calculation Window	$6\Lambda = 13.8\mu\text{m}$

**Figure 4-24: Convergence curves of the fundamental  $n_{\text{eff}}$  of the HoF with scalar-field FDFD (top) and vector-field FDFD (bottom)**

*It should be noted that for the vector-field simulations, the results from E-formulation and H-formulation overlap each other.*

**Table 4-18: Reference values on fundamental  $n_{\text{eff}}$  of the HoF and our simulation results**

Reference	Approach	Result
Mogilevtsev <i>et al.</i> , 1999	LFM	1.42805
Huang and Xu, 1993	FD-BPM	1.42868
Lüsсе <i>et al.</i> , 1994	FDFD	1.42858
Zhu and Brown, 2002	FDFD	1.42868
Current Work, Scalar-Field FDFD	FDFD	1.43026
Current Work, Vector-Field FDFD	FDFD	1.42864

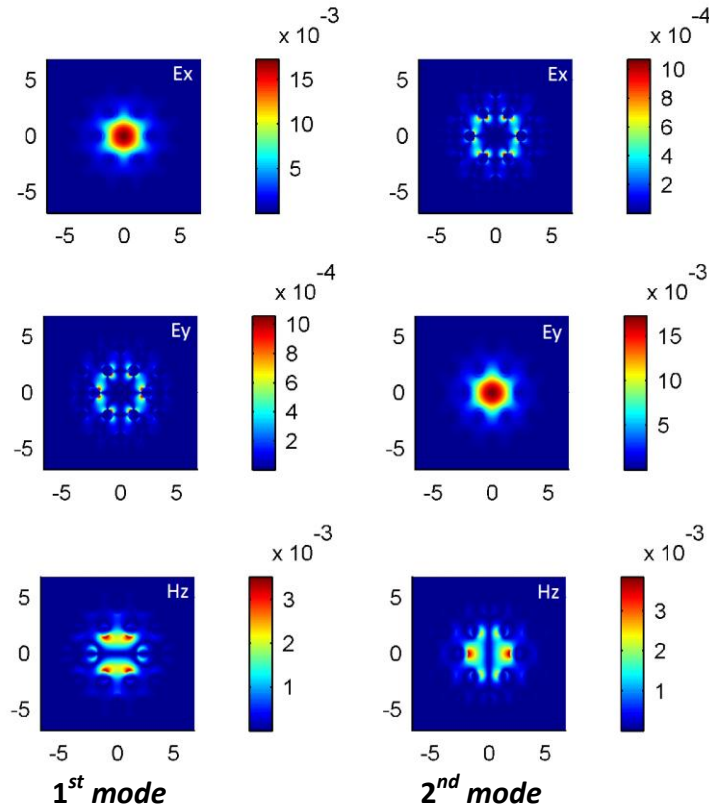


**Figure 4-25: The 1<sup>st</sup> and 2<sup>nd</sup> sets of eigenfields in E-formulation (Ex-Ey-Hz) of the HoF**

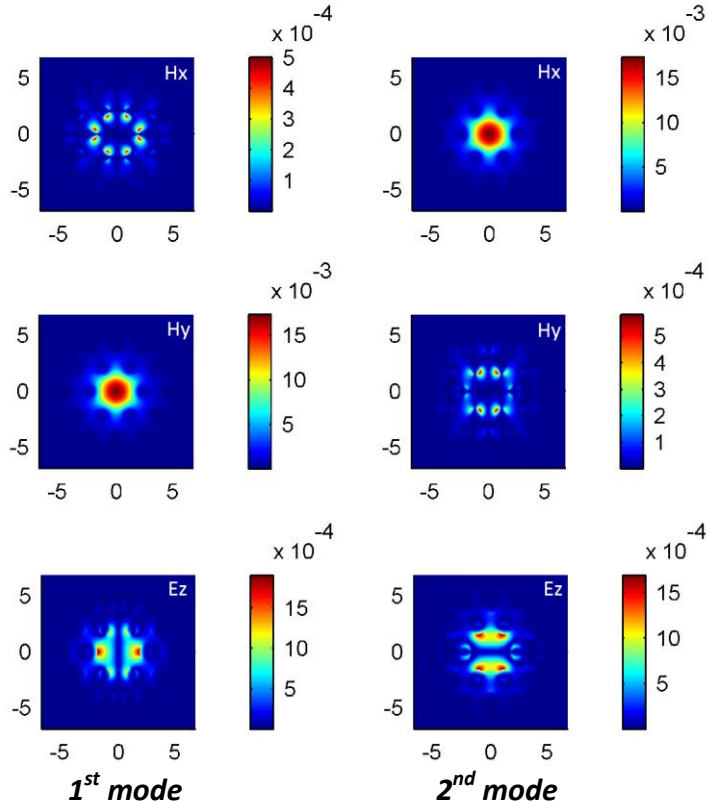


**Figure 4-26: The 1<sup>st</sup> and 2<sup>nd</sup> sets of eigenfields in H-formulation (Hx-Hy-Ez) of the HoF**

#### 4.7.6 Summary on Benchmarking of FDFD

The performance with **800** grid points and index-averaging of the FDFDs implemented is summarized in **Table 4-19**.

**Table 4-19: Benchmarking results of the scalar-field FDFD and the vector-field FDFD**

Mode		Reference	Scalar-Field FDFD	Relative Error	Vector-Field FDFD	Relative Error
Single-Mode Fiber	LP <sub>01</sub>	1.446535	1.446534	1ppm	1.446530	4ppm
Multi-Mode Fiber	LP <sub>01</sub>	1.449147	1.449147	0ppm	1.449146	-1ppm
	LP <sub>11</sub>	1.448600	1.448600	0ppm	1.448600	0ppm
	LP <sub>21</sub>	1.447888	1.447888	0ppm	1.447887	-1ppm
	LP <sub>02</sub>	1.447645	1.447645	0ppm	1.447644	-1ppm
	LP <sub>31</sub>	1.447022	1.447022	0ppm	1.447021	-1ppm
	LP <sub>12</sub>	1.446538	1.446537	-1ppm	1.446537	-1ppm
	LP <sub>41</sub>	1.446016	1.446015	-1ppm	1.446015	-1ppm
	LP <sub>22</sub>	1.445312	1.445309	-2ppm	1.445311	-1ppm
	LP <sub>03</sub>	1.445121	1.445109	-8ppm	1.445120	-1ppm
	LP <sub>51</sub>	1.444883	1.444880	-2ppm	1.444881	-1ppm
High Index-Contrast Step-Index Fiber	Fund.	1.438604	1.439054	313ppm	1.438608	3ppm
Holey Fiber	Fund.	1.42805	1.43026	0.2%	1.42864	413ppm

#### 4.8 Summary on Implemented FDFDs

So far we have compared our simulation results with well-known fiber geometries, and our FDFD schemes are qualified to give good and consistent results. However, in this thesis we emphasize on numerical schemes available for PLCFs, so it is essential to test our FDFD schemes with related fiber geometries. Mostly likely due to the newly developed concepts of PLCFs, there has not been much work in literature that gives good reference values. As a result, we will proceed directly to the PLCF of interest and discuss the results in **Chapter 5**. On the other hand, as proposed in **Section 4.7.1**, we can still perform analysis on convergence curves against the sizes of the grid and the computation

window to auto-verify the numerical schemes themselves. Furthermore, thanks to the six-fold symmetry of the PCF considered, it may also be interesting to compare the results obtained under different numerical configurations for an identical physical structure.

To sum up, in this chapter we discussed the scalar-field FDFD and the vector-field FDFD implemented in this thesis and tested them with some exemplary fiber geometries with three verification concepts. We show quantitatively the limitation of the scalar-field calculation, its difference to the vector-field calculation, and the errors of the FDFDs compared with analytical values. The proposed vector-field FDFD, based on [Zhu and Brown, 2002](#), gives good results for the single-mode, multi-mode, and high-contrast step-index fiber geometries. When vector-field FDFD is applied, relative error of **3ppm** is observed for  $n_{eff}$  of the fundamental mode in HC-SIF. For the holey fiber geometry, the result of the vector-field FDFD differs by **6E-4 (413ppm)** from that of the localized function method. On the other hand, it should be noted the results obtained with scalar-field FDFD have larger errors, with **313ppm** for HC-SIF and **0.2%** for HoF, which are approximately **100** times and **5** times larger than with vector-field FDFD, respectively.

Computational power (memory requirement, in particular) appears to be a concern regarding the convergence of the simulations. The specification of the computer used for the simulations in this chapter can be found in [Appendix D](#). One can always perform the benchmarking with more powerful computers, however, from the results in this chapter we have gained confidence of the FDFD schemes despite computational limitations. Since in this thesis we set an emphasis on PLCFs, it is therefore better to apply our tools to the real battlefield. In the next chapter we will discuss the PCF 070124 and the PLCF sample, which is PCF 070124 infiltrated with a LC commonly known as **6CHBT**.

## 5 Photonic Liquid Crystal Fiber of Interest

### 5.1 Photonic Liquid Crystal Fiber Geometry

The PCF chosen for our studies is **PCF 070124**, with three rings of air holes, manufactured by Maria Curie-Skłodowska University (Uniwersytet Marii Curie-Skłodowskiej, UMCS) in Lublin, Poland. The geometry and the optical microscope image of the PLCF are shown in **Figure 5-1**, together with the liquid crystal chosen for infiltration. We choose a 3-ring PCF for its smaller transverse extent and thus the possibility to include the entire periodic structure in the numerical simulations.

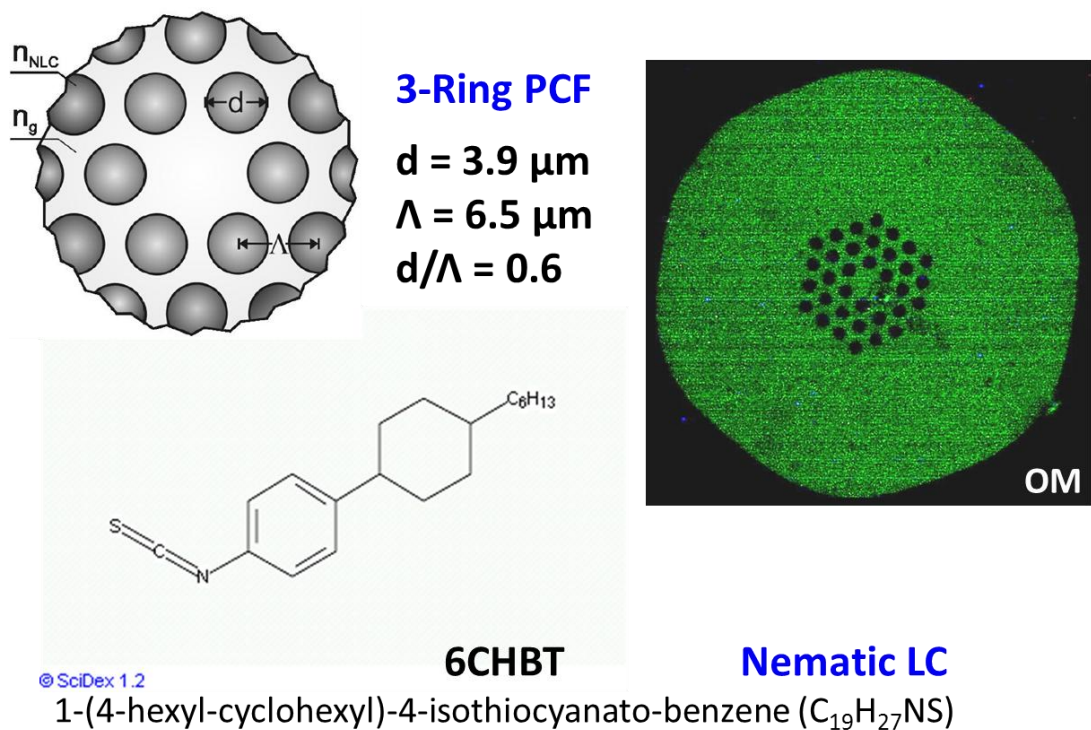


**Figure 5-1: PLCF of interest, showing the three-ring host PCF 070124, the nematic LC, 6CHBT, and the optical microscope image**

### 5.2 Liquid Crystal for Infiltration

**6CHBT** (also commonly known as **6CPS**) is chosen to be the LC for infiltration. The optical properties regarding **6CHBT** can be found in [Schirmer et al., 1997](#). The chemical structure of **6CHBT** is shown in [Figure 5-1](#) and the corresponding uniaxial nematic liquid crystal (N-LC) model in [Figure 5-2](#).

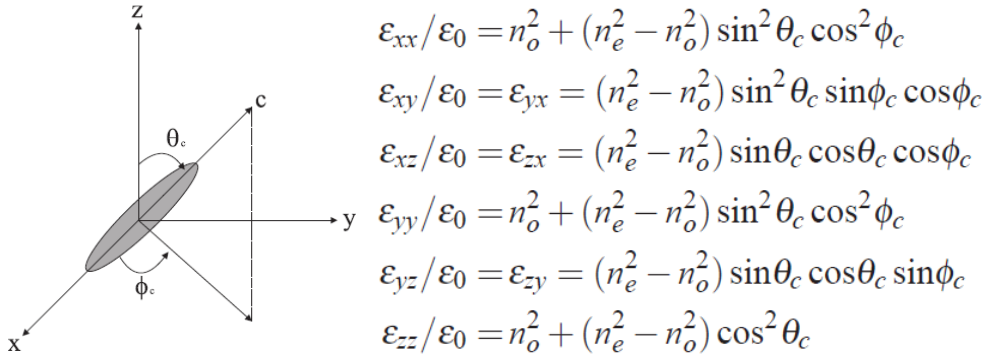


**Figure 5-2: Uniaxial nematic liquid crystal (N-LC) model**

### 5.3 Molecular Arrangements of Liquid Crystals

After infiltrating the liquid crystal molecules into the holes of the host PCF, several possible molecular arrangements can be obtained. [Figure 5-3](#) shows some steady-state molecular arrangements, after [Wolinski et al., 2006](#), and [Figure 5-4](#) shows variants of molecular arrangements which can be obtained under external fields, after [Ertman et al., 2009](#).

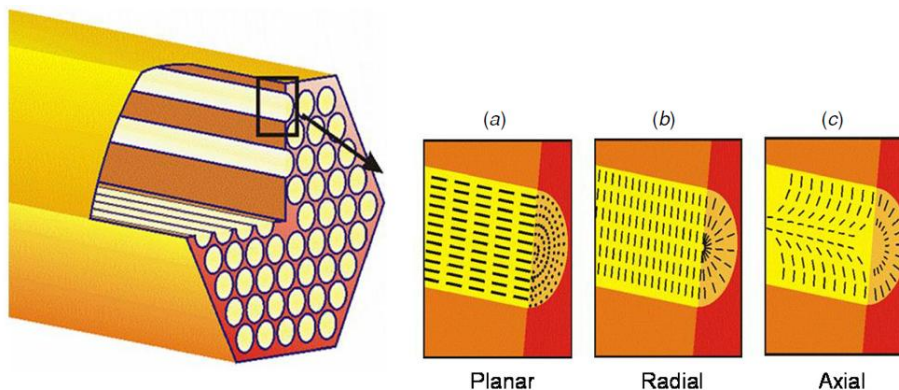


**Figure 5-3: Molecular arrangements of LC inside the holes of PCF**

(a) Planar, (b) Radial and (c) Axial

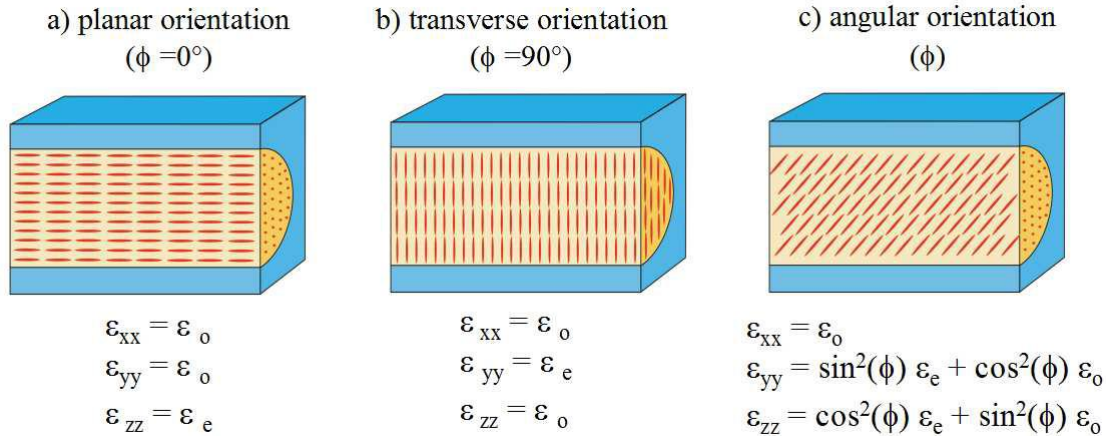


**Figure 5-4: Variants of molecular arrangements of LC inside the holes of PCF**

## 5.4 PLCF Sample Preparation

The sample PLCF consists of two parts: the empty PCF and the LC-infiltrated PLCF, all together in the form of a single fiber. The PLCF samples are prepared with respect to the following procedures:

- 1) An empty PCF with certain length is prepared.
- 2) The protective layers on both ends is striped and the end-facets are cleaved.
- 3) Light from a laser diode is focused by an objective onto one end-facet of the empty PCF.
- 4) The other end of the PCF is immersed into LC.
- 5) LC molecules infiltrate into the holes by capillary force (**Figure 5-5**).
- 6) The part of the PCF that is infiltrated by LC molecules becomes lossy and therefore the infiltration process can be monitored via observation of fiber losses (**Figure 5-5**).
- 7) After infiltration, the PLCF end-facet is cleaved again, and the residual LC molecules on the end-facet is removed with proper cleaning.

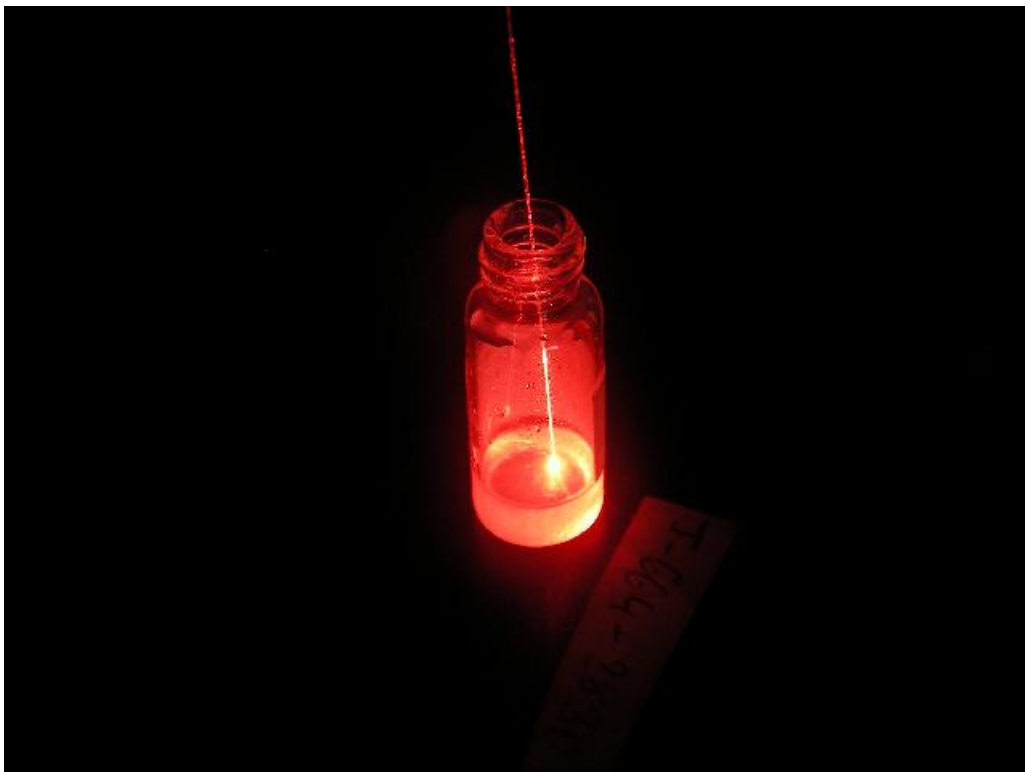


**Figure 5-5: PCF immersed in LC**

*The liquid crystal molecules infiltrate into the PCF with capillary force. The infiltration can be monitored as the PCF gets lossy after infiltration. The index-guiding PCF is transformed into a PBG-guiding PLCF after infiltration and becomes selective on wavelength.*

A video clip of the infiltration process can be found in the attached CD of the thesis, under the name “LC\_Infiltration.mp4”. **Figure 5-6** shows some selected frames of the video clip tagged with time. Note that the time 00’00 indicates the start of the video, not the infiltration process. The LC molecules raise much faster in the beginning, then slow down gradually, and finally reach a limit.

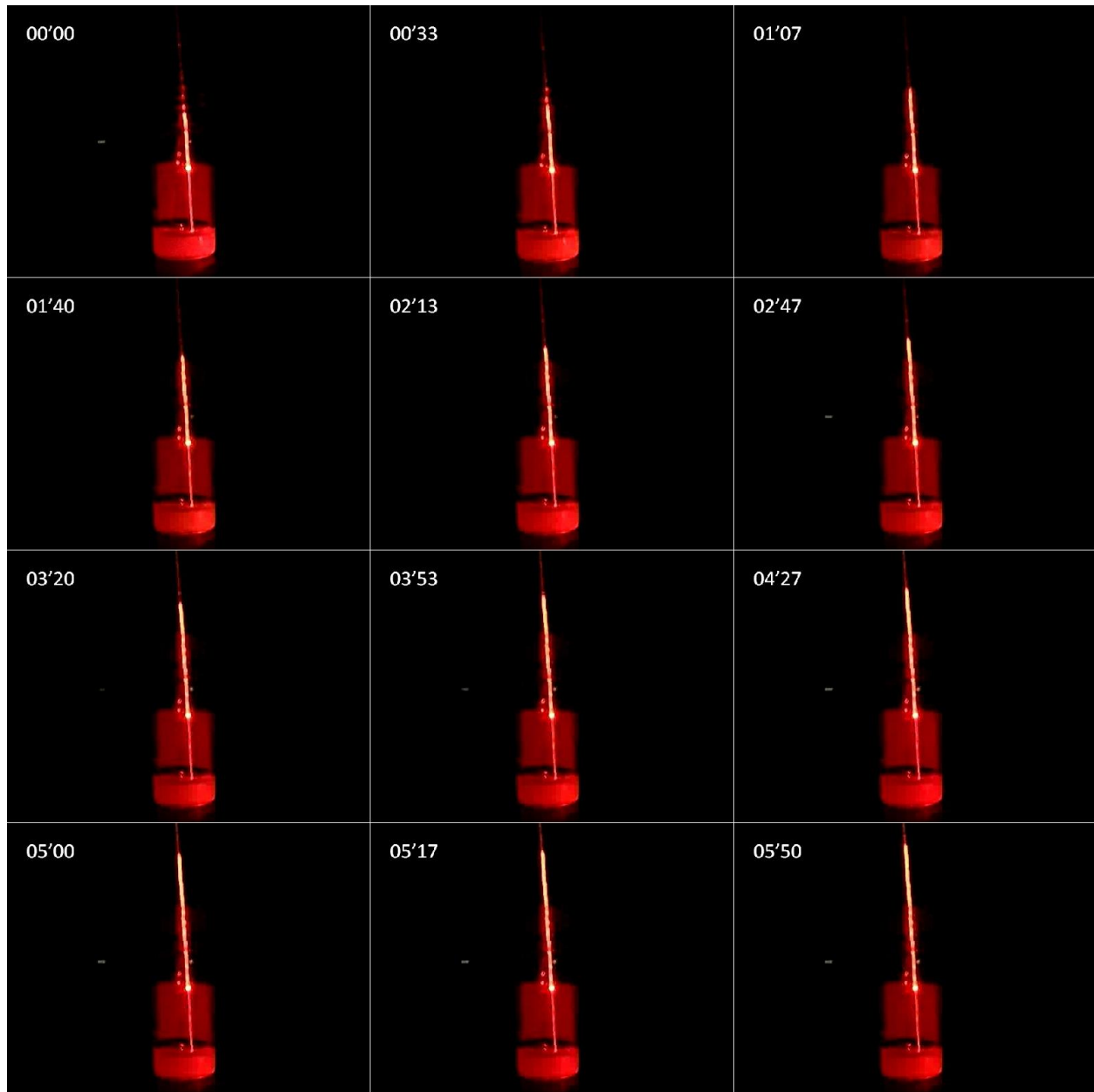


Figure 5-6: Selected frames from the LC infiltration video clip

## 5.5 Experimental Setup

The experimental setup for measuring the transmission spectra of PLCFs is shown in **Figure 5-7**. A white light source (Ocean Optics Halogen Calibration Light Source HL-2000-CAL and HL-2000-CAL-ISP) is focused onto the empty PCF end facet by an objective. A probing single-mode fiber (SMF), is then attached in proximity to the PLCF end facet and connected to the spectrometer. The signal is analyzed by a fiber optics spectrometer (Ocean Optics HR4000) with spectral resolution of around **0.25nm**. A Peltier

module is used to heat up or cool down the PLCF sample. A Testo 735 precise thermometer with **0.05°C** resolution and **0.1°C** accuracy is used to monitor temperature changes.

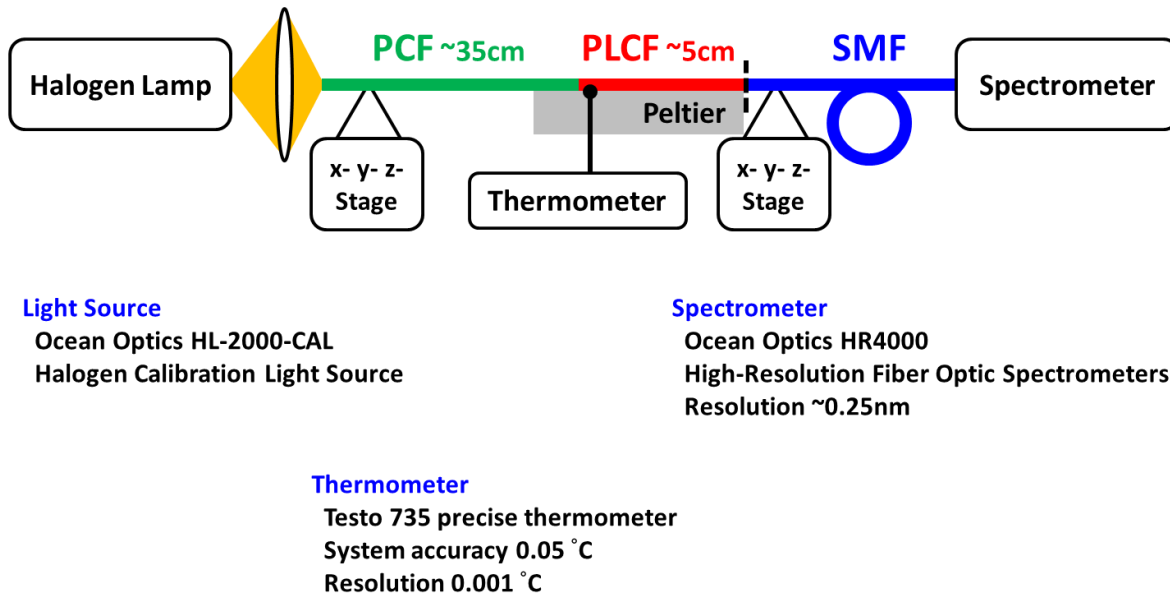


Figure 5-7: Experimental setup

## 5.6 Numerical Setup

### 5.6.1 Refractive Index of Silica

The refractive index of silica is well described by the common Sellmeier equation (4.33) with coefficients shown in **Table 4-6**. However, since we are interested in the behaviors with respect to temperature change, we adopt the temperature-dependent two-term Sellmeier dispersion relation,

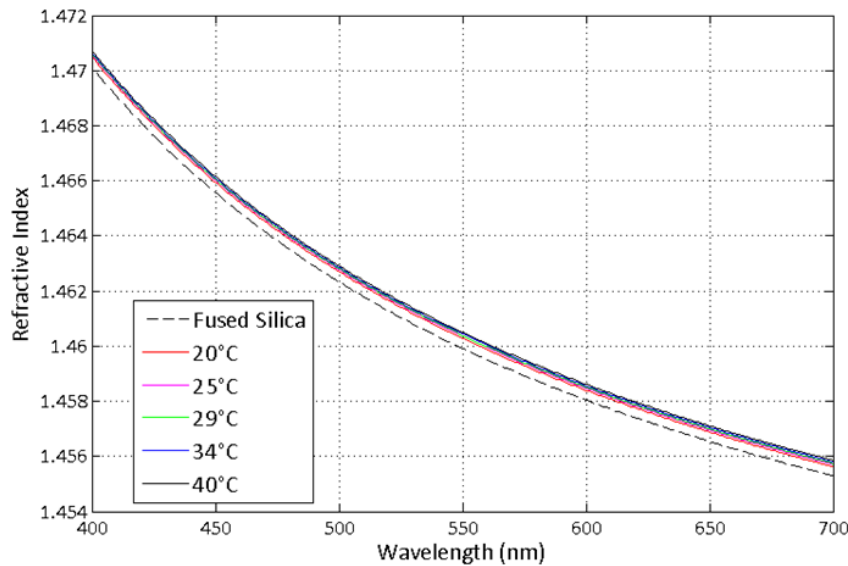
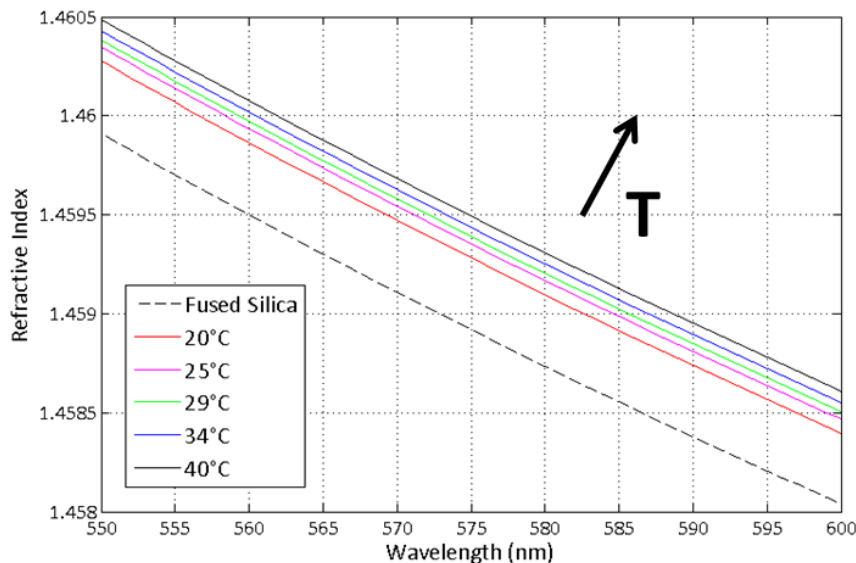
$$n^2 = A + \frac{B\lambda^2}{\lambda^2 - C} + \frac{D\lambda^2}{\lambda^2 - E}. \quad (5.1)$$

with coefficients from [Medhat et al., 2002](#). One term is due to electric resonance absorption and the other term is due to the lattice/ionic resonance absorption, where **n** is the refractive index, **λ** is the wavelength in **μm**. **A**, **B**, **C**, **D** and **E** are material-dependent Sellmeier coefficients. The coefficients are given in **Table 5-1**, and the corresponding dispersion curves of silica are shown in **Figure 5-8** and **Figure 5-9**. The common dispersion curve for fused silica is drawn in dashed line, tagged 'Fused Silica'.

**Table 5-1: Temperature-dependent Sellmeier coefficients for silica**

Temperature	A	B	C ( $\mu\text{m}^2$ )	D
20°C	1.311382	0.794229	0.010951	0.999525
25°C	1.309557	0.796189	0.010936	0.986365
29°C	1.308097	0.797703	0.010924	0.975837
34°C	1.306272	0.799595	0.010909	0.962676
40°C	1.304082	0.801867	0.010891	0.946884

\* $E = 100 \mu\text{m}^2$ . ([Medhat et al., 2002](#))

**Figure 5-8: Temperature dependent dispersion curves of silica****Figure 5-9: Temperature dependent dispersion curves of silica (zoom in)**

The refractive index of silica ( $n_{\text{silica}}$ ) rises with temperature.

### 5.6.2 Refractive Index of 6CHBT

The refractive index of liquid crystal is generally described by the Cauchy equation:

$$n_{e,o} \cong A_{e,o} + \frac{B_{e,o}}{\lambda^2} + \frac{C_{e,o}}{\lambda^4}. \quad (5.2)$$

However, [Schirmer et al., 1997](#) has measured the refractive index of a mixture of nCHBT (nCPS, [Figure 5-10](#)), and fitted the experimental data using single band model:

$$n_{e,o} \cong 1 + G_{e,o} \frac{\lambda^2 \lambda_{e,o}^2}{\lambda^2 - \lambda_{e,o}^2}, \quad (5.3)$$

and gave the coefficients as shown in [Figure 5-11](#).

COMPOSITION	n	m	wt%	T <sub>Nf</sub> /°C
	4		30.23	40.0
	6		33.34	
	8		36.43	

nCPS

**Figure 5-10: The mixture of nCHBT (nCPS)**

Alkyl chains with  $n$  carbon atoms ( $C_nH_{2n+1}$ ) are named  $R$ , with  $n$  given in the third column.

LC	T/°C	$n_e(589\text{ nm})$	$\lambda_0/\text{nm}$	$G_0/10^{-5}\text{ nm}^{-2}$	$\sigma/10^{-3}$
nCPS	20	1.5215	125.8	3.147	0.99
	30	1.5227	126.8	3.099	1.12

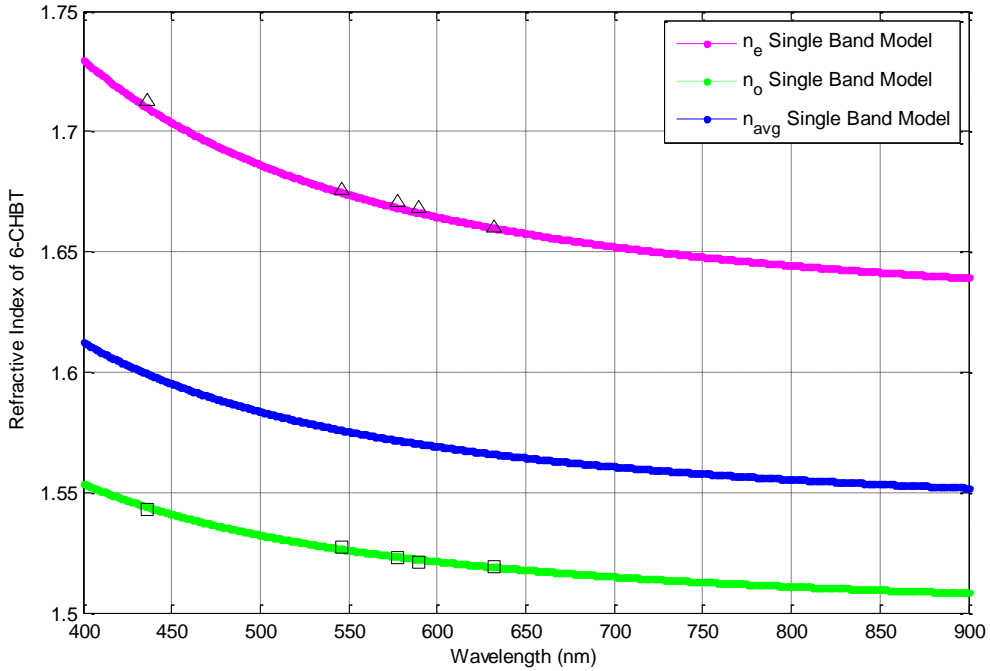
  

LC	T/°C	$n_e(589\text{ nm})$	$\lambda_e/\text{nm}$	$G/10^{-5}\text{ nm}^{-2}$	$\sigma/10^{-3}$
nCPS	20	1.6792	156.7	2.569	0.90
	30	1.6631	154.6	2.584	0.88

**Figure 5-11: Coefficients for nCHBT (nCPS) mixture with single band model**

After [Schirmer et al., 1997](#).

We use the single band model and the corresponding coefficients in our simulations. The refractive indices at temperatures between **20°C** and **30°C** are obtained through interpolation. As an example, the ordinary and extraordinary dispersion curves at **T=28°C** are plotted in [Figure 5-12](#).



**Figure 5-12: Ordinary and extraordinary dispersion curves of 6CHBT at T=28°C**

The ordinary ( $n_o$ ) and extraordinary ( $n_e$ ) refractive indices of 6CHBT are larger than that of fused silica ( $n_{silica} \sim 1.46$ ) over the spectral range of concern. This infers whenever there exist a guiding mode in the silica core, it is formed by the PBG-guiding mechanism.

### 5.6.3 Numerical Auto-Verification and Comparison with Experimental Results

Following the idea of numerical verification in **Section 4.7.1**, we perform auto-verification of the numerical scheme with the PLCF of interest and its host PCF structure in the following sections. Both scalar-field and vector-field FDFD are considered. The averaged refractive index of liquid crystal:

$$n_{avg} = \frac{2}{3} n_o + \frac{1}{3} n_e \quad (5.4)$$

is used in the scalar-field FDFD. For comparison, we also perform simulations on such ‘isotropic’ PLCF with the vector-field FDFD.

As there is no good analytical reference for simulations on PLCFs, we also try to compare the numerical results with experimental results in addition to the numerical auto-verification. We recall that in **Section 4.7.1** it is mentioned that owing to the limit of experimental means, direct qualitative comparison is not quite accessible. Instead, we compare the results qualitatively. What come to our mind that can be easily compared

are:

- 1) Field intensity distribution, and
- 2) Transmission spectrum

In the next two sections, we will discuss about some characteristics of the empty host PCF and the PLCF sample with these bases.

## 5.7 Experimental and Numerical Results for the Host PCF

### 5.7.1 Field Intensity Distribution

In FDFD simulations, the first-hand results obtained are the effective refractive index ( $n_{eff}$ ) and the modal field distribution, which correspond to the eigenvalue and the eigenfield (eigenvector), respectively. With vector-field schemes, it is also possible to obtain polarization information regarding the eigenfield and the derived parameters such as polarization mode dispersion (PMD, birefringence), polarization extinction ratio and dichroic ratio. The eigenfields can be compared with experimental results, although one of the problems is that the intensity distribution after propagation in the fiber depends on the initial field (input beam profile).

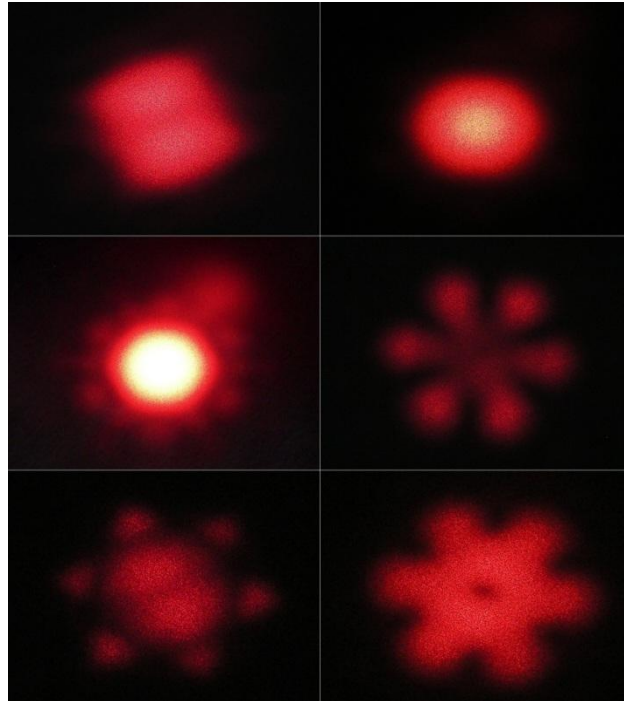


Figure 5-13: Experimental results on far-field intensity distribution of an empty PCF 070124

**Figure 5-13** shows some experimental results on far-field intensity distributions of an empty PCF 070124, with the same light source but different initial fields tuned by coupling conditions. Provided that one can orientate the PCF precisely, with polarimetric elements it is also possible to obtain information regarding polarization states of the fields. By observing the speckle effect, we find that light fields at the output of the empty PCF 070124 are spatially coherent.

We perform vector-field FDFD on the host PCF with the simulation parameters shown in **Table 5-2**. Edge-cutting was performed to reduce spurious results. An exemplary set of eigenfields ( $E_x$  &  $E_y$ ) at  $\lambda = 555\text{nm}$  is shown in **Figure 5-16**, and the corresponding effective refractive indices of the first six modes are given in **Table 5-3**.

As clearly seen, the first two modes are degenerate upon polarizations. To justify the simulations, we perform convergence analysis with PCF 070124 and the results are shown in **Figure 5-14**. The more details eigenfield patterns of the first two modes are given in **Figure 5-17** (E-formulation,  $E_x-E_y-H_z$ ) and **Figure 5-18** (H-formulation,  $H_x-H_y-E_z$ ). Such degeneracy has been reported both theoretically ([Steel et al., 2001](#)) and numerically ([Koshiba and Saitoh, 2001](#)) in literature.

**Table 5-2: Vector-field FDFD simulation parameters for PCF 070124 and the PLCF sample**

Calculation Window	50 $\mu\text{m}$ (x) by 43.75 $\mu\text{m}$ (y)
Grid Size	0.125 $\mu\text{m}$
Index-Averaging Factor	4

**Table 5-3: Vector-field FDFD results on  $n_{eff}$  of the first six modes in PCF 070124**

Mode	$n_{eff}$ , E-Formulation	$n_{eff}$ , H-Formulation
1 <sup>st</sup>	1.461344	1.461344
2 <sup>nd</sup>	1.461344	1.461344
3 <sup>rd</sup>	1.460455	1.460455
4 <sup>th</sup>	1.460450	1.460450
5 <sup>th</sup>	1.460452	1.460452
6 <sup>th</sup>	1.460452	1.460452

In order to compare the field patterns in experiments and in numerical simulations, we sort out the core-guiding modes of the empty PCF from our simulations with more eigenvalues calculated. The result for  $E_x$  is shown in **Figure 5-15**.

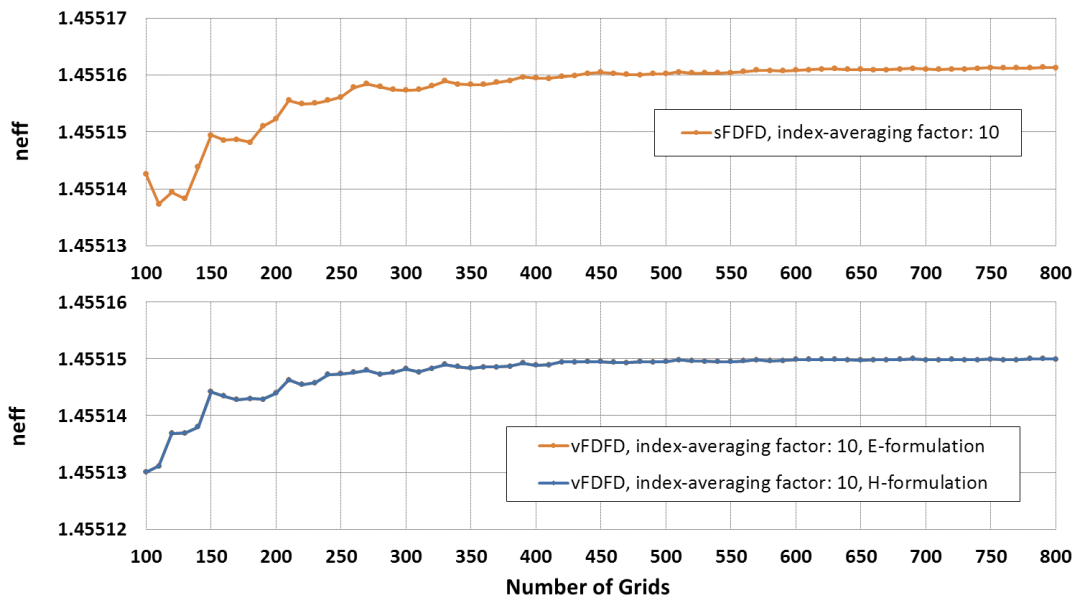


Figure 5-14: Convergence curves of the fundamental  $n_{eff}$  of PCF 701024 with respect to the number of grids calculated with scalar-field FDFD (top) and vector-field FDFD (bottom)

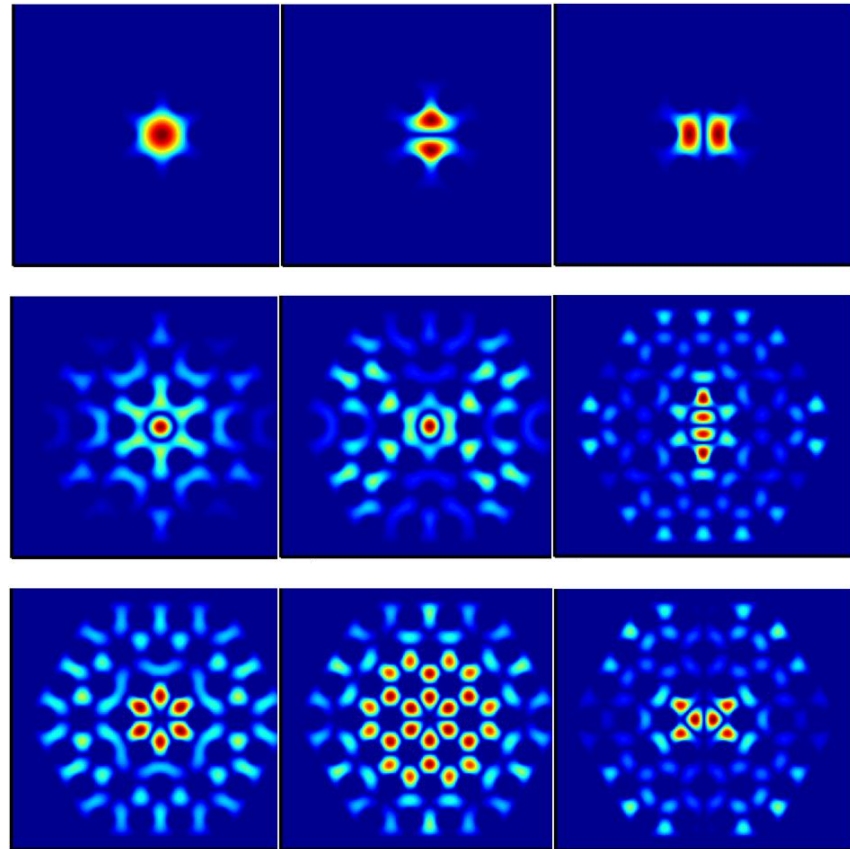


Figure 5-15: Eigenfields (Ex) of the core-guiding modes of PCF 070124

Comparing the experimental and numerical results of field patterns, we can see that the principle components of the core-guiding modes often possess the  $C_6$  six-fold rotational symmetry.



**Figure 5-16: Exemplary set of eigenfields of PCF 070124 at  $\lambda = 555\text{nm}$  calculated with vector-field FDFD (top: Ex, bottom: Ey)**

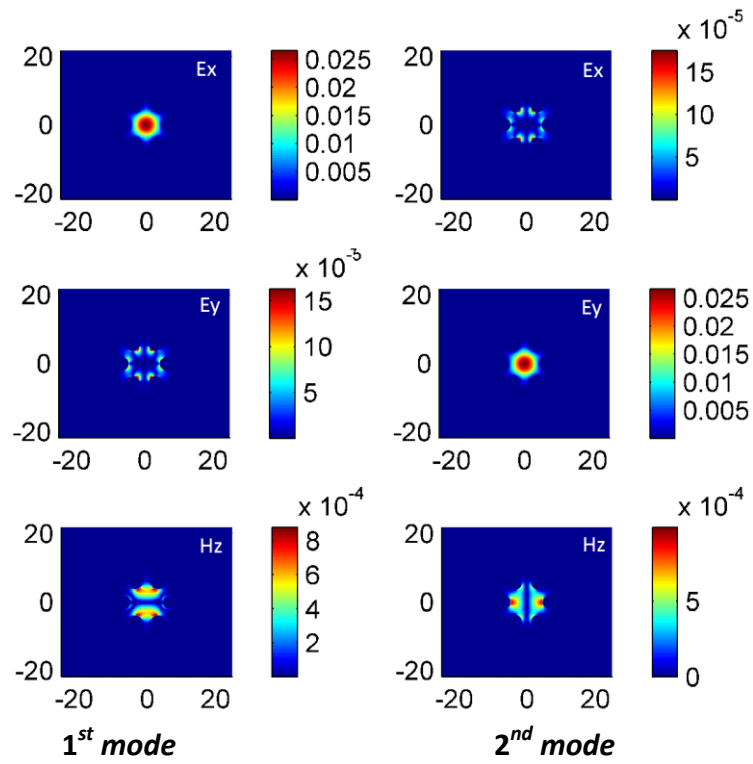


Figure 5-17: The 1<sup>st</sup> and 2<sup>nd</sup> sets of eigenfields in E-formulation (Ex-Ey-Hz) of PCF 070124

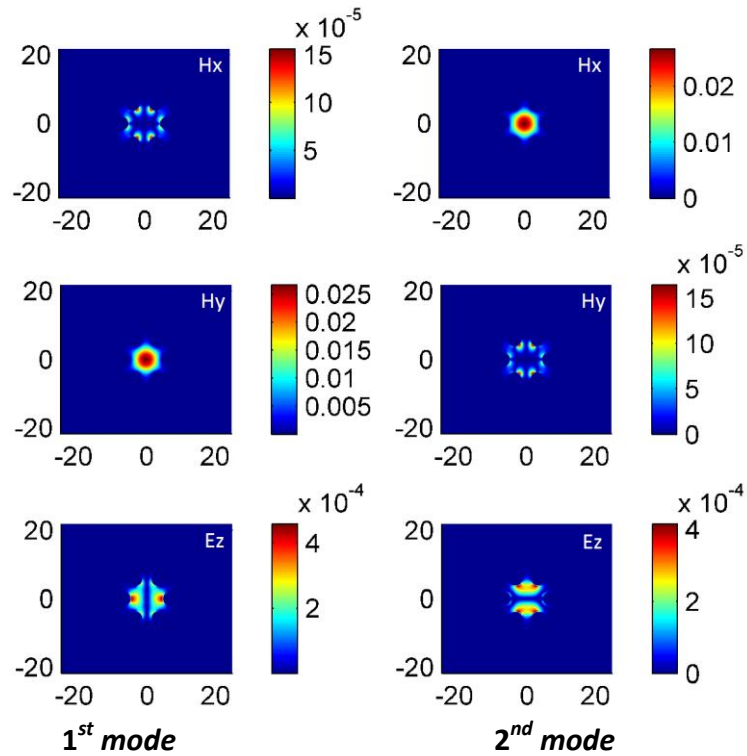
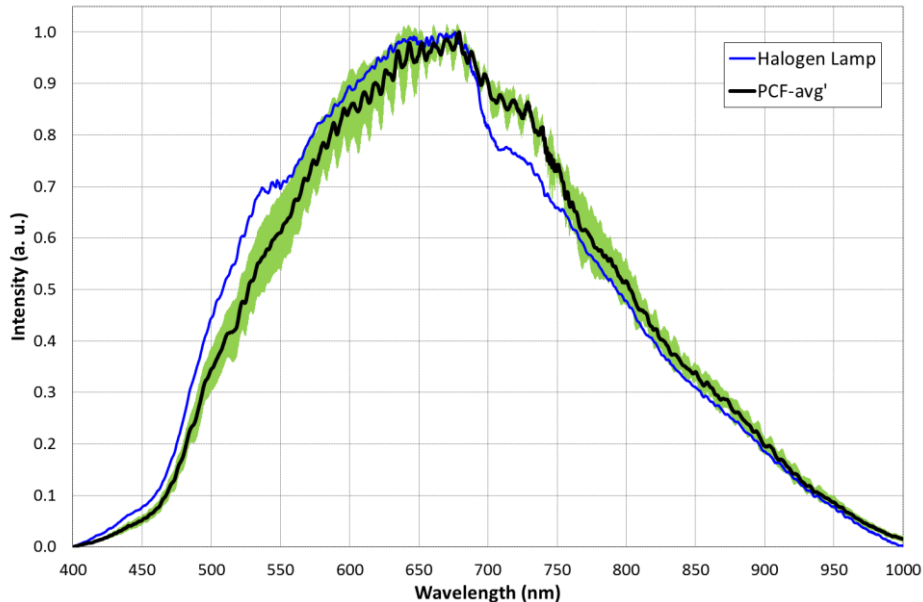


Figure 5-18: The 1<sup>st</sup> and 2<sup>nd</sup> sets of eigenfields in H-formulation (Hx-Hy-Ez) of PCF 070124

### 5.7.2 Transmission Spectrum

One characteristic that can be easily measured with our experimental setup is the transmission spectrum shown in **Figure 5-19**. We can see that the transmission spectrum of an empty PCF 070124 is continuous. This can be compared numerically if we perform suitable simulations over specific range of wavelengths. In our simulations we find that similar eigenfield patterns, as shown in **Figure 5-16**, exist for different wavelengths. This coincides with the continuous transmission spectrum in experiments. The fundamental  $n_{\text{eff}}$  with respect to wavelength is shown in **Figure 5-20**.



**Figure 5-19: Experimental results on transmission spectrum of an empty PCF 070124**

The blue line shows the normalized spectrum of the light source together with the probing single-mode fiber. The black line shows the normalized spectrum of the empty PCF 070124, together with the light source and the probing single-mode fiber. The green shade shows the uncertainty of the measurements. We note that the background (blue) and the data (black) were not measured simultaneously and there might have been fluctuations in the spectrum of the light source.

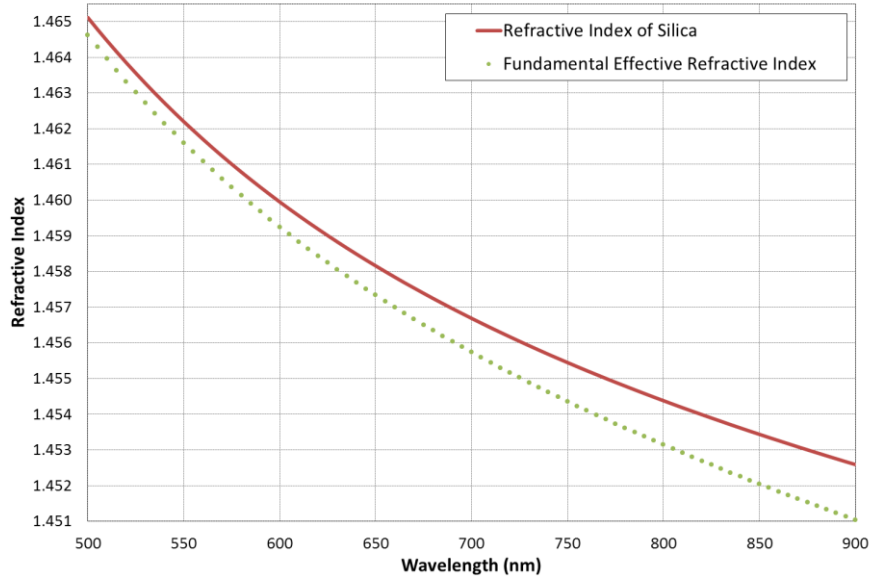


Figure 5-20: Numerical results on fundamental  $n_{eff}$  vs. wavelength of PCF 070124

## 5.8 Experimental and Numerical Results for the PLCF Sample

### 5.8.1 Field Intensity Distribution

First we observe the far-field intensity distribution of the PLCF sample (Figure 5-21).

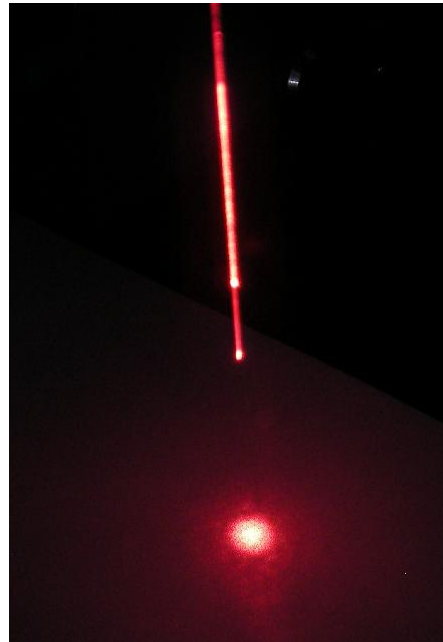
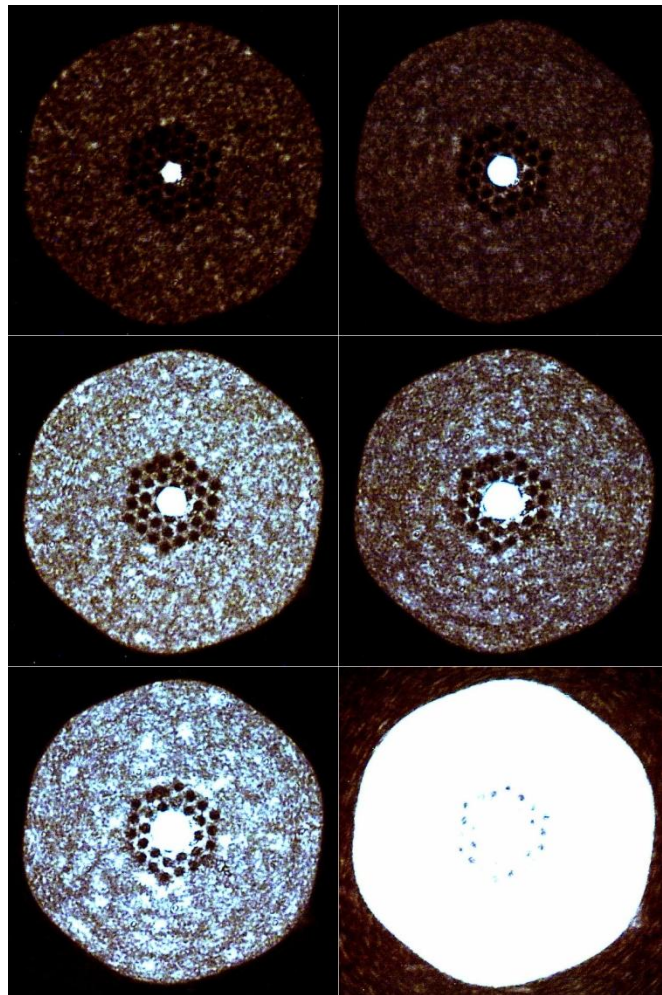


Figure 5-21: Experimental result on far-field intensity distribution of the PLCF sample

The far-field intensity distribution does not show much information, owing to the lossy nature of PLCF. To verify guiding of light by the PLCF but not the whole fiber strand, we proceed to near-field intensity distribution in **Figure 5-22** under different light levels. It is clearly seen that the light is guided within the core when the light level is low. However, when the light level is high, more light leaks to the regions outside the photonic crystal cladding and is thus guided by the whole fiber strand. One concern that might rise is whether this portion of the guided light affects the characteristics of the PLCF.



**Figure 5-22: Experimental results on near-field intensity distribution of the PLCF sample at different light levels**

We perform vector-field FDFD on the PLCF sample with the same simulation parameters as shown in **Table 5-2**, along with the edge-cutting technique to reduce spurious results. An exemplary set of eigenfields ( $E_x$ ,  $E_y$ ) at  $\lambda = 686\text{nm}$  is shown in **Figure 5-24**. The corresponding  $n_{eff}$  of the first two modes are **1.455222** and **1.455219**, which appears to

show that the two polarizations are not degenerate. However, the difference is so small that we cannot conclude on the degeneracy.

It is worth to recall here that for the PLCF of interest, the refractive indices ( $n_o$ ,  $n_e$ ) of **6CHBT** is larger than that of silica ( $n_{silica}$ ). Accordingly, in the simulations for the PLCF sample, guiding modes within the silica core are obtained as a result of the PBG-guiding mechanism.

On the other hand, in addition to the core-guiding modes and the cladding modes as seen for the empty PCF, some hole-guiding modes are also observed (**Figure 5-23**). Such possibilities of modes further increase the number of spurious results when searching for core-guiding modes. As seen in **Figure 5-23**, the hole-guiding modes are often characterized by  $n_{eff}$  larger than  $n_{silica}$ . Consequently, if we can specify the range of eigenvalues to be sought during the eigen solving process, as discussed in **Section 4.5.3**, we can possibly reduce the number of spurious results.

Another important observation from the eigenfield patterns is that, unlike the index-guiding empty PCF 070124, the eigenfield patterns of the PBG-guiding PLCF sample change sharply with wavelength, and for some wavelengths, there exist no core-guiding modes within the simulation range. The simulation range is the maximum absolute difference between the  $n_{eff}$  calculated and  $n_{silica}$ . It depends largely on the amount of spurious results, as will be discuss in the next section.

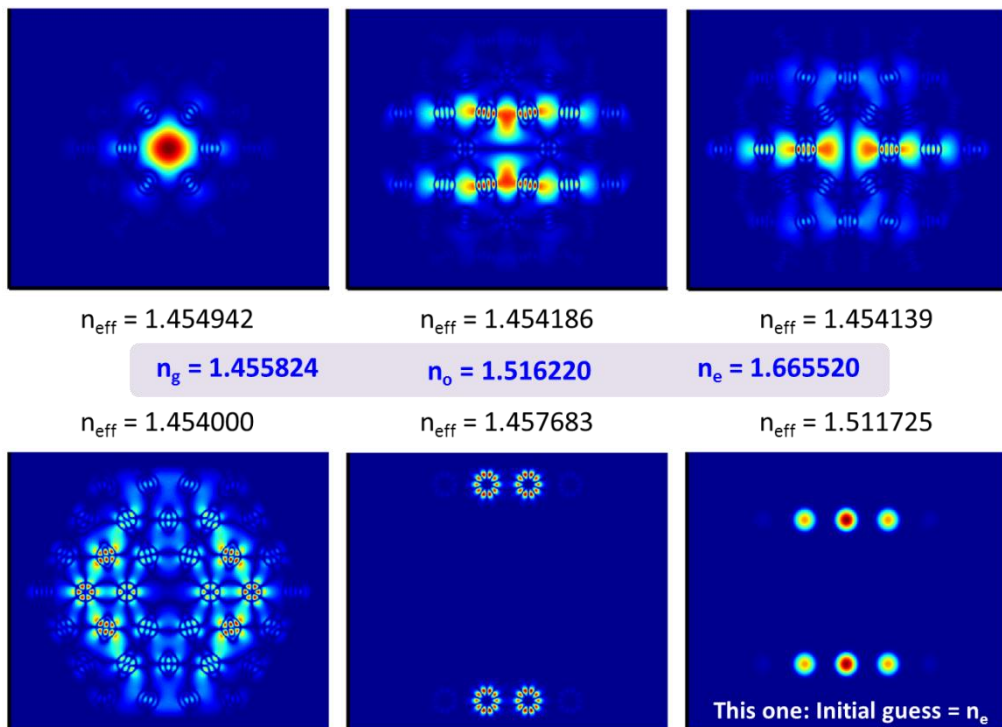
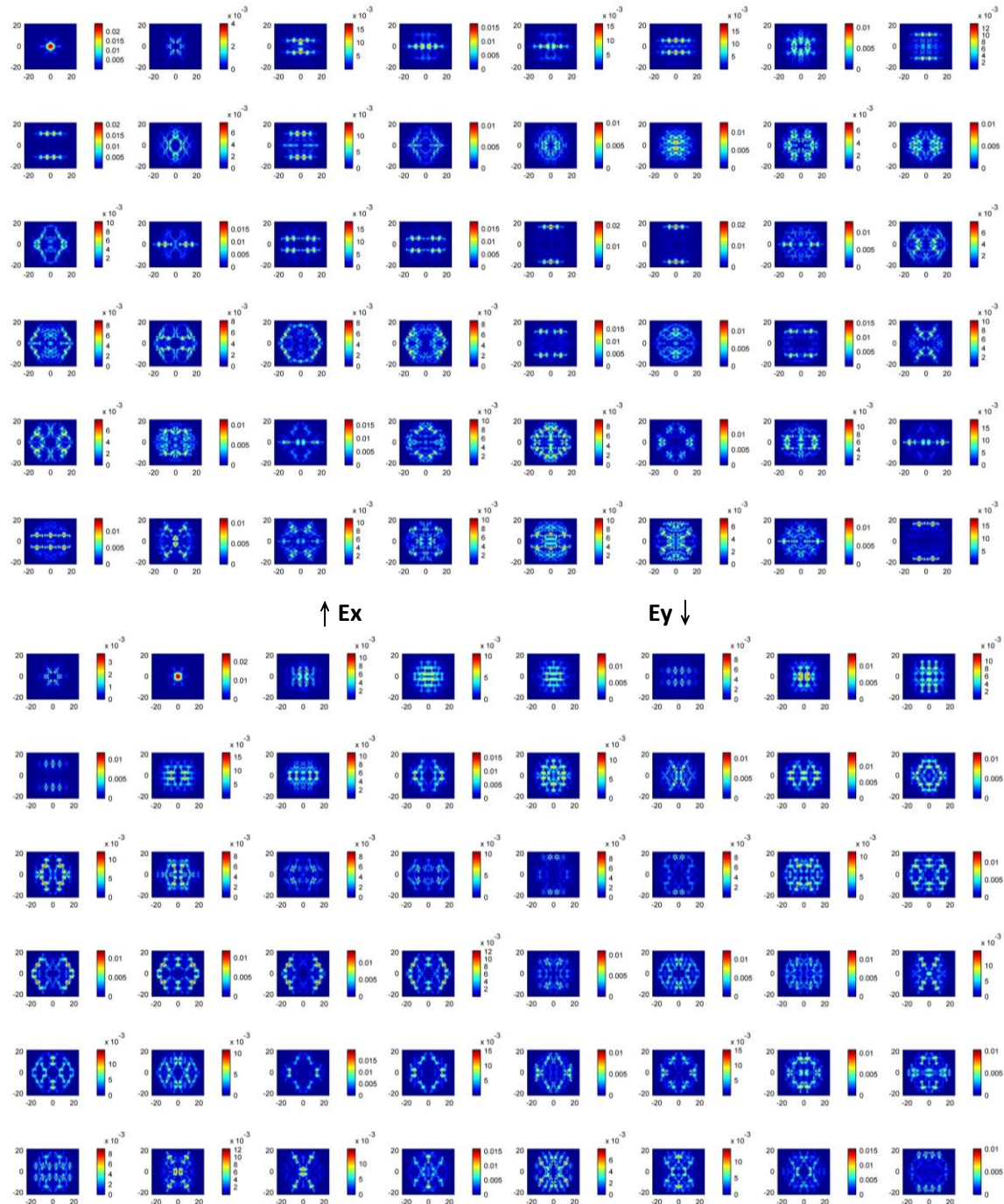
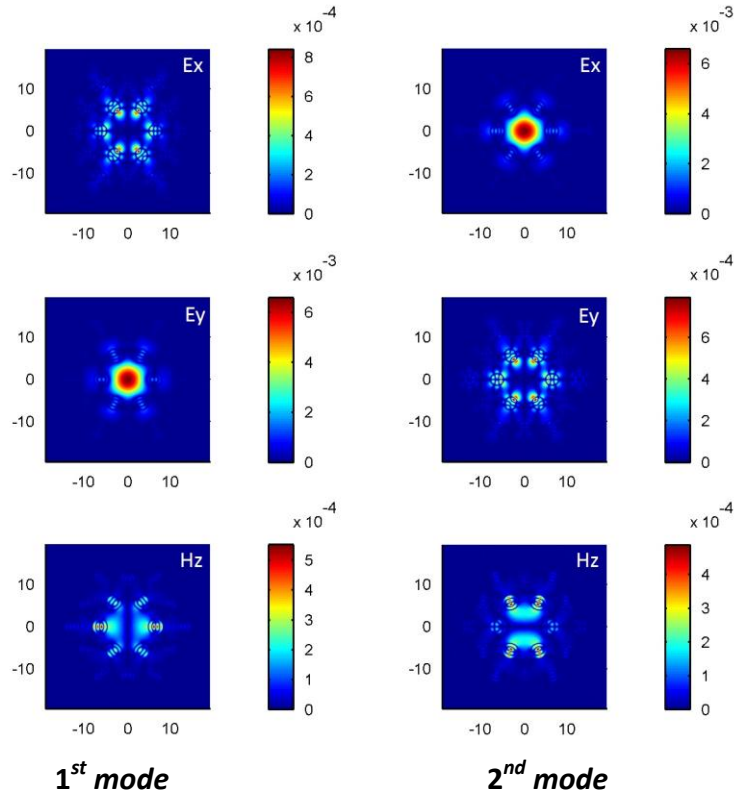


Figure 5-23: Types of modes (Ex) of the PLCF sample calculated with vector-field FDFD

With vector-field FDFD, the three components of the eigenfields are obtained and shown in **Figure 5-25** and **Figure 5-26**. It is worth mentioning here that these are PBG-guiding modes and have very different field patterns compared to those of the empty PCF host shown in **Figure 5-17** and **Figure 5-18**.



**Figure 5-24: Exemplary set of eigenfields of the PLCF sample at  $\lambda = 686\text{nm}$  with vector-field FDFD (top: Ex, bottom: Ey)**



**Figure 5-25: The 1<sup>st</sup> and 2<sup>nd</sup> sets of eigenfields in E-formulation (Ex-Ey-Hz) of the PLCF sample**

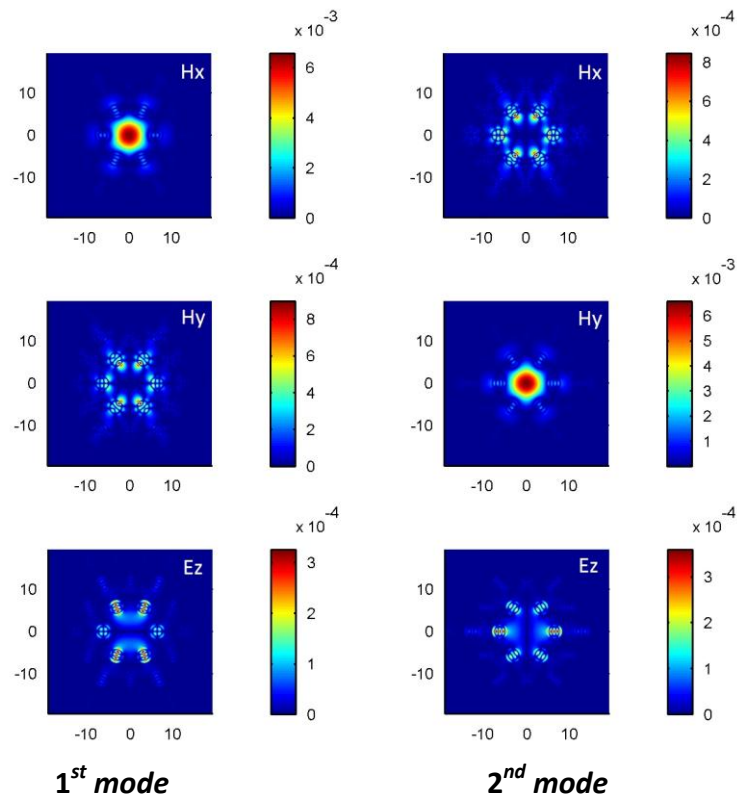


**Figure 5-26: The 1<sup>st</sup> and 2<sup>nd</sup> sets of eigenfields in H-formulation (Hx-Hy-Ez) of the PLCF sample**

### 5.8.2 Transmission Spectrum

The transmission spectrum of the PLCF sample is also measured for comparison with numerical results (**Figure 5-27**). We see that there exist several transmission peaks in the spectral range of the light source. Such selectivity on wavelength is characteristic of the PBG-guiding mechanism. **Figure 5-28** shows the numerical results on fundamental  $n_{eff}$  vs. wavelength of the PLCF sample, with the experimental results on transmission spectrum in background for comparison. The simulation is set to seek the first **48** eigenvalues and the corresponding eigenfields (eigenvectors). The core-guiding modes of each wavelength are then manually inspected and their effective refractive indices are extracted. As previously stated, the eigenfield patterns of the PBG-guiding PLCF sample change sharply with wavelength, and for some wavelengths, there exist no core-guiding modes within the simulation range. In view of the transmission spectrum, this coincides with the discrete transmission bands in experiments. The numerical simulation also shows ‘gaps’ in the transmission spectrum, but does not match entirely with the experimental results (**Figure 5-28**).

We would like to note the problem of spurious modes. In **Figure 5-28** the peach shade shows the range of eigenvalues obtained in the simulations. At the nodes of the shade, spurious results might have ruined the simulation. However, it is also possible that at and close to these nodes various cladding modes and hole-guiding modes exist. As a result, the PLCF sample no longer functions as an optical waveguide.

To verify the results of our simulations, we first perform convergence analysis, and then try to extend the range of the simulations. The convergence curves are shown in **Figure 5-29** and **Figure 5-30**, with respect to number of grids and grid size in  $\lambda$ , respectively. We note that the 1<sup>st</sup> and 2<sup>nd</sup> core-guiding modes mentioned in the figures are as those shown in **Figure 5-24**. A second note is that because these modes have very close  $n_{eff}$ , sometimes the 1<sup>st</sup> mode is quasi-x-polarized while sometimes the 2<sup>nd</sup> mode is quasi-x-polarized. When the  $n_{eff}$  of the two quasi-polarized modes are equal, the modes are degenerate. From **Figure 5-29** and **Figure 5-30** we can see that, with sufficient number of grids, the fundamental modes are degenerate. By fitting the curve with respect to the square of grid size, we obtain **1.455170** as a reference value for the fundamental  $n_{eff}$ . Using this reference, we see that with **800** grids, the simulation converges to about **1ppm**.

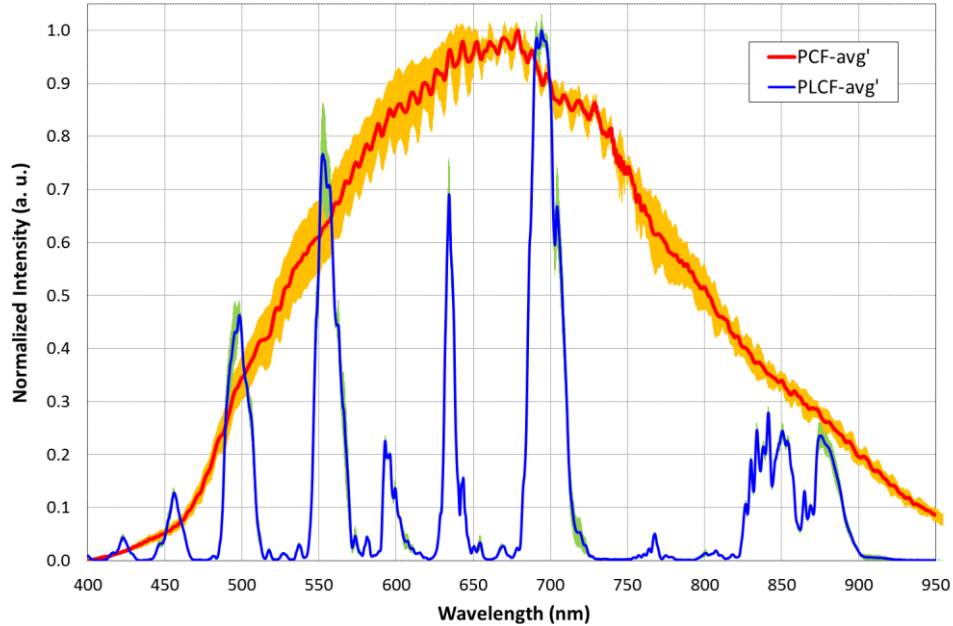


**Figure 5-27: Experimental results on transmission spectrum of the PLCF sample**

The red line shows the normalized spectrum of the light source together with the probing single-mode fiber and the empty PCF 070124. The blue line shows the normalized spectrum of the PLCF sample, together with the light source, the probing single-mode fiber, and the empty PCF 070124. The orange and green shades show the uncertainties of the measurements.

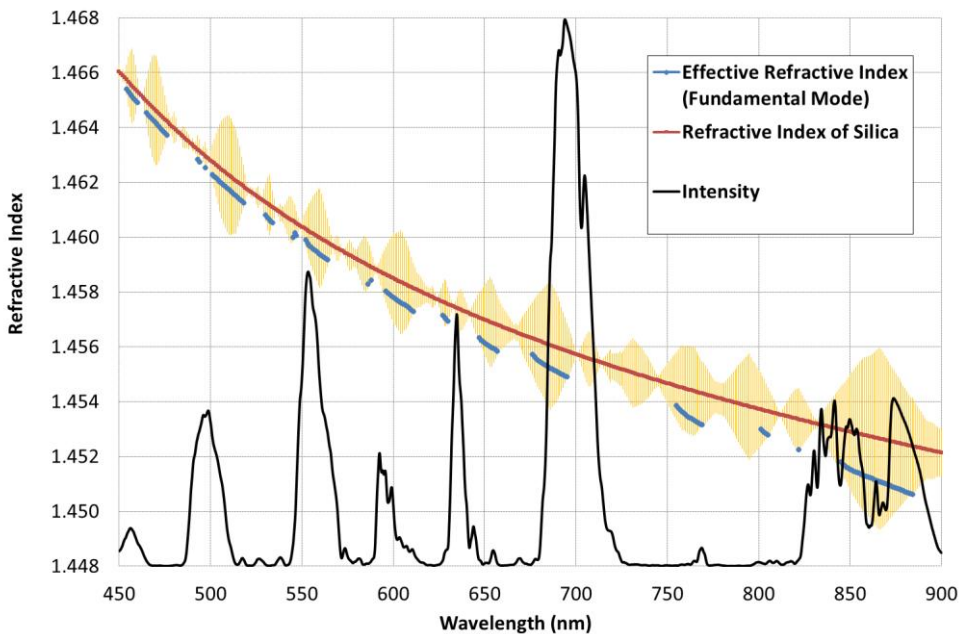


**Figure 5-28: Numerical results on fundamental  $n_{eff}$  vs. wavelength of the PLCF sample**

The eigenvalue range of simulations is shaded in peach. The transmission spectrum is normalized to [1.448 1.468] in background for comparison among the transmission peaks and the obtained bands of core-guiding modes.

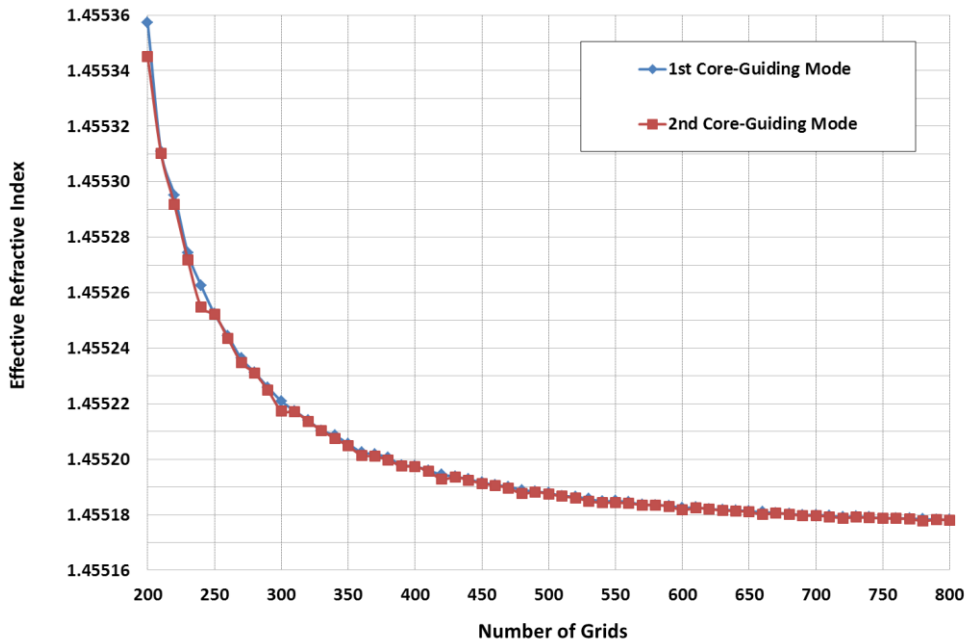


**Figure 5-29: Convergence curves of the PLCF sample with respect to the number of grids calculated with vector-field FDFD**

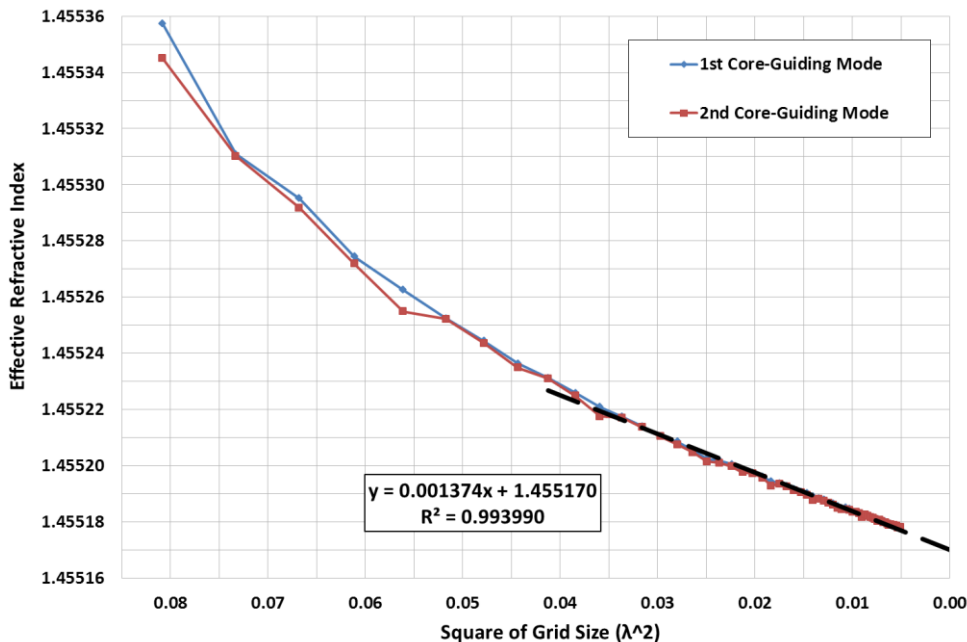


**Figure 5-30: Convergence curve of the PLCF sample with respect to the square of grid size calculated with vector-field FDFD**

## 5.9 Discussions and Numerical Study of PLCF

In this section we like to discuss some possible properties of PLCF observed in numerical simulations.

### 5.9.1 Polarization and Birefringence

With vector-field FDFD, we can easily obtain  $n_{eff}$  in two orthogonal polarization states, and this in turn gives us information on the birefringence and polarization mode dispersion of the fiber. Also, for some configurations, hybrid guiding (index-guiding in one polarization and PBG-guiding in the other) has been reported ([Sun and Chan, 2007](#); [Zograopoulos and Kriegis, 2009](#)) and with the vector-field FDFD, it may also be possible to observe the hybrid guiding mechanism.

### 5.9.2 Rotation of Liquid Crystals in the Transverse Plane of the PLCF

As discussed in [Chapter 4](#), the vector-field FDFD we implemented is able to take into account transverse anisotropies. In the context of the thesis so far, we have not taken advantage of this functionality. Instead, we have spent more effort on validating the accuracy and effectiveness of the implemented FDFDs. Some previous reports have shown the significant tunability of PLCFs with external electric field ([Ertman et al., 2009](#)). Provided that we can align the liquid crystal molecules within the PLCF from the planar configuration ([Figure 5-4a](#)) to the transverse configuration ([Figure 5-4b](#)), it can be an interesting aspect to observe the effects of the rotation of LC molecules in the transverse plane. The vector-field FDFD we have implemented is able to simulate this kind of configurations of LC.

## 6 Conclusions and Outlook

In this thesis we have shown that, based on two curl Maxwell equations with finite difference approximation, together with Yee's staggered mesh, the photonic bandgap guiding mechanism was observed in addition to the index-guiding mechanism for light propagation in photonic liquid crystal fibers.

The scalar-field FDFD implemented is based on direct 2<sup>nd</sup> order finite differences in space, and is capable of characterizing relatively simple fiber geometries with fairly accurate results. However, we have shown both theoretically and numerically, qualitatively and quantitatively, the limit of the scalar-field formulation by comparison with known analytical values. On the other hand, the vector-field FDFD implemented is based on 1<sup>st</sup> order finite differences with matrix multiplication, and is capable to deal with more complicated fiber geometries. Nevertheless, the size of the eigenvalue problem increases largely as the vector nature of fields is considered, and therefore demands significant computational effort.

We implemented the vector-field FDFD first proposed by [Zhu and Brown, 2002](#), and extended the formulation to include transverse anisotropies. Although through the context of this thesis we have not really used such additional feature, but as long as we have verified the vector-field FDFD, it can lead to interesting aspects of the dynamic studies of PLCFs.

Despite the insufficiency on computational power and time, we have tried to compare the numerical results with experimental results. Gaps in the transmission spectrum are observed both experimentally and numerically. The discrepancy might have arisen from both the experimental and the numerical aspects. Our preliminary observation regarding the simulation on PLCFs shows that lack of computational resolution might have led to inaccuracies and errors. On the other hand, the experimental results also have to be validated, particularly the molecular arrangement of the liquid crystal inside the host PCF.

Although the comparison was carried out in a more qualitative way, it nevertheless showed that the effectiveness of the implemented vector-field FDFD scheme. It brought excitement, together with more challenges. We have noted that spurious modes appeared to be an interesting issue to be understood, but owing to lack of time and knowledge, we have only tried a very primitive way to solve the issue, that is to cut away

the higher-refractive region outside the photonic crystal cladding. Some improvements are gained, but still a lot more are to be pursued.

Now that we have assessed and verified the applicability of FDFDs, the vector-field formulation in particular, to model light propagation in PLCFs, the next possible stage of work shall be dedicated to comprehensive and rigorous study of numerical results regarding PLCF geometries with various computational setups. In this way, more information can be obtained for further orientation on possible improvements regarding the FDFD schemes. On the experimental side, more precise control over the LC molecular configuration and higher quality on the manufacture of PCFs will give more valuable information on verification and benchmarking of the numerical schemes. By progressing these two aspects of future work, it can be foreseen that in the near future PLCFs can find potential applications in the field of optics with numerical design tools that greatly facilitate the manufacturing process.

One part of the objective of the thesis is accessibility and efficiency. In the thesis this has not been discussed explicitly. If some words are to fall on these two aspects, ‘unsatisfactory but acceptable’ shall be close. The major simulations were performed on a normal laptop. The resolution of the simulation was mostly limited by the software limit than the hardware limit. As for the time consumed, depending on the number of eigenvalues to be sought, the simulation itself for one single wavelength with highest available resolution takes between **5** to **10** minutes with **Computer 1** in **Appendix D**. Exporting the results into figures also consumes quite unexpected amount of time. The time for simulations for wavelengths over a spectral range depends on the spectral resolution. An overnight run is normally required for **1nm** spectral resolution.

This thesis sets its focus on finite difference methods in frequency domain. However, we have always kept in mind the possible usefulness of beam propagation methods in the study of PLCFs. It can be interesting to combine and compare the FDFDs and the BPMs. Even if we limit ourselves first to FDFDs, there are still a lot more aspects can be further considered in the simulation for PLCFs. For example, the order parameter which accounts for the molecular arrangement of liquid crystal, especially when we want to study the temperature dependent behaviors of PLCFs.

Last, we like to mention the aspects in view of computer science. Throughout the thesis we have tried to set up everything from scratch. We derived from theory the master equations for FDFD simulations and implemented the code library in **MATLAB**. However, one thing that we did not step into was the eigen solver. We have only fundamental

knowledge regarding the `eigs` function, which ports in the Arnoldi routine for sparse matrix eigen problems. Since the simulations for PLCFs have been shown to be demanding, the performance of the FDFD schemes may be improved largely through the study of more efficient algorithms, implementations, and parallel computing architectures.

## Appendix A

The implementation including both scalar-field and vector-field FDFDs consists of the following functions written as MATLAB® m-files:

### 1) eigensolve

```
% Eigen Solver: eigs, MATLAB interface with ARPACK, Arnoldi Package
% Recast Eigen Vectors into Eigen Fields
%
% Output
% FF(x, y, eigen index, field index): full eigen field matrix
% eig_value: eigen values
% flag_conv: if the eigenvalues are converged, see MATLAB help eigs
%
% Input
% MM: global matrix to be solved
% n_ev: number of eigen values desired
% mx, ny: calculation window dimensions
% n_fields: number of fields that are coupled in the global matrix
%
% Example
%
% P |Ex| = beta^2 |Ex| --> n_field = 2
% |Ey| |Ey| (P = global matrix, eig_value = beta^2)
%
% R |Ex| = beta |Ex| --> n_field = 4
% |Ey| |Ey| (R = global matrix, eig_value = beta)
% |Hx| |Hx|
% |Hy| |Hy|
%
function [FF, eig_value, flag_conv] = eigensolve(MM, n_ev, guess, mx, ny, n_fields)
nm = ny*mx;
options.tol = 1e-7; options.disp = 0; options.isreal = isreal(MM);
[eig_vector, eig_value, flag_conv] = eigs(MM, speye(size(MM)), n_ev, guess, options);
FF = zeros(ny, mx, n_ev, n_fields);
for ii = 1:1:n_ev
    FF_all = reshape(eig_vector(:,ii), nm, n_fields);
    for jj = 1:1:n_fields
        FF(:, :, ii, jj) = reshape(FF_all(:, jj), mx, ny)';
    end
end
end
```

### 2) epr\_nlc.m

```
function [epr_lc_xx, epr_lc_xy, epr_lc_xz, epr_lc_yx, epr_lc_yy, epr_lc_yz, epr_lc_zx,
epr_lc_zy, epr_lc_zz] = epr_nlc(no, ne, theta, phi)
delta = ne.^2-no.^2;
epr_lc_xx = no.^2 + delta.*sin(theta).^2.*cos(phi).^2;
epr_lc_yy = no.^2 + delta.*sin(theta).^2.*sin(phi).^2;
epr_lc_zz = no.^2 + delta.*cos(theta).^2;
epr_lc_xy = delta.*sin(theta).^2.*sin(phi).*cos(phi);
epr_lc_yx = epr_lc_xy;
epr_lc_xz = delta.*sin(theta).*cos(theta).*cos(phi);
epr_lc_zx = epr_lc_xz;
epr_lc_yz = delta.*sin(theta).*cos(theta).*sin(phi);
epr_lc_zy = epr_lc_yz;
end
```

### 3) finite\_diff.m

```
% Finite difference according to Yee mesh and BCs
%
```

```
% bc_e, bc_h: 0 for zero boundary condition (Dirichlet)
%           1 for Neumann boundary condition on x-boundary (d/dx = 0)
%           2 for Neumann boundary condition on y-boundary (d/dy = 0)
%           3 for Neumann boundary condition on x- and y- boundaries
%
% e for electric field, h for magnetic field

function [Ux, Uy, Vx, Vy] = finite_diff(mx, ny, dx, dy, bc_e, bc_h)
    nm = ny*mx;
    K1_e1 = 1:1:nm; L1_e1 = 1:1:nm; D1_e1 = ones(1,nm);
    K1_e2 = 1:1:nm; L1_e2 = 1:1:nm; D1_e2 = ones(1,nm);
    K1_e3 = 1:1:nm-1; L1_e3 = 2:1:nm;
    K1_e3t= ones(ny,1); L1_e3t = ones(1,mx); L1_e3t(end) = 0;
    D1_e3 = reshape((K1_e3t*L1_e3t)',1,nm); D1_e3 = D1_e3(1:end-1);
    K1_e4 = 1:1:nm-mx; L1_e4 = mx+1:1:nm; D1_e4 = ones(1,nm-mx);
    K1_h1 = 1:1:nm; L1_h1 = 1:1:nm; D1_h1 = ones(1,nm);
    K1_h2 = 1:1:nm; L1_h2 = 1:1:nm; D1_h2 = ones(1,nm);
    K1_h3 = 2:1:nm; L1_h3 = 1:1:nm-1; D1_h3 = D1_e3;
    K1_h4 = 1+mx:1:nm; L1_h4 = 1:1:nm-mx; D1_h4 = ones(1,nm-mx);
    if (bc_e == 1)
        D1_e1(mx:mx:nm) = 0;
    elseif (bc_e == 2)
        D1_e2(nm-mx+1:nm) = 0;
    elseif (bc_e == 3)
        D1_e1(mx:mx:nm) = 0; D1_e2(nm-mx+1:nm) = 0;
    end
    if (bc_h == 1)
        D1_h1(1:mx:nm-mx+1) = 0;
    elseif (bc_h == 2)
        D1_h2(1:mx) = 0;
    elseif (bc_h == 3)
        D1_h1(1:mx:nm-mx+1) = 0; D1_h2(1:mx) = 0;
    end
    Ux = (1/dx)*sparse([K1_e1 K1_e3], [L1_e1 L1_e3], [-1.*D1_e1 D1_e3]);
    Uy = (1/dx)*sparse([K1_e2 K1_e4], [L1_e2 L1_e4], [-1.*D1_e2 D1_e4]);
    Vx = (1/dy)*sparse([K1_h1 K1_h3], [L1_h1 L1_h3], [D1_h1 -1.*D1_h3]);
    Vy = (1/dy)*sparse([K1_h2 K1_h4], [L1_h2 L1_h4], [D1_h2 -1.*D1_h4]);
end
```

## 4) geometry\_{SIF | HoF | HoF3}.m

```
function Epri = geometry_SIF(mx, dx, ny, dy, epr_1, epr_2, r_core, ia_factor, padding)
    if (ia_factor == 1)
        X1 = -mx/2:1:mx/2-1; X1 = X1.*dx;
        Y1 = -ny/2:1:ny/2-1; Y1 = Y1.*dy;
        [X2,Y2] = meshgrid(X1,Y1);
        Epri = ones(ny,mx).*epr_2;
        Epri((X2.^2+Y2.^2)<=r_core^2) = epr_1;
    elseif (ia_factor > 1)
        % Interpolation
        mxi = (mx+padding.*2).*ia_factor;
        nyi = (ny+padding.*2).*ia_factor;
        dxi = dx./ia_factor;
        dyi = dy./ia_factor;
        X1i = -mxi/2:1:mxi/2-1; X1i = X1i.*dxi;
        Y1i = -nyi/2:1:nyi/2-1; Y1i = Y1i.*dyi;
        [X2i,Y2i] = meshgrid(X1i,Y1i);
        Epri = ones(nyi,mxi).*epr_2;
        Epri((X2i.^2+Y2i.^2)<=r_core^2) = epr_1;
    end
end

% Generate hexagonal Holey Optical Fiber (HoF) geometry with given
% parameters
%
% mx dx ny dy: number-of-grids and grid-size
% epr_h: relative permittivity of the host material (e.g. silica)
% epr_g: relative permittivity of the guest (hole) material (e.g. air)
% ia_factor: interpolation factor
% padding: in order to perform index-averaging on the border, additional
%         padding is required in the interpolation.
%         For general purposes, set padding = 2. However, for specific
```

```

% index-averaging schemes, padding = 1 is enough.

function Epri = geometry_HoF(mx, dx, ny, dy, epr_h, epr_g, pitch, r_air, ia_factor, padding)
    border = ceil(mx*dx/pitch/2)+2; border = border+mod(border,2);
    hp = pitch/2;
    if (ia_factor == 1)
        X1 = -mx/2:1:mx/2-1; X1 = X1.*dx;
        Y1 = -ny/2:1:ny/2-1; Y1 = Y1.*dy;
        [X2,Y2] = meshgrid(X1,Y1);
        Epri = ones(ny,mx).*epr_h;
        for jj = -border:2:border
            for ii = -border:2:border
                if (ii~=0 || jj~=0)
                    Epri(((X2-hp*ii).^2+(Y2-hp*sqrt(3)*jj).^2)<=r_air^2) = epr_g;
                end
            end
        end
        for jj = -border-1:2:border+1
            for ii = -border-1:2:border+1
                Epri(((X2-hp*ii).^2+(Y2-hp*sqrt(3)*jj).^2)<=r_air^2) = epr_g;
            end
        end
    elseif (ia_factor > 1)
        mx_i = (mx+padding.*2).*ia_factor;
        ny_i = (ny+padding.*2).*ia_factor;
        dx_i = dx./ia_factor;
        dy_i = dy./ia_factor;
        X1_i = -mx_i/2:1:mx_i/2-1; X1_i = X1_i.*dx_i;
        Y1_i = -ny_i/2:1:ny_i/2-1; Y1_i = Y1_i.*dy_i;
        [X2_i,Y2_i] = meshgrid(X1_i,Y1_i);
        Epri = ones(ny_i,mx_i).*epr_h;
        for jj = -border:2:border
            for ii = -border:2:border
                if (ii~=0 || jj~=0)
                    Epri(((X2_i-hp*ii).^2+(Y2_i-hp*sqrt(3)*jj).^2)<=r_air^2) = epr_g;
                end
            end
        end
        for jj = -border-1:2:border+1
            for ii = -border-1:2:border+1
                Epri(((X2_i-hp*ii).^2+(Y2_i-hp*sqrt(3)*jj).^2)<=r_air^2) = epr_g;
            end
        end
    end
end

function Epri = geometry_HoF3(mx, dx, ny, dy, epr_h, epr_g, pitch, r_air, ia_factor, padding)
% border = ceil(mx*dx/pitch/2)+2; border = border+mod(border,2);
    border = 6;
    hp = pitch/2;
    if (ia_factor == 1)
        X1 = -mx/2:1:mx/2-1; X1 = X1.*dx;
        Y1 = -ny/2:1:ny/2-1; Y1 = Y1.*dy;
        [X2,Y2] = meshgrid(X1,Y1);
        Epri = ones(ny,mx).*epr_h;
        Epri(abs(X2)>3.5*pitch|abs(Y2)>3.5*pitch*0.866) = 1;
        Epri(abs(Y2)>(-1.*sqrt(3).*((X2-3.5.*pitch)))) = 1;
        Epri(abs(Y2)>((1.*sqrt(3).*((X2+3.5.*pitch)))) = 1;
        for jj = -border+4:2:border-4
            for ii = -(border-abs(jj)):2:(border-abs(jj))
                if (ii~=0 || jj~=0)
                    Epri(((X2-hp*ii).^2+(Y2-hp*sqrt(3)*jj).^2)<=r_air^2) = epr_g;
                end
            end
        end
        for jj = -border+3:2:border-3
            for ii = -(border-abs(jj)):2:(border-abs(jj))
                Epri(((X2-hp*ii).^2+(Y2-hp*sqrt(3)*jj).^2)<=r_air^2) = epr_g;
            end
        end
    elseif (ia_factor > 1)
        mx_i = (mx+padding.*2).*ia_factor;
        ny_i = (ny+padding.*2).*ia_factor;

```

```

dxi = dx./ia_factor;
dyi = dy./ia_factor;
X1i = -mxi/2:1:mxi/2-1; X1i = X1i.*dxi;
Y1i = -nyi/2:1:nyi/2-1; Y1i = Y1i.*dyi;
[X2i,Y2i] = meshgrid(X1i,Y1i);
Epri = ones(nyi,mxi).*epr_h;
Epri(abs(X2i)>3.5*pitch|abs(Y2i)>3.5*pitch*0.866) = 1;
Epri(abs(Y2i)>(-1.*sqrt(3).*(X2i-3.5.*pitch))) = 1;
Epri(abs(Y2i)>( 1.*sqrt(3).*(X2i+3.5.*pitch))) = 1;
for jj = -border+4:2:border-4
    for ii = -(border-abs(jj)):2:(border-abs(jj))
        if (ii~=0 || jj~=0)
            Epri(((X2i-hp*ii).^2+(Y2i-hp*sqrt(3)*jj).^2)<=r_air^2) = epr_g;
        end
    end
end
for jj = -border+3:2:border-3
    for ii = -(border-abs(jj)):2:(border-abs(jj))
        Epri(((X2i-hp*ii).^2+(Y2i-hp*sqrt(3)*jj).^2)<=r_air^2) = epr_g;
    end
end
end
end

```

## 5) index\_avg.m

```

% Perform index averaging according to specified mesh configuration
%
% Epr_in: input permittivity map
% mx, ny: output size of the permittivity map
% ia_factor: interpolation factor
% padding: in order to perform index-averaging on the border, additional
%           padding is required in the interpolation.
%           For general purposes, set padding = 2. However, for specific
%           index-averaging schemes, padding = 1 is enough.
% pos_x, pos_y: relative positions in the mesh configuration
%
% Examples with a common Yee's staggered mesh
%


|          |          |                |
|----------|----------|----------------|
| Dy,Ey,Hx | Hx       | Erxx Erxy Erxz |
| Ez       | Dx,Ex,Hy | Erxy Eryy Eryz |
|          |          | Erzx Erzy Erzz |


%
% eps_x: relative permittivities Erxx, Erxy, Erxz
% eps_y: relative permittivities Eryx, Eryy, Eryz
% eps_z: relative permittivities Erzx, Erzy, Erzz
%
% 1) If we attach eps_z(k,l) to Ez with (pos_x, pos_y) = (0,0)
% Then
%   eps_x(k,l), attached to Dx/Ex, will have (pos_x, pos_y) = (1,0)
%   eps_y(k,l), attached to Dy/Ey, will have (pos_x, pos_y) = (0,1)
%
% 2) If we attach eps_z(k,l) to Hz with (pos_x, pos_y) = (0,0)
% Then
%   eps_x(k,l), attached to Dx/Ex, will have (pos_x, pos_y) = (0,-1)
%   eps_y(k,l), attached to Dy/Ey, will have (pos_x, pos_y) = (-1,0)
%
function Epr_out = index_avg(Epr_in, mx, ny, ia_factor, padding, pos_x, pos_y)
if (ia_factor==1)
    Epr_out = Epr_in;
elseif (ia_factor>1)
    Epr_out = zeros(ny,mx);
    hf = ia_factor/2;
    for iy = 1:1:ny;
        for ix = 1:1:mx;
            ya = (iy+padding)*ia_factor + 1 - hf;
            yb = (iy+padding)*ia_factor + 1 + hf;
            xa = (ix+padding)*ia_factor + 1 - hf;
            xb = (ix+padding)*ia_factor + 1 + hf;

```

```

Epr_out(iy,ix) = ...
sum(sum(Epr_in(ya+hf*pos_y:yb+hf*pos_y,xa+hf*pos_x:xb+hf*pos_x))) ...
./ (2.*hf+1)^2;
end
end
end
end

```

## 6) n6CHBT\_v3 {e20 | e30 | o20 | o 30} .m

```

function n = n6CHBT_v3e20(lambda)
lambda_nm0 = 156.7;
lambda_nm = lambda.*1000;
G = 2.569;
n = 1 + G.*1e-5.*lambda_nm.^2.*lambda_nm0.^2 ...
./((lambda_nm.^2-lambda_nm0.^2));
end

function n = n6CHBT_v3e30(lambda)
lambda_nm0 = 154.6;
lambda_nm = lambda.*1000;
G = 2.584;
n = 1 + (G.*1e-5.*lambda_nm.^2).*(lambda_nm0.^2) ...
./((lambda_nm.^2-lambda_nm0.^2));
end

function n = n6CHBT_v3o20(lambda)
lambda_nm0 = 125.8;
lambda_nm = lambda.*1000;
G = 3.147;
n = 1 + G.*1e-5.*lambda_nm.^2.*lambda_nm0.^2 ...
./((lambda_nm.^2-lambda_nm0.^2));
end

function n = n6CHBT_v3o30(lambda)
lambda_nm0 = 126.8;
lambda_nm = lambda.*1000;
G = 3.099;
n = 1 + G.*1e-5.*lambda_nm.^2.*lambda_nm0.^2 ...
./((lambda_nm.^2-lambda_nm0.^2));
end

```

## 7) nSilica {20 | 25 | 29 | 34 | 40} .m

```

function n = nSilica20(lambda)
A = 1.311382;
B = 0.794229;
C = 0.010951;
D = 0.999525;
E = 100;
n2 = B.*(lambda.^2)./(lambda.^2-C);
n3 = D.*(lambda.^2)./(lambda.^2-E);
n = sqrt(A + n2 + n3);
end

function n = nSilica25(lambda)
A = 1.309557;
B = 0.796189;
C = 0.010936;
D = 0.986365;
E = 100;
n2 = B.*(lambda.^2)./(lambda.^2-C);
n3 = D.*(lambda.^2)./(lambda.^2-E);
n = sqrt(A + n2 + n3);
end

```

```

function n = nSilica29(lambda)
A = 1.308097;
B = 0.797703;
C = 0.010924;
D = 0.975837;
E = 100;
n2 = B.*lambda.^2./(lambda.^2-C);
n3 = D.*lambda.^2./(lambda.^2-E);
n = sqrt(A + n2 + n3);
end

function n = nSilica34(lambda)
A = 1.306272;
B = 0.799595;
C = 0.010909;
D = 0.962676;
E = 100;
n2 = B.*lambda.^2./(lambda.^2-C);
n3 = D.*lambda.^2./(lambda.^2-E);
n = sqrt(A + n2 + n3);
end

function n = nSilica40(lambda)
A = 1.304082;
B = 0.801867;
C = 0.010891;
D = 0.946884;
E = 100;
n2 = B.*lambda.^2./(lambda.^2-C);
n3 = D.*lambda.^2./(lambda.^2-E);
n = sqrt(A + n2 + n3);
end

```

## 8) nSi02.m

```

function n = nSi02(lambda)
a1 = 0.6961663;
a2 = 0.4079426;
a3 = 0.8974794;
b1 = 0.0864043;
b2 = 0.1162414;
b3 = 9.896161;
n1 = a1.*lambda.^2./(lambda.^2-b1.^2);
n2 = a2.*lambda.^2./(lambda.^2-b2.^2);
n3 = a3.*lambda.^2./(lambda.^2-b3.^2);
n = sqrt(1 + n1 + n2 + n3);
end

```

## 9) plot\_field.m

```

% Plot nine eigen fields: 1+offset to 9+offset

function plot_field(fig, X1, Y1, field, row, col, offset)
figure(fig);
set(gcf, 'Renderer', 'zbuffer');
for ii = 1:1:row*col
    subplot(row,col,ii);
    set(gca, 'FontSize', 6);
    surf(X1,Y1,field(:,:,ii+offset));
    grid off;
    axis equal; shading flat, view([0 0 1]);
    set(colorbar, 'FontSize', 6);
    xlim([min(X1) max(X1)]), ylim([min(Y1) max(Y1)]);
end
end

```

## 10) plot\_field\_png.m

```

function plot_field_png(pngfile, X1, Y1, field, row, col, offset)
h = gcf;
set(h, 'Renderer', 'zbuffer');
set(h, 'PaperPositionMode', 'auto');
% set(h, 'PaperPositionMode', 'manual');
% set(h, 'PaperPosition', [100 100 12000 6000]);
% set(h, 'Units', 'points');
% set(h, 'PaperUnits', 'points');
% set(h, 'PaperSize', [12200 6200]);

for ii = 1:1:row*col
    subplot(row,col,ii);
    set(gca, 'FontSize', 6);
    surf(X1,Y1,field(:,:,ii+offset));
    axis equal; colorbar, shading flat, view([0 0 1]);
    set(colorbar, 'FontSize', 6);
    xlim([min(X1) max(X1)]), ylim([min(Y1) max(Y1)]);
end
% print(h, '-zbuffer', '-dpng', '-r900', pngfile);
% print(h, '-zbuffer', '-dpng', '-r600', pngfile);
print(h, '-zbuffer', '-dpng', '-r300', pngfile);
% close(h);
end

```

## 11) plot\_geometry.m

```

% Plots permittivity geometry to the assigned figure
%
% | Erxx Erxy Erxz |
% | Erxy Eryy Eryz |
% | Erzx Erzy Erzz |

function plot_geometry(fig , X1, Y1, Epr_xx, Epr_xy, Epr_xz, Epr_yx, Epr_yy, Epr_yz, Epr_zx,
Epr_zy, Epr_zz)
figure(fig);
h = gcf;
set(h, 'Renderer', 'zbuffer');

subplot(3,3,1);
surf(X1,Y1,(Epr_xx)), colorbar, shading flat, view([0 0 1]);
title('xx'); xlabel('x (micron)'); ylabel('y (micron)');
axis equal; xlim([min(X1) max(X1)]), ylim([min(Y1) max(Y1)]);

subplot(3,3,2);
surf(X1,Y1,(Epr_xy)), colorbar, shading flat, view([0 0 1]);
title('xy'); xlabel('x (micron)'); ylabel('y (micron)');
axis equal; xlim([min(X1) max(X1)]), ylim([min(Y1) max(Y1)]);

subplot(3,3,3);
surf(X1,Y1,(Epr_xz)), colorbar, shading flat, view([0 0 1]);
title('xz'); xlabel('x (micron)'); ylabel('y (micron)');
axis equal; xlim([min(X1) max(X1)]), ylim([min(Y1) max(Y1)]);

subplot(3,3,4);
surf(X1,Y1,(Epr_yx)), colorbar, shading flat, view([0 0 1]);
title('yx'); xlabel('x (micron)'); ylabel('y (micron)');
axis equal; xlim([min(X1) max(X1)]), ylim([min(Y1) max(Y1)]);

subplot(3,3,5);
surf(X1,Y1,(Epr_yy)), colorbar, shading flat, view([0 0 1]);
title('yy'); xlabel('x (micron)'); ylabel('y (micron)');
axis equal; xlim([min(X1) max(X1)]), ylim([min(Y1) max(Y1)]);

subplot(3,3,6);
surf(X1,Y1,(Epr_yz)), colorbar, shading flat, view([0 0 1]);
title('yz'); xlabel('x (micron)'); ylabel('y (micron)');

```

```

axis equal; xlim([min(X1) max(X1)]), ylim([min(Y1) max(Y1)]);

subplot(3,3,7);
surf(X1,Y1,(Epr_zx)), colorbar, shading flat, view([0 0 1]);
title('zx'); xlabel('x (micron)'); ylabel('y (micron)');
axis equal; xlim([min(X1) max(X1)]), ylim([min(Y1) max(Y1)]);

subplot(3,3,8);
surf(X1,Y1,(Epr_zy)), colorbar, shading flat, view([0 0 1]);
title('zy'); xlabel('x (micron)'); ylabel('y (micron)');
axis equal; xlim([min(X1) max(X1)]), ylim([min(Y1) max(Y1)]);

subplot(3,3,9);
surf(X1,Y1,(Epr_zz)), colorbar, shading flat, view([0 0 1]);
title('zz'); xlabel('x (micron)'); ylabel('y (micron)');
axis equal; xlim([min(X1) max(X1)]), ylim([min(Y1) max(Y1)]);

end

```

## 12) sFDFD.m

```

% Scalar-Field Finite-Difference Frequency Domain
% 3-term FD

function M = sFDFD(lambda, mx, ny, dx, dy, Er2)
c0 = 299792458e6; % speed of light (um)
w_ang = 2.*pi.*c0./lambda; % angular frequency

nm = ny*mx;
K1_a = 1:1:nm; L1_a = 1:1:nm;
D1_a = ones(ny,mx);
D1_a = D1_a.*((-2/dx.^2) + (-2/dy.^2) + (Er2.*w_ang.^2./c0.^2));
D1_a = reshape(D1_a',1,nm);

K1_b = 1:1:nm-1; L1_b = 2:1:nm;
K1_bt = ones(ny,1); L1_bt = ones(1,mx); L1_bt(end) = 0;
D1_b = reshape((K1_bt*L1_bt)', 1 , nm); D1_b = D1_b(1:end-1);

K1_c = 1:1:nm-mx; L1_c = mx+1:1:nm;
D1_c = ones(1,nm-mx);

M = sparse([K1_a K1_b K1_b+1 K1_c K1_c+mx], ...
           [L1_a L1_b L1_b-1 L1_c L1_c-mx], ...
           [D1_a D1_b./dx.^2 D1_b./dx.^2 D1_c./dy.^2 D1_c./dy.^2]);
end

```

## 13) vFDFD {dP | dQ} .m

```

% Vector-Field Finite-Difference Frequency Domain
% Assembly of the Global Matrix
% Only diagonal anisotropies are taken into account
%
%   | Erxx   0   0 |
% D = | 0   Eryy   0 |
%   | 0   0   Erzz |
%
% P |Ex| = beta^2 |Ex|
% |Ey| |Ey|
%

function P = vFDFDdP(lambda, mx, ny, Ux, Uy, Vx, Vy, Epr_xx, Epr_yy, Epr_zz, Epr_xy, Epr_yx)
nm = ny*mx; k0 = 2*pi/lambda; I2 = speye(nm,nm); K1_a = 1:1:nm;
Erx = sparse(K1_a, K1_a, reshape(Epr_xx',1,nm));
Ery = sparse(K1_a, K1_a, reshape(Epr_yy',1,nm));
Erz = sparse(K1_a, K1_a, reshape(Epr_zz',1,nm));
% Erxy = sparse(K1_a, K1_a, reshape(Epr_xy',1,nm));
% Eryx = sparse(K1_a, K1_a, reshape(Epr_yx',1,nm));
Pxx = (-k0^2)*Ux*(I2/Erz)*Vy*Vx*Uy ...
      + (k0^2*I2+Ux*(I2/Erz)*Vx)*(Erz+k0^2-Vy*Uy);
Pxy = Ux*(I2/Erz)*Vy*(Ery+k0^2-Vx*Ux) ...

```

```

        - k0^-2*(k0^2*I2+Ux*(I2/Erz)*Vx)*Vy*Ux;
Pyy = (-k0^-2)*Uy*(I2/Erz)*Vx*Vy*Ux ...
      + (k0^2*I2+Uy*(I2/Erz)*Vy)*(Ery+k0^-2*Vx*Ux);
Pyx = Uy*(I2/Erz)*Vx*(Erz+k0^-2*Vy*Uy) ...
      - k0^-2*(k0^2*I2+Uy*(I2/Erz)*Vy)*Vx*Uy;
P_1 = cat(2,Pxx,Pxy);
P_2 = cat(2,Pyx,Pyy);
P = cat(1,P_1,P_2);
end

% Vector-Field Finite-Difference Frequency Domain
% Assembly of the Global Matrix
% Only diagonal anisotropies are taken into account
%
% D = | Erxx   0   0 |
%      | 0   Eryy   0 |
%      | 0   0   Erzz |
%
% Q |Hx| = beta^2 |Hx|
% |Hy|           |Hy|
%

function Q = vFDFDdQ(lambda, mx, ny, Ux, Uy, Vx, Vy, Epr_xx, Epr_yy, Epr_zz, Epr_xy, Epr_yx)
nm = ny*mx; k0 = 2*pi/lambda; I2 = speye(nm,nm); K1_a = 1:1:nm;
Erx = sparse(K1_a, K1_a, reshape(Epr_xx',1,nm));
Ery = sparse(K1_a, K1_a, reshape(Epr_yy',1,nm));
Erz = sparse(K1_a, K1_a, reshape(Epr_zz',1,nm));
% Erxy = sparse(K1_a, K1_a, reshape(Epr_xy',1,nm));
% Eryx = sparse(K1_a, K1_a, reshape(Epr_yx',1,nm));
Qxx = (-k0^-2)*Vx*Uy*Ux*(I2/Erz)*Vy ...
      + (Ery+k0^-2*Vx*Ux)*(k0^2*I2+Uy*(I2/Erz)*Vx);
Qxy = -(Ery+k0^-2*Vx*Ux)*Uy*(I2/Erz)*Vx ...
      + k0^-2*Vx*Uy*(k0^2*I2+Ux*(I2/Erz)*Vx);
Qyy = (-k0^-2)*Vy*Ux*Uy*(I2/Erz)*Vx ...
      + (Erz+k0^-2*Vy*Uy)*(k0^2*I2+Ux*(I2/Erz)*Vx);
Qyx = -(Erz+k0^-2*Vy*Uy)*Ux*(I2/Erz)*Vy ...
      + k0^-2*Vy*Ux*(k0^2*I2+Uy*(I2/Erz)*Vy);
Q_1 = cat(2,Qxx,Qxy);
Q_2 = cat(2,Qyx,Qyy);
Q = cat(1,Q_1,Q_2);
end

```

## 14) vFDFD {tP | tQ} .m

```

% Vector-Field Finite-Difference Frequency Domain
% Assembly of the Global Matrix
% Only diagonal and transverse anisotropies are taken into account
%
% D = | Erxx   Erxy   0 |
%      | Erxy   Eryy   0 |
%      | 0       0       Erzz |
%
% P |Ex| = beta^2 |Ex|
% |Ey|           |Ey|
%

function P = vFDFDtP(lambda, mx, ny, Ux, Uy, Vx, Vy, Epr_xx, Epr_yy, Epr_zz, Epr_xy, Epr_yx)
nm = ny*mx; k0 = 2*pi/lambda; I2 = speye(nm,nm); K1_a = 1:1:nm;
Erx = sparse(K1_a, K1_a, reshape(Epr_xx',1,nm));
Ery = sparse(K1_a, K1_a, reshape(Epr_yy',1,nm));
Erz = sparse(K1_a, K1_a, reshape(Epr_zz',1,nm));
Erxy = sparse(K1_a, K1_a, reshape(Epr_xy',1,nm));
Eryx = sparse(K1_a, K1_a, reshape(Epr_yx',1,nm));
Pxx = (-k0^-2)*Ux*(I2/Erz)*Vy*Vx*Uy ...
      + (k0^2*I2+Ux*(I2/Erz)*Vx)*(Erz+k0^-2*Vy*Uy) ...
      + Ux*(I2/Erz)*Vy*Eryx;
Pxy = Ux*(I2/Erz)*Vy*(Ery+k0^-2*Vx*Ux) ...
      - k0^-2*(k0^2*I2+Ux*(I2/Erz)*Vx)*Vy*Ux ...
      + k0^2*Erxy + Ux*(I2/Erz)*Vx*Eryx;
Pyy = (-k0^-2)*Uy*(I2/Erz)*Vx*Vy*Ux ...
      + (k0^2*I2+Uy*(I2/Erz)*Vy)*(Ery+k0^-2*Vx*Ux) ...
      + Uy*(I2/Erz)*Vx*Eryx;

```

```

Pyx = Uy*(I2/Erz)*Vx*(Erz+k0^-2*Vy*Uy) ...
    - k0^-2*(k0^2*I2+Uy*(I2/Erz)*Vy)*Vx*Uy ...
    - k0^2*Eryx + Uy*(I2/Erz)*Vy*Eryx;
P_1 = cat(2,Pxx,Pxy);
P_2 = cat(2,Pyx,Pyy);
P = cat(1,P_1,P_2);
end

% Vector-Field Finite-Difference Frequency Domain
% Assembly of the Global Matrix
% Only diagonal and transverse anisotropies are taken into account
%
% D = | Erxx   Eryx   0 |
%      | Eryx   Eryy   0 |
%      | 0       0     Erzz |
%
% Q |Hx| = beta^2 |Hx|
% |Hy|           |Hy|
%

function Q = vFDFDtQ(lambda, mx, ny, Ux, Uy, Vx, Vy, Epr_xx, Epr_yy, Epr_zz, Epr_xy, Epr_yx)
nm = ny*mx; k0 = 2*pi/lambda; I2 = speye(nm,nm); K1_a = 1:1:nm;
Erz = sparse(K1_a, K1_a, reshape(Epr_xx',1,nm));
Ery = sparse(K1_a, K1_a, reshape(Epr_yy',1,nm));
Erz = sparse(K1_a, K1_a, reshape(Epr_zz',1,nm));
Erx = sparse(K1_a, K1_a, reshape(Epr_xy',1,nm));
Eryx = sparse(K1_a, K1_a, reshape(Epr_yx',1,nm));
Qxx = (-k0^-2)*Vx*Uy*Ux*(I2/Erz)*Vy ...
    + (Ery+k0^-2*Vx*Ux)*(k0^2*I2+Uy*(I2/Erz)*Vy) ...
    + Eryx*Ux*(I2/Erz)*Vy;
Qxy = -(Ery+k0^-2*Vx*Ux)*Uy*(I2/Erz)*Vx ...
    + k0^-2*Vx*Uy*(k0^2*I2+Ux*(I2/Erz)*Vx) ...
    - k0^2*Eryx - Eryx*Ux*(I2/Erz)*Vx;
Qyy = (-k0^-2)*Vy*Ux*Uy*(I2/Erz)*Vx ...
    + (Erz+k0^-2*Vy*Uy)*(k0^2*I2+Ux*(I2/Erz)*Vx) ...
    + Ery*Uy*(I2/Erz)*Vx;
Qyx = -(Erz+k0^-2*Vy*Uy)*Ux*(I2/Erz)*Vy ...
    + k0^-2*Vy*Ux*(k0^2*I2+Uy*(I2/Erz)*Vy) ...
    - k0^2*Eryx - Eryx*Uy*(I2/Erz)*Vy;
Q_1 = cat(2,Qxx,Qxy);
Q_2 = cat(2,Qyx,Qyy);
Q = cat(1,Q_1,Q_2);
end

```

## Appendix B

<http://www.photonics.byu.edu/FiberOpticConnectors.parts/images/smf28.pdf>

### Corning® SMF-28™ Optical Fiber Product Information



PI1036  
Issued: April 2002  
Supersedes: December 2001  
ISO 9001 Registered

### Corning® Single-Mode Optical Fiber

#### The Standard For Performance

Corning® SMF-28™ single-mode optical fiber has set the standard for value and performance for telephony, cable television, submarine, and utility network applications. Widely used in the transmission of voice, data, and/or video services, SMF-28 fiber is manufactured to the most demanding specifications in the industry. SMF-28 fiber meets or exceeds ITU-T Recommendation G.652, TIA/EIA-492CAAA, IEC Publication 60793-2 and GR-20-CORE requirements.

Taking advantage of today's high-capacity, low-cost transmission components developed for the 1310 nm window, SMF-28 fiber features low dispersion and is optimized for use in the 1310 nm wavelength region. SMF-28 fiber also can be used effectively with TDM and WDM systems operating in the 1550 nm wavelength region.

#### Environmental Specifications

Environmental Test Condition	Induced Attenuation 1310 nm/1550 nm (dB/km)
-40°C to +85°C*	<0.05
Humidity Cycling -10°C to +85°C*, up to 98% RH	<0.05
Water Immersion, 23±2°C*	<0.05
Heat Aging, 85±2°C*	<0.05

\*Reference temperature = +23°C

#### Operating Temperature Range

-60°C to +85°C

#### Dimensional Specifications

Length (km/reel): fiber lengths available up to 50.4\*

\* Longer spliced lengths available as a premium.

#### Glass Geometry

Fiber Curvature: ≥ 4.0 m radius of curvature

Cladding Diameter: 125.0 ± 0.7 µm

Core-Clad Concentricity: ≤ 0.5 µm

Cladding Non-Circularity: ≤ 1.0%

Defined as  $\left[ \frac{\text{Min. Cladding Diameter}}{\text{Max. Cladding Diameter}} \right] \times 100$

#### Coating Geometry

Coating Diameter: 245 ± 5 µm

Coating-Cladding Concentricity: <12 µm

#### Features And Benefits

- Versatility in 1310 nm and 1550 nm applications
- Enhanced optical properties that optimize transmission performance
- Outstanding geometrical properties for low splice loss and high splice yield
- OVD manufacturing reliability and product consistency
- Optimized for use in loose tube, ribbon, and other common cable design

#### The Sales Leader

Corning SMF-28 fiber is the world's best selling fiber. In 2001, SMF-28 fiber was deployed in over 45 countries around the world. All types of network providers count on this fiber to support network expansion into the 21st Century.

#### Mechanical Specifications

##### Proof Test

The entire fiber length is subjected to a tensile proof stress ≥ 100 kpsi (0.7 GPa/m)\*.

\* Higher proof levels available as a premium.

##### Performance Characterizations

*Characterized parameters are typical values.*

**Core Diameter:** 8.2 µm

**Numerical Aperture:** 0.14

NA is measured at the one percent power level of a one-dimensional far-field scan at 1310 nm.

**Zero Dispersion Wavelength ( $\lambda_0$ ):** 1313 nm

**Zero Dispersion Slope ( $S_0$ ):** 0.086 ps / (nm·km)

**Refractive Index Difference:** 0.36%

**Effective Group Index of Refraction,** ( $N_{\text{eff}}$  @ nominal MFD):

1.4677 at 1310 nm

1.4682 at 1550 nm

**Fatigue Resistance Parameter ( $n_d$ ):** 20

**Coating Strip Force:**

Dry: 0.6 lbs. (3N)

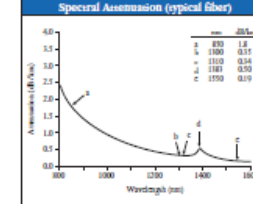
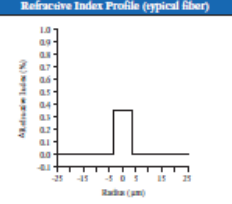
Wet, 14-day room temperature: 0.6 lbs. (3N)

**Rayleigh Backscatter Coefficient** (for 1 m pulse width):

1310 nm: -77 dB

1550 nm: -82 dB

#### Refractive Index Profile (typical fiber)



#### Protection And Versatility

SMF-28 fiber is protected for long-term performance and reliability by the CPC® coating system. Corning's enhanced, dual acrylate CPC coatings provide excellent fiber protection and are easy to work with. CPC coatings are designed to be mechanically stripped and have an outside diameter of 245 µm. They are optimized for use in many single- and multi-fiber cable designs including loose tube, ribbon, slotted core, and tight buffer cables.

#### Patented Quality Process

SMF-28 fiber is manufactured using the Outside Vapor Deposition (OVD) process, which produces a truly synthetic ultra-pure fiber. As a result, Corning SMF-28 fiber has consistent geometric properties, high strength, and low attenuation. Corning SMF-28 fiber can be counted on to deliver excellent performance and high reliability, reel after reel. Measurement methods comply with ITU recommendations G.650, IEC 60793-1, and Bellcore GR-20-CORE.

#### Optical Specifications

##### Attenuation

Wavelength (nm)	Premium	Standard
1310	≤ 0.34	≤ 0.35
1550	≤ 0.20	≤ 0.22

\*Average attenuation values available upon request

##### Point Discontinuity

No point discontinuity greater than 0.10 dB at either 1310 nm or 1550 nm.

##### Attenuation at the Water Peak

The attenuation at 1383 ± 3 nm shall not exceed 2.1 dB/km.

##### Attenuation vs. Wavelength

Range (nm)	Ref. λ (nm)	Max. Δ Difference (dB/km)
1285 - 1330	1310	0.05
1525 - 1575	1550	0.05

The attenuation in a given wavelength range does not exceed the attenuation of the reference wavelength ( $\lambda_0$ ) by more than the value  $\Delta$ .

#### Ordering Information

To order Corning® SMF-28™ fiber, contact your sales representative, or call the Optical Fiber Customer Service Department at 607-248-2000 or 444-1244-287-437 in Europe. Please specify the following parameters when ordering.

**Fiber Type:** Corning® SMF-28™ Fiber

**Fiber Attenuation:** dB/km

**Fiber Quantity:** km

**Others:** (Requested ship date, etc.)

#### Attenuation with Bending

Mandrel Diameter (mm)	Number of Turns	Wavelength (nm)	Induced Attenuation* (dB)
32	1	1350	≤ 0.50
50	100	1310	≤ 0.05
50	100	1550	≤ 0.10
60	100	1350	≤ 0.05

\*The induced attenuation due to fiber wrapped around a mandrel of a specified diameter.

#### Cable Cut-off Wavelength ( $\lambda_{\text{cut}}$ )

$\lambda_{\text{cut}} \leq 1260$  nm

#### Mode-Field Diameter

9.2 ± 0.4 µm at 1310 nm

10.4 ± 0.8 µm at 1550 nm

#### Dispersion

Zero Dispersion Wavelength ( $\lambda_0$ ):

1302 nm ≤  $\lambda_0$  ≤ 1322 nm

Zero Dispersion Slope ( $S_0$ ):

≤ 0.092 ps/(nm²·km)

$$\text{Dispersion} = D(\lambda) = \frac{S_0}{4} \left[ \lambda - \frac{\lambda_0^4}{\lambda^3} \right] \text{ ps/(nm·km)}, \quad \text{for } 1200 \text{ nm} \leq \lambda \leq 1600 \text{ nm}$$

$\lambda$  = Operating Wavelength

#### Polarization Mode Dispersion

##### Fiber Polarization Mode Dispersion (PMD)

Value (ps/ $\sqrt{\text{km}}$ )

PMD Link Value: ≤ 0.1\*

Maximum Individual Fiber: ≤ 0.2

\*Complies with IEC 60794-3-3001, section 5.5, Method 1, September 2001.

The PMD link value is a term used to describe the PMD of concatenated lengths of fiber (also known as the link quadrature average). This value is used to determine a statistical upper limit for system PMD performance.

Individual PMD values may change when cabled. Corning's fiber specification supports network design requirements for a 0.5 ps/km maximum PMD.

#### Coming Incorporated

[www.corning.com/opticalfiber](http://www.corning.com/opticalfiber)

One Riverfront Plaza

Corning, NY 14831

Phone: 800-525-2524 (U.S. and Canada)

607-786-8125 (International)

Fax: 800-539-3632 (U.S. and Canada)

607-786-8344 (International)

Email: [cocfc@corning.com](mailto:cocfc@corning.com)

#### Europe

Phone: 00 800 6620 6623 (U.K., Ireland, Italy, France, Germany, The Netherlands, Spain and Sweden)

+1 607 786 8125 (All other countries)

Fax: +1 607 786 8344

#### Australia

Phone: 3 800 148-690

Fax: 1 800 148-568

#### Indonesia

Phone: 001-803-015-721-3261

Fax: 001-803-015-721-2162

#### Malaysia

Phone: 1-800-80-3356

Fax: 1-800-80-3355

#### Philippines

Phone: 1-800-5-116-0338

Fax: 1-800-5-116-0339

#### Singapore

Phone: 65-505-1300-955

Fax: 65-505-1300-956

#### Thailand

Phone: 001-800-1-5-721-1263

Fax: 001-800-1-5-721-1264

#### Latin America

Brazil

Phone: 000817-762-4732

Fax: 000817-762-4996

#### Mexico

Phone: 001-800-339-1719

Fax: 001-800-339-1472

#### Venezuela

Phone: 800-3-4418

Fax: 800-3-4419

#### Greater China

##### Beijing

Phone: [86] 10-6505-5066

Fax: [86] 10-6505-5077

##### Hong Kong

Phone: [852] 2807-2723

Fax: [852] 2807-2152

##### Shanghai

Phone: [86] 21-3222-4668

Fax: [86] 21-6288-4575

##### Taiwan

Phone: [886] 2-2716-0338

Fax: [886] 2-2716-0339

E-mail: [GCCofc@corning.com](mailto:GCCofc@corning.com)

Corning is a registered trademark. SMF-28 and CPC are trademarks of Corning Incorporated.

Any warranty or liability relating to any Corning optical fiber is only contained in the written agreement between Corning Incorporated and the direct purchaser of such fiber.

©2002, Corning Incorporated

## Appendix C

[http://cvimellesgriot.com/products/Documents/Catalog/Dispersion\\_Equations.pdf](http://cvimellesgriot.com/products/Documents/Catalog/Dispersion_Equations.pdf)

Appendix & Indices
Ask About Our Build-to-Print and Custom Capabilities
DEM

## Dispersion Equations

Appendix

General Index

Product Code/Product Number Index

**Dispersion Equations for Optical Materials**

Typically either a Sellmeier or Laurent series equation is used to describe glass dispersion.

The Sellmeier series equation is:

$$\eta^2 = 1 + \frac{B_1\lambda^2}{\lambda^2 - C_1} + \frac{B_2\lambda^2}{\lambda^2 - C_2} + \frac{B_3\lambda^2}{\lambda^2 - C_3}$$

where the wavelength,  $\lambda$ , is expressed in  $\mu\text{m}$ .

**Dispersion Equation Constants - Sellmeier series equation**

	B <sub>1</sub>	B <sub>2</sub>	B <sub>3</sub>	C <sub>1</sub>	C <sub>2</sub>	C <sub>3</sub>
MgF <sub>2</sub> $\eta_0$	4.13440230E-01	5.04974990E-01	2.49048620E+00	1.35737865E-03	8.23767167E-03	5.65107755E+02
MgF <sub>2</sub> $\eta_0$	4.87551080E-01	3.98750310E-01	2.31203530E+00	1.88217800E-03	8.95188847E-03	5.66135591E+02
Sapphire $\eta_0$	1.50397590E+00	5.50691410E-01	6.59273790E+00	5.48041129E-03	1.47994281E-02	4.02895140E+02
Sapphire $\eta_0$	1.48134980E+00	6.50547130E-01	5.34140210E+000	5.27992610E-03	1.42382647E-02	3.25017834E+02
CaF <sub>2</sub>	5.67588800E-01	4.71091400E-01	3.84847230E+00	2.52642999E-03	1.00783328E-02	1.20055597E+03
Fused Silica	6.96166300E-01	4.07942600E-01	8.97479400E-01	4.67914826E-03	1.35120631E-02	9.79340025E+01
Schott BK7	1.03961212E+00	2.31792344E-01	1.01046945E+00	6.00069867E-03	2.00179144E-02	1.03560653E+02
Schott N-BK7	1.03961212E+00	2.31792344E-01	1.01046945E+00	6.00069867E-03	2.00179144E-02	1.03560653E+02
Schott F2	1.34533359E+00	2.09073118E-01	9.37357162E-01	9.97743871E-03	4.70450767E-02	1.11886764E+02
Schott N-F2	1.39757037E+00	1.59201403E-01	1.26865430E+00	9.95906143E-03	5.46931752E-02	1.19248346E+02
Schott SF2	1.40301821E+00	2.09073176E-01	9.39056586E-01	1.05795466E-02	4.93226978E-02	1.12405955E+02
Schott SF10	1.61625977E+00	2.59229334E-01	1.07762317E+00	1.27534559E-02	5.81983954E-02	1.16607680E+02
Schott N-SF10	1.62153902E+00	2.56287842E-01	1.64447552E+00	1.22241457E-02	5.95736775E-02	1.47468793E+02
Schott SF11	1.73848403E+00	3.11168974E-01	1.17490871E+00	1.36068604E-02	6.15960463E-02	1.21922711E+02
Schott N-SF11	1.73759695E+00	3.13747346E-01	1.89878101E+00	1.13188707E-02	6.23068142E-02	1.55236290E+02
Schott N-LAI21	1.22718116E+00	4.20783743E-01	1.01284843E+00	6.02075682E-03	1.96862889E-02	8.84370099E+01

**Laurent Series Equation**

The Laurent series equation is:

$$\eta^2 = A_0 + A_1\lambda^2 + \frac{A_2}{\lambda^2} + \frac{A_3}{\lambda^4} + \frac{A_4}{\lambda^6} + \frac{A_5}{\lambda^8}$$

where the wavelength,  $\lambda$ , is expressed in  $\mu\text{m}$ .

**Dispersion Equation Constants - Laurent series equation**

	A <sub>0</sub>	A <sub>1</sub>	A <sub>2</sub>	A <sub>3</sub>	A <sub>4</sub>	A <sub>5</sub>
Crystal Quartz $\eta_0$	2.38490000E+00	-1.25900000E-02	1.07900000E-02	1.65180000E-04	-1.94741000E-06	9.36476000E-08
Crystal Quartz $\eta_0$	2.35728000E+00	-1.17000000E-02	1.05400000E-02	1.34148000E-04	-4.45368000E-07	5.92362000E-08
S-LAM60M	2.95844800E+00	-1.54203600E-02	2.03097300E-02	1.30264600E-03	-1.23870800E-04	7.40159800E-06
S-BSL7M	2.26250500E+00	-1.03792100E-02	9.34172400E-03	6.45307100E-04	-7.46385800E-05	4.09621500E-06

For up-to-date information on materials compliance with European Union RoHS, see [www.cvimellesgriot.com](http://www.cvimellesgriot.com)

6 Appendix


  
www.cvimellesgriot.com

- 103 -

## Appendix D

### Computer 1

CPU	Intel® Core™ i5 M460 @ 2.53GHz
RAM	4.00 GB (3.86 GB Available)
OS	Windows 7 Home Premium (64-bit) with Service Pack 1
MATLAB 7.10.0 (R2010a) <Student Version>	
EDU>> memory	
Maximum possible array: 2046 MB (2.146e+009 bytes) *	
Memory available for all arrays: 3494 MB (3.664e+009 bytes) **	
Memory used by MATLAB: 267 MB (2.805e+008 bytes)	
Physical Memory (RAM): 3958 MB (4.150e+009 bytes)	
* Limited by contiguous virtual address space available.	
** Limited by virtual address space available.	

### Computer 2

CPU	Intel® Core™ i7 950 @ 3.07GHz
RAM	24.0 GB
OS	Windows 7 Professional (64-bit)
MATLAB 7.12.0.0635 (R2011a)	
EDU>> memory	
Maximum possible array: 59142 MB (6.201e+010 bytes) *	
Memory available for all arrays: 59142 MB (6.201e+010 bytes) *	
Memory used by MATLAB: 436 MB (4.570e+008 bytes)	
Physical Memory (RAM): 24574 MB (2.577e+010 bytes)	
* Limited by System Memory (physical + swap file) available.	

For **Computer 1**, when **48** eigenvalues are set to be sought, the maximum number of grid points allowed for vector-field simulation is approximately **350-by-350**, limited mainly by the contiguous virtual address space available (**32-bit** allocation). For **Computer 2**, under the same setting, the maximum number is approximately **1200-by-1200**, limited by system memory.

## Appendix E

May 29

ZB7+

$$\text{Field dependence} = \exp[i(\beta z - \omega t)] \Rightarrow \frac{\partial}{\partial t} \rightarrow -i\omega, \frac{\partial}{\partial z} \rightarrow i\beta.$$

Li-Wei

$$\begin{cases} ik_0 H_x = U_y E_z - i\beta E_y & ① \\ ik_0 H_y = i\beta E_x - U_x E_z & ② \\ ik_0 H_z = U_x E_y - U_y E_x & ③ \end{cases}$$

\*  $\epsilon_{xx}, \epsilon_{yy} \dots$  表  $\epsilon_r \dots, \epsilon = \epsilon_e \cdot \epsilon_r$

\*  $E$  表  $E'$ ,  $E' = \frac{E}{\epsilon_0}$ .

$$\begin{cases} -ik_0 \epsilon_{xx} E_x - ik_0 \epsilon_{xy} E_y = V_y H_z - i\beta H_y & ④ \\ -ik_0 \epsilon_{yx} E_x - ik_0 \epsilon_{yy} E_y = i\beta H_x - V_x H_z & ⑤ \\ -ik_0 \epsilon_{zz} E_z = V_x H_y - V_y H_x & ⑥ \end{cases}$$

$$\text{關係式: } \exists_{zz} = \frac{1}{\epsilon_{zz}}$$

$$\beta E_x = k_0 H_y - iU_x E_z = k_0 H_y + \frac{1}{k_0} U_x \exists_{zz} V_x H_y - \frac{1}{k_0} U_x \exists_{zz} V_y H_x.$$

$$\beta E_y = -k_0 H_x - iU_y E_z = -k_0 H_x + \frac{1}{k_0} U_y \exists_{zz} V_x H_y - \frac{1}{k_0} U_y \exists_{zz} V_y H_x$$

$$-iE_z = \frac{1}{k_0} \exists_{zz} V_x H_y - \frac{1}{k_0} \exists_{zz} V_y H_x$$

$$iH_z = \frac{1}{k_0} U_x E_y - \frac{1}{k_0} U_y E_x$$

$$i\beta H_z = \frac{1}{k_0} U_x \beta E_y - \frac{1}{k_0} U_y \beta E_x$$

$$-i\beta E_z = \frac{1}{k_0} \exists_{zz} V_x \beta H_y - \frac{1}{k_0} \exists_{zz} V_y \beta H_x$$

$$\beta H_y = k_0 \epsilon_{xx} E_x + k_0 \epsilon_{yy} E_y - iV_y H_z = k_0 \epsilon_{xx} \bar{E}_x + k_0 \epsilon_{yy} \bar{E}_y - \frac{1}{k_0} V_y U_x \bar{E}_y + \frac{1}{k_0} V_y U_y \bar{E}_x$$

$$\beta H_x = -k_0 \epsilon_{yx} \bar{E}_x - k_0 \epsilon_{yy} \bar{E}_y - iV_x H_z = -k_0 \epsilon_{yx} \bar{E}_x - k_0 \epsilon_{yy} \bar{E}_y - \frac{1}{k_0} V_x U_x \bar{E}_y + \frac{1}{k_0} V_x U_y \bar{E}_x$$

P.1

$$\underline{H_x} : i\beta H_x = -ik_0 \epsilon_{yx} E_x - ik_0 \epsilon_{yy} E_y + V_x H_z. \quad [EB7+]$$

$$\begin{aligned} \beta^2 H_x &= -k_0 \epsilon_{yx} \beta E_x - k_0 \epsilon_{yy} \beta E_y - i\beta V_x H_z \\ &= -k_0 \epsilon_{yx} \beta E_x - k_0 \epsilon_{yy} \beta E_y - V_x \left[ \frac{1}{k_0} U_x \beta \bar{E}_y - \frac{1}{k_0} U_y \beta \bar{E}_x \right] \end{aligned}$$

$$= (-k_0 \epsilon_{yx} + \frac{1}{k_0} V_x U_y) \beta \bar{E}_x + (-k_0 \epsilon_{yy} - \frac{1}{k_0} V_x U_x) \beta \bar{E}_y$$

$$= (-k_0 \epsilon_{yx} + \frac{1}{k_0} V_x U_y) (k_0 \underline{H_y} + \frac{1}{k_0} U_x \partial_{zz} V_x \underline{H_y} - \frac{1}{k_0} U_x \partial_{zz} V_y \underline{H_x}) +$$

$$(-k_0 \epsilon_{yy} - \frac{1}{k_0} V_x U_x) (-k_0 \underline{H_x} + \frac{1}{k_0} U_y \partial_{zz} V_x \underline{H_y} - \frac{1}{k_0} U_y \partial_{zz} V_y \underline{H_x})$$

$$\begin{aligned} Q_{xx} : \\ (H_x) &= \boxed{\epsilon_{yx} U_x \partial_{zz} V_y H_x} - \frac{1}{k_0^2} V_x U_y U_x \partial_{zz} V_y H_x + \\ &\quad k_0^2 \epsilon_{yy} H_x^\circ + \epsilon_{yy} U_y \partial_{zz} V_y H_x + V_x U_x H_x^\Delta + \frac{1}{k_0^2} V_x U_x U_y \partial_{zz} V_y H_x^\square \end{aligned}$$

$$\begin{aligned} Q_{xy} : \\ (H_y) &= \boxed{-k_0^2 \epsilon_{yx} H_y - \epsilon_{yx} U_x \partial_{zz} V_x H_y} + V_x U_y H_y^\nabla + \frac{1}{k_0^2} V_x U_y U_x \partial_{zz} V_x H_y^\circ \\ &\quad - \epsilon_{yy} U_y \partial_{zz} V_x H_y^\nabla - \frac{1}{k_0^2} V_x U_x U_y \partial_{zz} V_x H_y^\Delta. \end{aligned}$$

P.2

$$H_y = i\beta H_y = i\kappa_0 \epsilon_{xx} E_x + i\kappa_0 \epsilon_{xy} E_y + V_y H_z.$$

$$\beta^2 H_y = \kappa_0 \epsilon_{xx} \beta E_x + \kappa_0 \epsilon_{xy} \beta E_y - V_y \left[ \frac{1}{\kappa_0} U_x \beta E_y - \frac{1}{\kappa_0} U_y \beta E_x \right]$$

$$= (\kappa_0 \epsilon_{xx} + \frac{1}{\kappa_0} V_y U_y) \beta E_x + (\kappa_0 \epsilon_{xy} - \frac{1}{\kappa_0} V_y U_x) \beta E_y$$

$$= (\kappa_0 \epsilon_{xx} + \frac{1}{\kappa_0} V_y U_y) (\kappa_0 H_y + \frac{1}{\kappa_0} U_x \partial_{zz} V_x H_y - \frac{1}{\kappa_0} U_x \partial_{zz} V_y H_x) +$$

$$(\kappa_0 \epsilon_{xy} - \frac{1}{\kappa_0} V_y U_x) (-\kappa_0 H_x + \frac{1}{\kappa_0} U_y \partial_{zz} V_x H_y - \frac{1}{\kappa_0} U_y \partial_{zz} V_y H_x)$$

$$Q_{yx} = -\epsilon_{xx} U_x \partial_{zz} V_y H_x - \frac{1}{\kappa_0^2} V_y U_y U_x \partial_{zz} V_y H_x$$

$$\boxed{-\kappa_0^2 \epsilon_{xy} H_x - \epsilon_{xy} U_y \partial_{zz} V_y H_x + V_y U_x H_x + \frac{1}{\kappa_0^2} V_y U_x U_y \partial_{zz} V_y H_x}$$

$$Q_{xy} : \kappa_0^2 \epsilon_{xx} H_y + \epsilon_{xx} U_x \partial_{zz} V_x H_y + V_y U_y H_y +$$

$$\frac{1}{\kappa_0^2} V_y U_y U_x \partial_{zz} V_x H_y + \boxed{\epsilon_{xy} U_y \partial_{zz} V_x H_y - \frac{1}{\kappa_0^2} V_y U_x U_y \partial_{zz} V_x H_y}$$

$$E_x : i\beta E_x = ik_0 H_y + U_x E_z$$

ZB7+

$$\begin{aligned} \beta^2 E_x &= k_0 \beta H_y - i\beta U_x E_z = k_0 \beta H_y + U_x \left( \frac{1}{k_0} \partial_{zz} V_x \beta H_y - \frac{1}{k_0} \partial_{zz} V_y \beta H_x \right) \\ &= (k_0 + \frac{1}{k_0} U_x \partial_{zz} V_x) \beta H_y - \frac{1}{k_0} U_x \partial_{zz} V_y \beta H_x \\ &= (k_0 + \frac{1}{k_0} U_x \partial_{zz} V_x) (k_0 \epsilon_{xx} \overset{\circ}{E_x} + k_0 \epsilon_{yy} \overset{\circ}{E_y} - \frac{1}{k_0} V_y U_x \overset{\circ}{E_y} + \frac{1}{k_0} V_y U_y \overset{\circ}{E_x}) \\ &\quad - \frac{1}{k_0} U_x \partial_{zz} V_y (-k_0 \epsilon_{yx} \overset{\circ}{E_x} - k_0 \epsilon_{yy} \overset{\circ}{E_y} - \frac{1}{k_0} U_x U_x \overset{\circ}{E_y} + \frac{1}{k_0} U_x U_y \overset{\circ}{E_x}) \end{aligned}$$

$$\begin{aligned} P_{xx}^{(E_x)} &: k_0^2 \epsilon_{xx} \overset{\circ}{E_x} + V_y U_y \overset{\circ}{E_x} + U_x \partial_{zz} V_x \epsilon_{xx} \overset{\circ}{E_x} + \frac{1}{k_0^2} U_x \partial_{zz} V_x V_y U_y \overset{\circ}{E_x} \\ &\quad + U_x \partial_{zz} V_y \epsilon_{yx} \overset{\circ}{E_x} - \frac{1}{k_0^2} U_x \partial_{zz} V_y V_x U_y \overset{\circ}{E_x}. \end{aligned}$$

$$\begin{aligned} P_{yy}^{(E_y)} &: \boxed{k_0^2 \epsilon_{yy} \overset{\circ}{E_y}} - V_y U_x \overset{\circ}{E_y} + \boxed{U_x \partial_{zz} V_x \epsilon_{yy} \overset{\circ}{E_y}} - \frac{1}{k_0^2} U_x \partial_{zz} V_x V_y U_x \overset{\circ}{E_y} \\ &\quad + U_x \partial_{zz} V_y \epsilon_{yy} \overset{\circ}{E_y} + \frac{1}{k_0^2} U_x \partial_{zz} V_y V_x U_x \overset{\circ}{E_y} \end{aligned}$$

✓ 8.4

$$E_y : i\beta E_y = -ik_0 H_x + U_y E_z$$

$$\beta^2 E_y = -k_0 \beta H_x - i\beta U_y E_z$$

$$= -k_0 \beta H_x + U_y \left[ \frac{1}{k_0} \partial_{zz} V_x \beta H_y - \frac{1}{k_0} \partial_{zz} V_y \beta H_x \right]$$

$$= (-k_0 - \frac{1}{k_0} U_y \partial_{zz} V_y) \beta H_x + \frac{1}{k_0} U_y \partial_{zz} V_x \beta H_y$$

$$= (-k_0 - \frac{1}{k_0} U_y \partial_{zz} V_y) (-k_0 \epsilon_{yx} \overline{E_x} - k_0 \epsilon_{yy} \overline{E_y} - \frac{1}{k_0} V_x U_x \overline{E_y} + \frac{1}{k_0} V_x U_y \overline{E_x})$$

$$+ \frac{1}{k_0} U_y \partial_{zz} V_x (k_0 \epsilon_{xx} \overline{E_x} + k_0 \epsilon_{xy} \overline{E_y} - \frac{1}{k_0} V_y U_x \overline{E_y} + \frac{1}{k_0} V_y U_y \overline{E_x})$$

$$P_{yx} : \begin{aligned} & \boxed{-k_0^2 \epsilon_{yx} \overline{E_x}} - V_x U_y \overline{E_x} + U_y \partial_{zz} V_y \epsilon_{yx} \overline{E_x} - \frac{1}{k_0^2} U_y \partial_{zz} V_y V_x U_y \overline{E_x} \\ & + U_y \partial_{zz} V_x \epsilon_{xx} \overline{E_x} + \frac{1}{k_0^2} U_y \partial_{zz} V_x V_y U_y \overline{E_x}. \end{aligned}$$

$$P_{yy} : \begin{aligned} & k_0^2 \epsilon_{yy} \overline{E_y} + V_x U_x \overline{E_y} + U_y \partial_{zz} V_y \epsilon_{yy} \overline{E_y} + \frac{1}{k_0^2} U_y \partial_{zz} V_y V_x U_x \overline{E_y} \\ & + U_y \partial_{zz} V_x \epsilon_{xy} \overline{E_y} - \frac{1}{k_0^2} U_y \partial_{zz} V_x V_y U_x \overline{E_y}. \end{aligned}$$

P.5

## Bibliography

### Agrawal, 2007

Govind P. Agrawal, Nonlinear Fiber Optics, Fourth Edition, Academic Press (2007)

### Berenger, 1994

Jean-Pierre Berenger, A perfectly matched layer for the absorption of electromagnetic waves, *Journal of Computational Physics*, Vol. 114, Issue 2, pp. 185-200 (1994)

### Bierwirth *et al.*, 1986

Karlheinz Bierwirth, Norbert Schulz, and Fritz Arndt, Finite-Difference Analysis of Rectangular Dielectric Waveguide Structures, *IEEE Transactions on Microwave Theory and Techniques*, Vol. MTT-34, No. 11, pp. 1104-1114 (1986)

### Birks *et al.*, 1997

T. A. Birks, J. C. Knight, and P. St. J. Russell, Endlessly single-mode photonic crystal fiber, *Optics Letters*, Vol. 22, Issue 13, pp. 961-963 (1997)

### Chen *et al.*, 2009

Ming-yun Chen, Sen-ming Hsu, and Hung-Chun Chang, A finite-difference frequency-domain method for full-vectorial mode solutions of anisotropic optical waveguides with arbitrary permittivity tensor, *Optics Express*, Vol. 17, Issue 8, pp. 5965-5979 (2009)

### Chiang, 1994

K. S. Chiang, Review of numerical and approximate methods for the modal analysis of general optical dielectric waveguides, *Optical and Quantum Electronics*, Vol. 26, No. 3, S113-S134 (1994)

### Dils, 1983

R. R. Dils, High-temperature optical fiber thermometer, *Journal of Applied Physics*, Vol. 54, No. 3, pp. 1198-1201 (1983)

### Du *et al.*, 2004

Fang Du, Yan-Qing Lu, and Shin-Tson Wu, Electrically tunable liquid-crystal photonic crystal fiber, *Applied Physics Letters*, Vol. 85, No. 2, pp. 2181-2183 (2004)

### Dudley *et al.*, 2006

John M. Dudley, Goëry Genty, and Stéphane Coen, Supercontinuum generation in photonic crystal fiber, *Reviews of Modern Physics*, Volume 78, pp. 1135-1183 (2006)

### Ertman *et al.*, 2009

Slawomir Ertman, Tomasz R. Wolinski, Dariusz Pysz, Ryszard Buczynski, Edward Nowinowski-Kruszelnicki, and Roman Dabrowski, Low-loss propagation and continuously tunable birefringence in high-index photonic crystal fibers filled with nematic liquid crystals, *Optics Express*, Vol. 17, Issue 21, pp. 19298-19310 (2009)

### Fallahkhair *et al.*, 2008

Arman B. Fallahkhair, Kai S. Li, and Thomas E. Murphy, Vector Finite Difference Modesolver for Anisotropic Dielectric Waveguides, *Journal of Lightwave Technology*, Vol. 26, Issue 11, pp. 1423-1431 (2008)

### Gloge, 1971

D. Gloge, Weakly Guiding Fibers, *Applied Optics*, Vol. 10, Issue 10, pp. 2252-2258 (1971)

### Guo *et al.*, 2004

Shangping Guo, Feng Wu, Sacharia Albin, and Robert Rogowski, Photonic band gap analysis using finite-difference frequency-domain method *Optics Express*, Vol. 12, Issue 8, pp. 1741-1746 (2004)

### Huang and Xu, 1993

W. P. Huang and C. L. Xu, Simulation of Three-Dimensional Optical Waveguides by a Full-Vector Beam Propagation Method, *IEEE Journal of Quantum Electronics*, Vol. 29, No. 10, pp. 2639-2649 (1993)

### Ivinskaya *et al.*, 2010

Aliaksandra M. Ivinskaya, Dzmitry M. Shyroki, and Andrei V. Lavrinenko, Three Dimensional Finite-Difference Frequency-Domain Method in Modeling of Photonic Nanocavities, *IEEE ICTON 2010 Mo.P.16* (2010)

### Joannopoulos *et al.*, 2008

Photonic Crystals: Molding the Flow of Light, John D. Joannopoulos, Steven G. Johnson, Joshua N. Winn, and Robert D. Meade, Princeton University Press (2008)

### John, 1987

Sajeev John, Strong Localization of Photons in Certain Disordered Dielectric Superlattices, *Physical Review Letters*, Vol. 58, Issue 23, pp. 2486-2489 (1987)

### Knight, 2003

Jonathan C. Knight, Photonic crystal fibres, *Nature*, Vol. 424, No. 6950, pp. 847-851 (2003)

### Knight *et al.*, 1998

J. C. Knight, J. Broeng, T. A. Birks, P. St. J. Russell, Photonic Band Gap Guidance in Optical Fibers, *Science*, Vol. 282, No. 5393, pp. 1476-1478 (1998)

### Knight *et al.*, 2000

J. C. Knight, J. Arriaga, T. A. Birks, A. Ortigosa-Blanch, W. J. Wadsworth, and P. St. J. Russell, Anomalous Dispersion in Photonic Crystal Fiber, *IEEE Photonics Technology Letters*, Vol. 12, Issue 7, pp. 807-809 (2000)

### Koshiba and Saitoh, 2001

Masanori Koshiba and Kunimasa Saitoh, Numerical Verification of Degeneracy in Hexagonal Photonic Crystal Fibers, *IEEE Photonics Technology Letters*, Vol. 13, No. 12, pp. 1313-1315 (2001)

## Bibliography

---

### Larsen *et al.*, 2003

Thomas Larsen, Anders Bjarklev, David Hermann, and Jes Broeng, Optical devices based on liquid crystal photonic bandgap fibres, *Optics Express*, Vol. 11, Issue 20, pp. 2589-2596 (2003)

### Lee *et al.*, 2010

Chun-Hong Lee, Ching-Hsiang Chen, Chia-Lung Kao, Chin-Ping Yu, Szu-Ming Yeh, Wood-Hi Cheng, and Tsung-Hsien Lin, Photo and electrical tunable effects in photonic liquid crystal fiber, *Optics Express*, Vol. 18, Issue 3, pp. 2814-2821 (2010)

### Lusse *et al.*, 1994

P. Lusse, P. Stuwe, J. Schule, and H.-G. Unger, Analysis of vectorial mode fields in optical waveguides by a new finite difference method, *Journal of Lightwave Technology*, Vol. 12, Issue 3, pp. 487-494 (1994)

### Medhat *et al.*, 2002

M. Medhat, S. Y. El-Zaiat, Amr Radi and M. F. Omar, Application of fringes of equal chromatic order for investigating the effect of temperature on optical parameters of a GRIN optical fibre, *Journal of Optics A: Pure and Applied Optics*, Vol. 4, pp. 174-179 (2002)

### Mogilevtsev *et al.*, 1999

D. Mogilevtsev, T. A. Birks, and P. St. J. Russell, Localized Function Method for Modeling Defect Modes in 2-D Photonic Crystals, *Journal of Lightwave Technology*, Vol. 17, No. 11, pp. 2078-2081 (1999)

### Reeves *et al.*, 2002

W. H. Reeves, J. C. Knight, P. St. J. Russell, and P. J. Roberts, Demonstration of ultra-flattened dispersion in photonic crystal fibers, *Optics Express*, Vol. 10, Issue 14, pp. 609-613 (2002)

### Riishede *et al.*, 2003

Jesper Riishede, Niels Asger Mortensen, and Jesper Lægsgaard, A 'poor man's approach' to modelling micro-structured optical fibres, *Journal of Optics A: Pure and Applied Optics*, Vol. 5, No. 5, pp. 534-538 (2003)

### Russell, 2003

Philip Russell, Photonic Crystal Fibers, *Science*, Vol. 299, pp. 358-362 (2003)

### Saitoh and Koshiba, 2005

Kunimasa Saitoh and Masanori Koshiba, Numerical modeling of photonic crystal fibers, *Journal of Lightwave Technology*, Vol. 23, No. 11, pp. 3580-3590 (2005)

### Scarmozzino *et al.*, 2000

R. Scarmozzino, A. Gopinath, R. Pregla and S. Helfert, Numerical techniques for modeling guided-wave photonic devices, *IEEE Journal of Selected Topics in Quantum Electronics*, Vol. 6, Issue 1, pp. 50-162 (2000)

### Schirmer *et al.*, 1997

Jorg Schirmer, Peter Kohns, Theodor Schmidt-Kaler, Anatoli A. Muravski, Sergei Ye. Yakovenko, Vladimir S. Bezborodov, Roman Dabrowski, and Povilas Adomenas, Birefringence and Refractive Indices Dispersion of Different Liquid Crystalline Structures, *Molecular Crystals and Liquid Crystals*, Vol. 307, Issue 1, pp. 17-42 (1997)

### Shen *et al.*, 1999

Yonghang Shen, Limin Tong, Yanqi Wang, and Linhua Ye, Sapphire-Fiber Thermometer Ranging from 20 to 1800 °C, *Applied Optics*, Vol. 38, Issue 7, pp. 1139-1143 (1999)

### Snyder and Love, 1983

Allan W. Snyder and John D. Love, *Optical Waveguide Theory*, Springer (1983)

### Steel *et al.*, 2001

M. J. Steel, T. P. White, C. M. Sterke, R. C. McPhedran, and L. C. Botten, Symmetry and degeneracy in microstructured optical fibers, *Optics Letters*, Vol. 26, No. 8, pp. 488-490 (2001)

### Stern, 1988

M. S. Stern, Semivectorial polarised finite difference method for optical waveguides with arbitrary index profiles, *IEE Proceedings*, Vol. 135, Pt. J, No. 1, pp. 56-63 (1988)

### Sun and Chan, 2007

J. Sun and C. C. Chan, Hybrid guiding in liquid-crystal photonic crystal fibers, *Journal of the Optical Society of America B*, Vol. 24, Issue 10, pp. 2640-2646 (2007)

### Thyagarajan and Ghatak, 2007

K. Thyagarajan and Ajoy Ghatak, *Fiber Optic Essentials*, John Wiley & Sons (2007)

### Wolinski *et al.*, 2006

T. R. Wolinski, K. Szaniawska, S. Ertman, P. Lesiak, A. W. Domanski, R. Dabrowski, E. Nowinowski-Kruszelnicki, and J Wojcik, Influence of temperature and electrical fields on propagation properties of photonic liquid-crystal fibres, *Measurement Science and Technology*, Vol. 17, No. 5 (2006)

### Yablonovitch, 1993

E. Yablonovitch, Photonic band-gap structures, *Journal of the Optical Society of America B*, Vol. 10, No. 2, pp. 283-295 (1993)

### Yee, 1966

Kane S. Yee, Numerical Solution of Initial Boundary Value Problems Involving Maxwell's Equations in Isotropic Media, *IEEE Transactions on Antennas and Propagation*, Vol. Ap-13, No. 3, pp. 302-307 (1966)

### Yu and Chang, 2004

Chin-Ping Yu and Hung-Chun Chang, Yee-mesh-based finite difference eigenmode solver with PML absorbing boundary conditions for optical waveguides and photonic crystal fibers, *Optics Express*, Vol. 12, Issue 25, pp. 6165-6177 (2004)

## Bibliography

---

### Zhu and Brown, 2002

Zhaoming Zhu and Thomas G. Brown, Full-vectorial finite-difference analysis of microstructured optical fibers, Optics Express, Vol. 10, No. 17, pp. 853-864 (2002)

### Zografopoulos and Kriegis, 2009

Dimitrios C. Zografopoulos and Emmanouil E. Kriegis, Tunable Polarization Properties of Hybrid-Guiding Liquid-Crystal Photonic Crystal Fibers, Journal of Lightwave Technology, Vol. 27, Issue 6, pp. 773-779 (2009)

### ARPACK

ARPACK, the ARnoldi PACKage,  
[http://www.caam.rice.edu/software/ARPACK/  
eigs](http://www.caam.rice.edu/software/ARPACK/eigs)

MATLAB Documentation

eigs - Largest eigenvalues and eigenvectors of matrix  
<http://www.mathworks.com/help/techdoc/ref/eigs.html>

### MATLAB

MATrix LABoratory  
<http://www.mathworks.com/products/matlab/>

### Nobel Prize in Physics, 2009

Nobelprize.org, The Nobel Prize in Physics 2009 (29 Aug 2011)  
[http://www.nobelprize.org/nobel\\_prizes/physics/laureates/2009/](http://www.nobelprize.org/nobel_prizes/physics laureates/2009/)